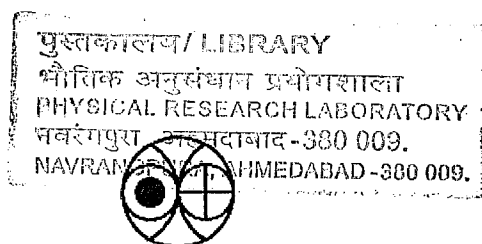


**Investigations on the radiation dose distribution in
natural environment and their implications in
luminescence chronology**

**A THESIS SUBMITTED TO
GUJARAT UNIVERSITY**

**for
the degree of
Doctor of Philosophy in Physics**

**by
P. Morthekai**



Physical Research Laboratory

Ahmedabad 380 009

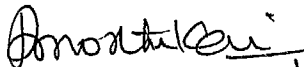
India

July 2007


DECLARATION

This is to certify that the contents of this thesis entitled "Investigations on the radiation dose distribution in natural environment and their implications in luminescence chronology" comprise original research work of the candidate and have at no time been submitted for any other degree or diploma.

Author


Morthekai, P 03/04/07

Guide


Prof. Shyam Lal
Physical Research Laboratory
Ahmedabad- 380 009, Gujarat, India

Dedicated to
my parents and
my PRL luminescence group members

Abstract

Luminescence dating provides the age of the depositional event of sediments through an analysis of the luminescence of minerals (such as feldspars and quartz) constituting the sediment. This application is based on the premise, that Sun exposure prior to sediment deposition photo-bleaches the geological luminescence of minerals to zero or a near zero residual value. On deposition, the day light exposure ceases and a re-accumulation of luminescence in the mineral is initiated due to irradiation from natural radioactivity. The computation of age involve, the ratio of the dose absorbed by the natural minerals like quartz, feldspars, etc. (termed as the palaeodose P) and the annual dose rate, arising due to the decay of natural radioactivity viz. U, Th and K, (Aitken, 1985; 1998; Singhvi and Wagner, 1986). The palaeodose is estimated by measuring the luminescence signal from the natural sample (as received) and by converting it into dose units via appropriate measurements of luminescence sensitivity, using standard protocols and a calibrated laboratory irradiations using a beta source. The dose rate is estimated by measuring the concentration of long lived naturally occurring radioactive elements viz., ^{238}U , ^{232}Th , ^{40}K , in the sample and in its surrounding environment. A small proportion (<5%) of dose rate is from cosmic rays and this depends on the location (latitude, longitude and altitude) and the depth of the samples. The radiation flux arises due to the alpha beta and gamma rays that accompany the radioactive decay of natural radionuclides. Given that alphas, betas and gammas have widely differing ranges in the sediment matrix, the dose deposition from the three components arising from same decay chain is spatially heterogeneous.

The present thesis deals with an important aspect of spatially heterogeneous dose distribution that becomes significant at a single grain level (at spatial scale of $\sim 200\text{ }\mu\text{m}$). The thesis provides an analysis of this spatial heterogeneity of distribution of natural dose and develops a protocol to deal with this aspect by providing a more rigorous age equation.

A luminescence age is the time lapsed since the natural mineral was last exposed to daylight, i.e., prior to deposition. This uses the fact that the daylight exposure of minerals serving as radiation dosimeters photo-bleaches their geologically acquired luminescence. The rate of reduction normally depends on the flux and spectrum of the daylight available to the mineral during its transport. As a general rule, the minerals are heterogeneously bleached at the time of deposition and different mineral grains of the same sediment have different amount of residual signal. To an extent, the advent of single grain and small aliquot techniques help in isolating the most bleached grains/discs (i.e., the grains/discs with minimum residual). This is done by plotting a histogram of palaeodoses of individual single grains/small aliquots and by taking the lowest dose population from this ensemble.

The use of single grains, while allows for the isolation of most bleached grains, however entails complex dosimetric aspects, most of which have been ignored so far. The beta dose, on account of the beta particle range being comparable to the grain sizes, becomes complex. The beta particle range in a sediment matrix is ~ 1 mm and the grain size used for single grains is ~ 200 μm . A spatial heterogeneity in beta dose arises, because of the fact that, in sediments, the quartz grains receive decreasing beta dose with distance to the natural beta emitter (Aitken, 1985). Thus, different quartz grains in a sediment matrix receive different beta doses but uniform gamma doses. Beta particles arise in the decay of all the three naturally occurring radionuclides. Of these potassium is provided by feldspar grains which can stoichiometrically contain up to 14% potassium. Thus, only a few grains account for the total potassium concentration and the associated beta dose. This makes the beta dose from potassium becomes heterogeneous. This beta dose heterogeneity problem was identified when we analysed the dose distribution of 3 aeolian (Wahiba sands, Grand Desierto Mexico dunes and Thar desert samples) samples. The relative standard deviation of the equivalent dose distribution came out to be 21 % and 45 % using multigrain and single grain measurements respectively. This large spread is unexpected from the wind transported sediments as they are relatively well bleached and hence there would be no residual dose before deposition. And the investigations lead us to consider the beta dose heterogeneity. The results of the dose measurement and the investigations are given in Chapter 3.

The beta dose heterogeneity problem was tackled analytically by considering the number density and positional fluctuations of the hotspots (K-feldspars) in the sample matrix which comprise of quartz and feldspar grains. The dose deposited from a hotspot to a quartz grain was derived from the first principles. The hotspots are assumed to be distributed uniformly throughout the sample and they are not correlated. By taking the configuration averaging, a dose distribution was derived. That equation was solved using Laplace Transform technique and in the process a numerical Laplace Inversion algorithm was developed. The measured dose distribution could be fitted to Gumbel (slightly modified version) distribution. The study suggested that, 46 % to 18 % relative standard deviation could be caused solely by the fluctuations (number and position) of the hotspots in the sample matrix alone. The mathematical formulation and the principles are given in Chapter 4.

In Chapter 5, the implications of the spatial heterogeneity of beta dose in the sediments are given. The main implication is that the least absorbed dose in the burial dose distribution would be unaltered even if the grains had considerable bleaching heterogeneity i.e. average dose prior to deposition. This implication lead to a modified version of the Age equation and this equation seem to give true burial age even for the heavily affected partial bleached sediments. This inference was checked using published results of Murray and Roberts (1997), and could explain the dose distribution and the age so computed was in conformity with the controlled ages. We then followed the same procedure in 22 of our Aeolian sediments and the results were encouraging. The inference is that the age calculated by whether conventional age equation or modified age equation would be same if the sample well bleached. Hence the beta dose heterogeneity would have effect in the age calculation by showing up a large spread in the dose distribution. And, if the sample is partially bleached then the modified age equation would give correct burial age. The conventional age equation will not give a correct age.

In summary, till the present work, the minimum palaeodose in quartz grains was assumed to correspond to the most bleached grains and the age was calculated assuming that all the quartz grains received homogeneous natural dose. This thesis instead suggests that, in general the least palaeodose grains correspond to both, the most bleached and least dosed grains. This thesis quantifies the effect of spatially heterogeneous distribution of beta

dose and based on this, proposes a paradigm shift in the manner in which the single grain age analyses are carried out.

Finally, we present conclusions and future outlook.

Acknowledgements

I would like to thank my supervisor Prof. A. K. Singhvi whose research acumen and the never ending spirit to pursue the impossible have made this thesis possible. His inspiring words particularly on holidays encouraged me to do more than what I had been doing. I am also thankful to his whole family for the kindness that they extended to me and gave me a feeling of togetherness. I would like to thank Prof. Shyam Lal for the interest he showed in my research work and for allowing me to register my Ph.D. with him. Dr. Y. S. Mayya is gratefully acknowledged not only for his greatly commendable mathematical thinking but also for the collaborative work without which this thesis wouldn't have taken the present shape. Dr. Mayank Jain, Dr. K. P. N. Murthy and Dr. M. D. Sastry are acknowledged for all they have done for this thesis. I am very thankful to the PRL academic committee for critically reviewing my work and providing valuable suggestions. I am very thankful to library staff, experts from computer centre, workshop, purchase section and canteen of PRL for their prompt help.

I dedicate this thesis to my PRL luminescence group members. I would love to name them and convey my whole heartily thankfulness to each and every one. Dr. Navin Juyal, Dr. Manoj, Mr. Padia, Dr Yogesh Nagar, Madhav, Anil, Timmy, Shinde, Rabiul and Naveen are the people who helped me with this thesis. The long group discussion helped me to master single grain OSL technique about which I had no idea before joining PRL. I am very happy that I met Navinji and Mayank in Ph.D duration and they are still a source

of inspiration to strive perfection in all fronts, and I will ever cherish the friendship of Yogesh, the technically perfect, mischievous, talented and nicest guy and Madhav, the brutally honest and ever smiling man.

This degree being the epitome of academics, I find it worth to acknowledge all my teachers particularly Mr. Prabhu Dhayalan (Physics teacher in my higher secondary school) and Dr. S. Gurubaran (Head, EGRL, IIGM, Tirunelveli) for their inspiration, knowledge and personal care. I would also like to acknowledge the men of sciences whose pain staking efforts have motivated and assisted me in pursuing my research.

I would like to thank PRL volleyball team, Kaka Chai Club members and all of my PRL friends for their friendship which gave me a good balance in life. I am very thankful to my batch (2001) for the good start. Here I would like to thank my friends Sankar, Arun, Solomon, Preeti, Satheesh Thampi and Meenakshisundaram for sharing some of their precious time with me. I think, I'll not forget Kaushikda and Bhavesh because of their clear and insightful words. I can't forget the time spent with Hema (little genius) and Manimaran (anja nenjan). Actually I would love to mention all my friend's names but I am sure the pages are not enough to name them and describe how they had been helpful to me. The fellowship I had with the members of Methodist Church and CNI Tamil congregation was helpful during this thesis time.

Risø National Laboratory, Denmark is acknowledged for allowing me to use its resources for this thesis writing.

I never say thanks to my parents and my sister for anything but will feel immensely grateful to them till my last breath. Because of their willfull sacrifice I am in this level of

finishing my highest degree. And my childhood friend Athisayam annan's selfless spiritual support is also acknowledged.

Above all, as my supervisor's hand had been on all matters regarding this thesis my Triune God's mighty hand was on all the activities mentioned above and hopefully will be in the future also as per His Words in Romans 8²⁸.

P. Morthekai

Contents

| | Page |
|--|-------------|
| Abstract | iv |
| Acknowledgement | viii |
| List of Figures | xiv |
| List of Tables | xxi |
| Chapter 1: Luminescence Dating: A perspective | |
| 1.1 Introduction | 1 |
| 1.2 Luminescence dating: Basic principles | 3 |
| 1.3 Event that can be dated using Luminescence | 5 |
| 1.4 The age equation | 7 |
| 1.5 Luminescence characteristics of Quartz | 9 |
| 1.5.1 UV emission of quartz: TL and OSL | 11 |
| 1.6 Objectives | 17 |
| 1.6.1 Bleaching heterogeneity | 20 |
| 1.6.1.1 Analysis of dose distribution | 24 |
| 1.6.1.2 Analysis of OSL signal | 28 |
| 1.6.2 Beta dose heterogeneity | 30 |
| Chapter 2: Experimental details and Methodology | |
| 2.1 Experimental Details | 36 |
| 2.1.1 Stimulation | 36 |
| 2.1.2 Detection unit | 38 |
| 2.1.3 Stimulation of single grains | 39 |
| 2.1.4 Irradiation | 39 |
| 2.2 Methodology | 42 |
| 2.2.1 Measurement of Equivalent Dose | 42 |
| 2.2.1.1 Multiple Aliquot – Additive Dose (MAAD) | 42 |
| 2.2.1.2 Multiple Aliquot – Regenerative Dose | 42 |
| 2.2.1.3 Single Aliquot – Additive Dose | 44 |
| 2.2.1.4 Single Aliquot – Regenerative Dose (SAR) | 44 |

| | |
|-------------------------------------|----|
| 2.2.1.5 Standard Growth Curve (SGC) | 47 |
| 2.2.1.6 NCF-SAR | 47 |
| 2.2.1.7 Experimental errors | 48 |
| 2.2.2 Measurement of Dose rate | 50 |
| 2.2.3 Analysis | 50 |
| 2.2.3.1 Common Age Model | 51 |
| 2.2.3.2 The Central Age Model | 51 |
| 2.2.3.3 Minimum Age Model | 52 |
| 2.2.3.4 Finite Mixture Model | 53 |

Chapter 3: Chronology of Aeolian sequences

| | |
|--|----|
| 3.1 Introduction | 55 |
| 3.2 Wahiba Sands | 56 |
| 3.2.1 Sample Description | 56 |
| 3.2.2 Experimental details | 56 |
| 3.2.3 Results | 57 |
| 3.3 Mexico dunes | 65 |
| 3.3.1 Sample Description | 65 |
| 3.3.2 Methods used | 65 |
| 3.3.3 Results | 65 |
| 3.4 Thar desert | 73 |
| 3.4.1 Sample description | 73 |
| 3.4.2 Methods used | 73 |
| 3.4.3 Results | 73 |
| 3.5 Single grain dose distribution | 73 |
| 3.6 Explanation for the spread in dose distribution | 77 |
| 3.6.1 Bioturbation | 77 |
| 3.6.2 Heterogeneous bleaching | 81 |
| 3.6.3 Variations in the luminescence characteristics | 81 |
| 3.6.4 Variations in the microdosimetry | 81 |
| 3.7 Summary | 84 |

Chapter 4: The Spatial Heterogeneity of Beta Dose in Sediments

| | |
|------------------------------|----|
| 4.1 The problem | 85 |
| 4.2 Mathematical Formulation | 89 |

| | |
|--|-----|
| 4.2.1 Dose-distance relationship | 89 |
| 4.2.2 Dose distribution | 91 |
| 4.2.3 Solution of dose distribution | 96 |
| 4.2.3.1 Numerical Approach | 96 |
| 4.2.3.1.1 Numerical Laplace Inversion | 99 |
| 4.2.3.1.2 Analytical method | 101 |
| 4.2.4 Results and Discussion | 107 |
| 4.3 Summary | 108 |
| Chapter 5: Implication of spatial heterogeneity of beta dose in sediments | |
| 5.1 Introduction | 112 |
| 5.2 Influence of partial bleaching on dose distribution | 114 |
| 5.3 Age Equation | 120 |
| 5.3.1 Dose | 124 |
| 5.3.2 Dose Rate | 128 |
| 5.4 Conclusion | 136 |
| Chapter 6: Conclusion and Future outlook | 137 |
| References | 140 |
| List of Publications | 149 |

| | |
|--|-----|
| 4.2.1 Dose-distance relationship | 89 |
| 4.2.2 Dose distribution | 91 |
| 4.2.3 Solution of dose distribution | 96 |
| 4.2.3.1 Numerical Approach | 96 |
| 4.2.3.1.1 Numerical Laplace Inversion | 99 |
| 4.2.3.1.2 Analytical method | 101 |
| 4.2.4 Results and Discussion | 107 |
| 4.3 Summary | 108 |
| Chapter 5: Implication of spatial heterogeneity of beta dose in sediments | |
| 5.1 Introduction | 112 |
| 5.2 Influence of partial bleaching on dose distribution | 114 |
| 5.3 Age Equation | 120 |
| 5.3.1 Dose | 124 |
| 5.3.2 Dose Rate | 128 |
| 5.4 Conclusion | 136 |
| Chapter 6: Conclusion and Future outlook | 137 |
| References | 140 |
| List of Publications | 149 |

Figures

Page

Chapter 1: Luminescence Dating: A perspective

- | | | |
|-----|---|----|
| 1.1 | Physics of luminescence chronology. Band diagram of a) Pure crystal, b) with impurities, c) during irradiation of nuclear radiation and d) stimulated emission | 4 |
| 1.2 | Possible processes of excitation of a luminescence centre (after Krbetschek et al., 1997) | 6 |
| 1.3 | Event can be dated. I shows the latent luminescence acquired since the formation of the crystal or any luminescence signal before it was exposed to light, II shows the luminescence acquired due to the natural radioactive elements in the surrounding since the deposition and III shows the regenerated dose response curve using laboratory irradiation | 8 |
| 1.4 | The TL glow curve of quartz from sedimentary origin (of two sub samples; open and filled circles). There are three main TL peaks centered at 110°C, 325°C and 375°C | 15 |
| 1.5 | The Blue stimulated luminescence in UV emission band. The stimulated photons flux was constant throughout the stimulation duration i.e., conventionally called cw-OSL | 16 |
| 1.6 | LM-OSL of the quartz in UV emission where the Blue light photons flux was ramped linearly during stimulation | 18 |
| 1.7 | Empirical model of quartz in UV emission band (after Bailey 2001) with 5 trapping centers and 4 recombination centers | 19 |
| 1.8 | Solar Spectrum: outside the atmosphere and at sea level with the sun 60°C below zenith (Oriel Solar Simulator handbook, based on works by M.P. Thekaekara; taken from Aitken, 1998) | 21 |
| 1.9 | Solar spectra at various depths of water column (after Berger 1990). The sedimentation concentration was in the range 15-21 mg.l ⁻¹ | |

| | |
|--|----|
| (taken from Aitken, 1998) | 21 |
| 1.10 Bleaching efficiency verses wavelength (after Spooner 1994) of quartz (taken from Aitken, 1998) | 22 |
| 1.11a The probability distributions for $p=0.01, 0.02, 0.05$ and 0.1 . These are equivalent to the contamination of a well-bleached sample by 1 %, 2 %, 5 % and 10 % of unbleached grains, respectively (after Olley et al., 1999) | 25 |
| 1.11b The probability of selecting only well-bleached grains in aliquots consisting of n grains, versus the proportion of unbleached grains in a sample (after Olley et al., 1999) | 25 |
| 1.12. Checking partial bleaching in samples using the replacement plot (taken from Bailey, 2003a). Open circles are from the natural sample and the closed circles are from the laboratory bleached aliquots | 29 |
| 1.13. The flow diagram of optimizing the usage of method for dose distribution based on some statistical parameters (after Bailey and Arnold, 2006). CAM and MAM are Central Age Model and Minimum Age Model respectively. The critical values for skewness and kurtosis are the result of the simulation results. For more details see Bailey and Arnold, 2006 | 31 |
| 1.14. Single quartz grains dose distribution from Allen's cave deposits from southern Australia (after Murray and Roberts, 1997). First ever observed bimodal dose distribution | 33 |

Chapter 2: Experimental details and Methodology

| | |
|---|----|
| 2.1 Stimulation and detection unit (taken from Internal Report, Risø National Laboratory, Denmark). IR-LEDs and Blue LEDs are used for optical stimulation and linear rate heating for thermal stimulation. Standard bi-alkali photomultiplier tube EMI 9235QA is the photon detection unit | 37 |
|---|----|

| | | |
|---------|--|----|
| 2.2 | Emission band of a typical quartz after optical stimulation at the wavelength of 614 nm (after Huntley et al., 1991) | 40 |
| 2.3. | Schematic diagram of Risø Single Grain OSL reader (taken from Internal Report, Risø National Laboratory, Denmark) | 41 |
| 2.4 | Irradiation unit (taken from Internal Report, Risø National Laboratory, Denmark). 40 mCi activity $^{90}\text{Sr}/^{90}\text{Y}$ beta source is the irradiation unit | 41 |
| 2.5(a). | Schematic diagram explaining multiple aliquot additive dose method. The open circles are the naturally accrued luminescence points while the closed ones are the laboratory irradiated luminescence points. Each dose points are from 3-5 aliquots | 43 |
| 2.5(b). | Actual measurement of multiple aliquot additive dose method of Wahiba sands from Oman. The 0.1s short shine normalization was done for all the aliquots | 43 |
| 2.6 | Schematic diagram explaining multiple aliquot regenerative dose procedure. The open circles are the naturally accrued luminescence points while the closed ones are the laboratory irradiated luminescence points. Each dose points are from 3-5 aliquots | 45 |
| 2.7 | Proportion of bright grains in the sample. Normally it is 5 – 10 % of grains are bright. This is for sand grains from Wahiba sands | 45 |
| 2.8(a) | Schematic diagram explaining the single aliquot regenerative dose procedure (SAR; Murray and Wintle, 2000). Filled circles shows the laboratory irradiated luminescence points and the open circle is the luminescence due to natural ambient radiation environment. The shaded circle point is used to calculate the recyclic ratio which is the ultimate measure of the sensitivity changes during the measurement procedure | 46 |
| 2.8(b) | Estimation of D_e using SAR procedure for 6L3 (Wahiba | |

| | |
|--|----|
| sands from Oman). The growth curve is fitted to single saturating exponential function | 46 |
| 2.9 Sequence for NCF-SAR protocol. The shaded steps are the additional ones to the normal SAR sequence | 49 |

Chapter 3: Chronology of Aeolian sequences

| | |
|---|----|
| 3.1 The dose response curve (growth curve) using SAR procedure for Oman samples, a) 1L1 and b) 5L2. The inset shows the OSL decay curve | 58 |
| 3.2 A typical MAAD growth curve of sample 6L3 | 59 |
| 3.3 Standard growth curve obtained using 10 aliquots of 6L3 | 59 |
| 3.4. The dose response curve of 7L3 and the effect of natural sensitivity correction in obtaining De value | 60 |
| 3.5. Preheat plateau of 1L1. Preheat 260°C was used for the De measurements | 60 |
| 3.6 The dose recovery test for the sample 7L3 of Wahiba sands | 61 |
| 3.7 Histograms of dose distribution of Wahiba sands. The bin width is the median value of the individual error | 63 |
| 3.8. The SAR dose response curve for sample GD03-13 (oldest sample). The inset shows the shine down curve | 66 |
| 3.9 Histogram of dose distribution Gran Desierto sample | 67 |
| 3.10 The growth curve and shine down curve of GPR-09 (Thar desert sample) | 74 |
| 3.11 Dose distributions of Thar desert samples | 75 |
| 3.12 Comparison of dose distributions of single aliquot and single grain measurements, a) 1L1, b) 5L2, c) GD03-13 and d) GPR-09 | 78 |
| 3.13 Comparison of RSD (%) from the single aliquot and the single grain measurements of 22 samples. The same data set is tabulated in Table 3.4 | 79 |

| | | |
|------|--|----|
| 3.14 | Replacement plot of one well bleached sediment (1L1) and one partially bleached sediment (RB3) | 82 |
| 3.15 | Dose deposition of ^{40}K 's beta in the quartz grain | 82 |
| 3.16 | Schematic diagram for showing spread in dose distribution due to type of distribution of potassium source particles | 83 |

Chapter 4: The Spatial Heterogeneity of Beta Dose in Sediments

| | | |
|------|---|-----|
| 4.1a | Distribution of quartz (open circles) grains and ^{40}K hotspots (closed circles) | 88 |
| 4.1b | Schematic of dose delivered to a grain located at the centre of the coordinate system. The circle represents the volume of interest and its radius is the maximum range of beta particles from potassium (^{40}K) | 88 |
| 4.2 | Normalized beta-range spectrum of ^{40}K fitted to Eq. (4.30) | 92 |
| 4.3 | Derived dose distance relationship $g(\rho)$ a) in linear scale and b) in logarithmic scale based on the Eq. (4.12) | 97 |
| 4.4 | Verification of Bellman method of numerical Laplace inversion with the known exact function xe^{-2x} | 102 |
| 4.5 | Verification of Piessen method of numerical Laplace inversion with the same known function xe^{-2x} | 102 |
| 4.6 | Comparison of Bellman and Piessen method of numerical Laplace inversion with the known function xe^{-2x} | 103 |
| 4.7 | Obtained dose distribution function for $K=0.5\%$ by both Bellman and Piessens methods | 103 |
| 4.8 | Dose distance relationship used for analytical [Eq. (4.52)] and numerical [Eq. (4.12)] approaches. | 105 |
| 4.9 | Appropriate Integration contour | 105 |
| 4.10 | The dose distribution obtained by analytical approach for number of hotspots (μ) of 84 | 109 |
| 4.11 | Comparison of dose distribution by analytical and | |

| | | |
|------|--|-----|
| | numerical approaches for number of hotspots (μ) of 84 | 109 |
| 4.12 | Dose distribution and fitting to modified Gumbel distribution given in Eq. (4.74) | 110 |
| 4.13 | Dose distribution results for various K values | 110 |
| 4.14 | Exponential saturation of the 'p' factor with increasing K concentration following the empirical functional form given in Eq. (4.75) | 111 |
| 4.15 | Decreasing of RSD with increasing K concentration | 111 |

Chapter 5: Implication of spatial heterogeneity of beta dose in sediments

| | | |
|------|--|-----|
| 5.1 | (a) The burial dose distribution arising because of the K hotspots in the sample matrix shown in scaled dose and (b) in real dose. Here D is the dose, \bar{D} is the mean dose and $\Phi(D)$ is the dose distribution | 113 |
| 5.2. | Palaeodose distribution in modern surface samples from Aeolian contexts. (redrawn from Bush and Feathers, 2003). The distribution has been fitted to an exponential decay function | 115 |
| 5.3 | Palaeodose distribution in modern surface samples from Fluvial contexts. (redrawn from M. Jain, 2007). All the dose distributions are fitted to an exponential decay function | 116 |
| 5.4 | Assumed truncated negative exponential distribution of the partially bleached dose with the normalized mean value | 118 |
| 5.5 | (a) Measured dose distribution of well bleached sample, (b) Experimental error distribution obtained from the dose recovery experiment for an administered dose ~ 12 Gy | 119 |
| 5.6 | Resulting dose distribution after deconvoluting the experimental error distribution (Fig. 5.5b) from the measured distribution (Fig. 5.5 a) dose distribution. There is no effect in deconvoluting the experimental error distribution | |

| | | |
|-------|--|-----|
| | from the measured dose distribution and that is seen in the indistinguishableness of the two curves. | |
| | See text for the details | 121 |
| 5.7 | Graphs showing the burial dose distribution and the convoluted distribution with the truncated exponential (partial bleached) distribution. a) 90 % dose unbleached b) 70 % of dose c) 30 % of dose and d) 10 % of dose was unbleached | 122 |
| 5.8. | a) The burial dose distribution arises from the 0.5 % of K concentration present in the sample. The oscillations in the lower dose side and in higher dose side are clearly seen and it is attributed to small variations in the values used in the numerical approach for the Laplace Inversion and b) the lower dose side is zoomed in so that the nature of oscillations could be noticed | 125 |
| 5.9 | Sensitivity changes with many measurements. Dashed line show the 30 % increase in sensitivity after the first measurement | 126 |
| 5.10 | Natural radioactive nuclide measurements from the 3758 samples. [taken from Ankjaegard, et al., 2006] | 130 |
| 5.11 | Murray and Roberts data with theoretically obtained dose distribution for the K concentration of the given sample | 131 |
| 5.12. | Comparison of model obtained age with the reported age and the mean age | 135 |

Tables

Page

Chapter 1: Luminescence Dating: A perspective

- 1.1 Details about the luminescence emission of quartz and the method used to investigate it. TL, PL, CL and RL stands for thermoluminescence, photoluminescence, cathodoluminescence and radioluminescence respectively.

12

Chapter 3: Chronology of aeolian sequences

- 3.1 Wahiba sands results
3.2 Mexico dunes samples results
3.3 Thar desert samples results
3.4 Comparison of RSD of single aliquot and single grain dose Distribution

64

71

76

80

Chapter 5: Implication of spatial heterogeneity of beta dose in sediments

- 5.1 Natural radioactive nuclide concentration of 3758 samples (from Ankjærgård et al., 2006)
5.2 Detailed tabulation of results after applied our modified age equation for Wahiba, Mexico and Thar desert samples

130

134

Chapter 1

Luminescence Dating: A perspective

1.1 Introduction

Concerns on anthropogenically caused global changes have now necessitated a detailed understanding of the earth's climatic system and the modes of its natural variability. Only then will it be possible to quantify the net effect of changes caused by human activities. Such an effort is necessary, to have a prediction of the future climate state and net ecosystem changes, based on a comparison with palaeoanalogues. The instrumental records of climate (i.e. humidity and temperature) are available for the past two centuries only. Historical records also are often limited to only a few centuries. Extension of these records, using geological archives, therefore becomes necessary and presently variety of palaeoarchives are being used to reconstruct past climate. This involves analysis of isotopic and other physical attributes of tree rings, corals, speleothems and the sedimentary records on the land and in ocean. Towards studying the sedimentary records, several radiometric dating techniques exist. The radiocarbon dating technique has been one of the useful

techniques for the recent earth history. This method however has a small time range of dating (~40 ka), a limited applicability to carbon containing organic matter and carbonate sediments has problems of post deposition contamination due to diagenesis, and suffer from difficulties of uniquely establishing the association of sediment stratum and the sample being dated. Further the ages need a calibration that results in enhanced error in age despite a high measurement precision. Other methods such as uranium series disequilibrium methods have high precision of <1% and extended dating range of ~300ka, however suffer from limited applicability to pure carbonates, that are difficult to obtain in terrestrial settings. Relative dating methods such as palaeomagnetism, need secondary age controls such as volcanic ashes. These are often not easy to find in a desired stratigraphic context and even in most opportune cases, an interpolation of age between securely dated volcanic horizons is needed using an assumed sedimentation rate.

It is in this context that the recent developments of luminescence dating make it a preferred method for the dating of terrestrial records and processes. The method provides the age of deposition of a sediment layer using the radiation exposure to minerals constituting it. This eliminates the ambiguity in correlating the sample with the strata. The dating range is sample dependent and can range from 10a to 1Ma. The most important aspect is its ability to deal with various facies of a sedimentary layer, be it sediments representing diverse depositional environments, volcanic ashes or authigenic precipitates and the like. This provides for a self consistent numerical chronometric frame work, not possible with any other method. There are however problems of details, the complexities of radiation environment and its spatial distribution and temporal behavior, and the complexities of the solid state, which ensures that no two grains of a same mineral type are identical. These call for a careful examination of these aspects for every sample, making the application, a rigorous and a time consuming effort.

This thesis concerns the radiation dosimetric aspects of luminescence dating of sediments and aims to further refine the existing methodologies relating to the interpretation and computation of ages based on the analysis of single grains. Single grain analysis provides the best possible scenario of dating sediments, however there are finer details of sample analysis that need attention for a robust application of the method. One such improvement that is needed relates to the quantification of

radiation environment. This thesis investigates the causes and the impact of heterogeneity of radiation environment at a single grain level on luminescence ages and attempt to develop a conceptual formalism to deal with such heterogeneity by providing a more elaborate age equation. Analytical studies and application to real samples, suggest that the calculation and the formalism developed are robust. This chapter deals with the basic luminescence phenomena particularly relating to natural quartz along with an overview of luminescence dating.

1.2 Luminescence dating: Basic principles

The physical basis of luminescence process in minerals can be explained using the band theory of solids (Fig 1.1a). Here the allowed energy levels form a continuum and are separated from the filled states by an energy band gap termed forbidden energy gap. For silicate minerals like quartz, the band gap (E_g) is large (~ 8.6 eV) and in such cases, at room temperature, the lower continuum (the valence band) is filled and the upper energy continuum (the conduction band) is empty. Energy states are not allowed in the forbidden gap. This is the case with the pure crystal. In nature however, during the crystallization of minerals, some of the ions in the host crystals are replaced by impurities. The nature of the impurities incorporated is determined by the impurity concentration, its ionic radii and the cooling rate of the mineral. Presence of these impurities leads to localized energy states which are represented by isolated states in the forbidden band gap (Fig. 1.1b). Depending on their electronic nature, these impurity states serve as charge traps capable of trapping either an electron or a hole. The electron traps are near the conduction band and the hole traps near the valence band. The binding energy (i.e., residence time) of the trapped charges depends on the electronic structure and crystal fields around an impurity. Irradiation by, α , β , γ and cosmic rays induces ionization and electrons and holes thus created, diffuse through the crystal lattice. Most of them recombine instantaneously, heating the crystals and a few get trapped (Fig. 1.1c). Depending on their charge environment they remain trapped for variable time scales, ranging from few seconds to several million years. The concentration of trapped charges is cumulative such that it increases with increasing irradiation till a saturation level is reached. Since the half lives of the radioactive elements in the environment such U, Th and K are several billion years, the flux of the ionizing radiation can be assumed to be a constant over

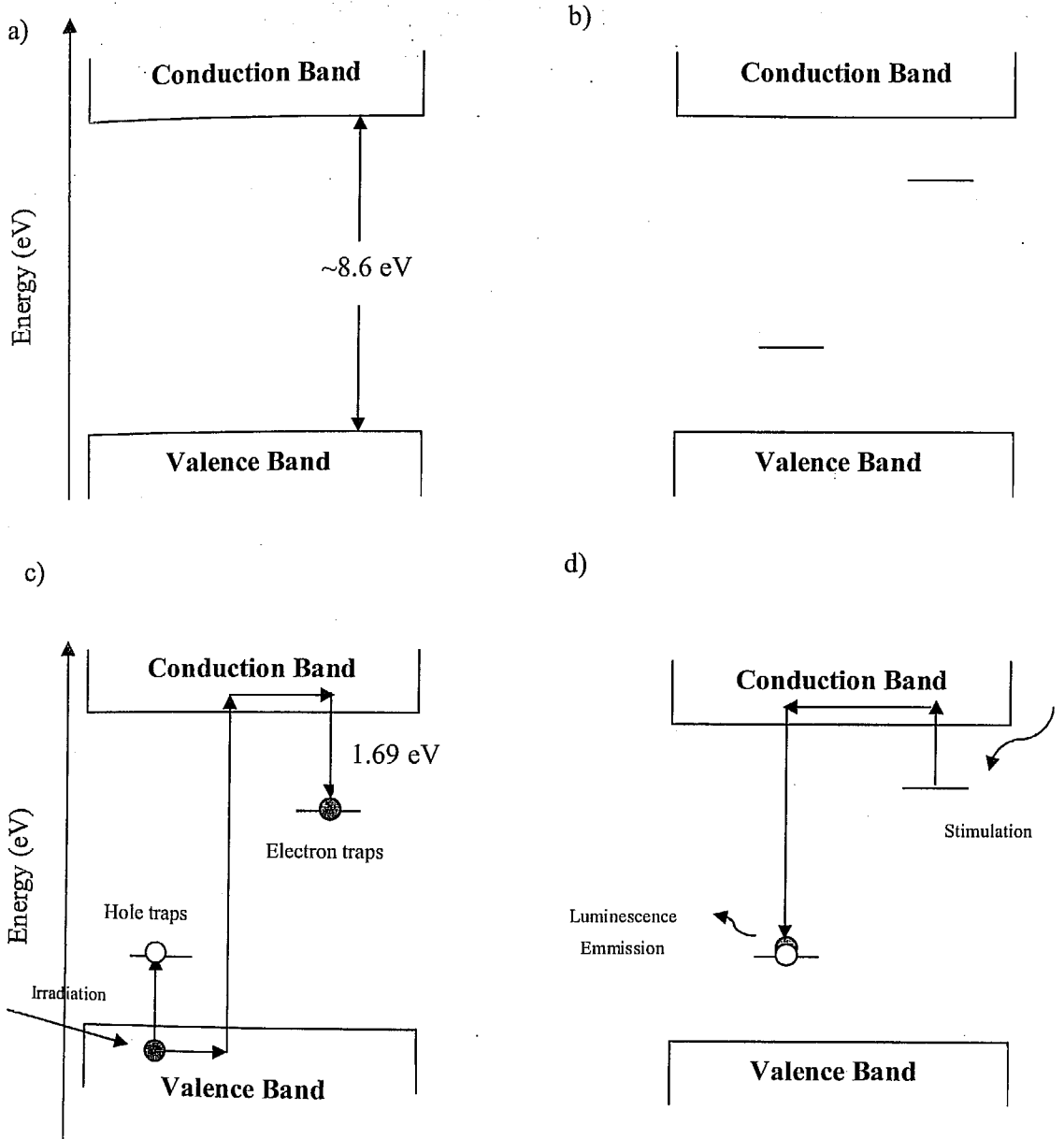


Figure 1.1 Physics of luminescence chronology. Band diagram of a) Pure crystal, b) with impurities, c) during irradiation of nuclear radiation and d) stimulated emission.

million year time scales. Given that the mean residence time in deeper traps is large, it implies then that the trapped charge concentration in such traps will increase in a cumulative manner, related only to time and irradiation (i.e., dose rate). Thus a measurement of the trapped charge concentration and annual irradiation rate leads to the age of the sample. The trapped charges can be detrapped by a thermal or optical stimulation. These move in the lattice and some of these radiatively recombine at appropriate recombination centers to produce luminescence. The colour of the luminescence is determined by the nature of recombination of centers (Fig. 1.1d).

The process of excitation and emission of an individual center participating in a luminescence process can also be described using a configuration coordinate diagram. Figure 1.2 shows the potential energy curves of the absorbing center as a function of the relative distance R of the nucleus to the equilibrium position (electron in the ground state). Figure 1.2 shows excitation and radiative (I) and non-radiative (II) transitions to the ground state. A particular case of thermally assisted excitation (III) into the conduction band and the relationship between the configuration coordinate and the band model are also shown. Following an excitation to a higher state, the electron can escape to the conduction band by phonon absorption and recombine with other activators. This process is called thermally assisted emission. This is the most likely process in Feldspars (Hütt et al., 1988). The horizontal displacement ΔR results in line broadening. Larger the ΔR broader is the absorption and the emission bands. The displacement is temperature dependent and hence the radiationless return to the ground state becomes more important at higher temperatures. This radiationless return is called thermal quenching.

1.3 Event that can be dated using Luminescence

Luminescence methods provide the age (time elapsed) since a “zeroing” event that caused de-trapping of all the trapped charges that a sample acquired during its geological antiquity, to a zero or near zero residual value. The events that are dated by this methods are, 1) the most recent heating event (for the case of pottery, contact baked clay, sediments contact heated by lava flows etc.), 2) the most recent daylight exposure event (all sediments transported by wind, water, ice such as loess, glacier debris, sand dunes, alluvial and colluvial sediments etc.) and, 3) mineral formation event (gypsum, halite, carbonates, volcanic ashes etc.) (Singhvi and Wagner, 1986).

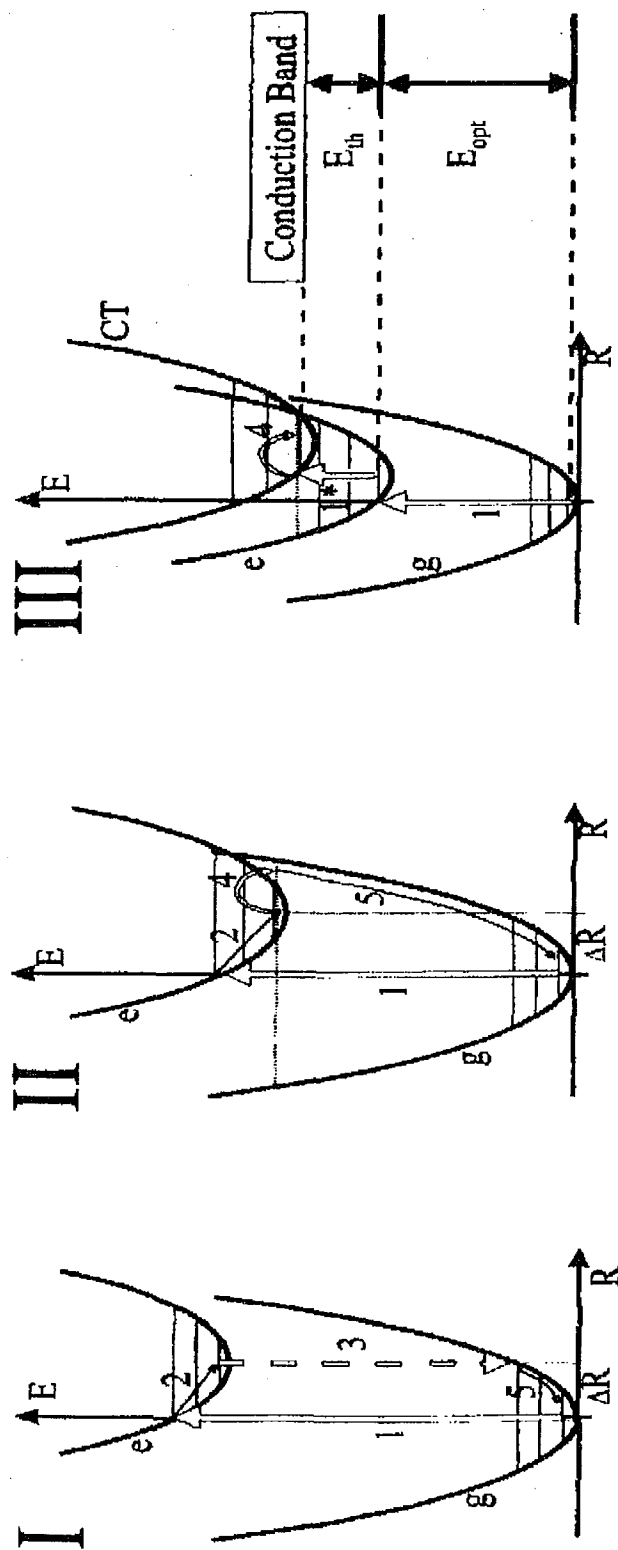


Figure 1.2 Possible processes of excitation of a luminescence centre (after Krbetschek et al., 1997).

In case of heating event the luminescence clock is reset to zero by heating the sample to around 500°C. In second case, daylight exposure during weathering and transport provides results in photo-bleaching of the trapped charges leaving a near zero trapped charge concentration and make the luminescence clock reset. After transportation, the grains are buried, the day light exposure ceases and re-accumulation of trapped charges, due to irradiation from the ambient radiation is initiated. This re-accumulation continues till excavation or till reworking of the sediment (Fig 1.3). The third case is the mineral formation event, where the accumulation of luminescence signal is initiated at time of crystal nucleation, and the event dated is the formation time of minerals (gypsum, halite, carbonates, etc.).

1.4 The age equation

In geological settings the decay of naturally occurring radionuclide such as ^{40}K , ^{238}U , ^{235}U , ^{230}Th and ^{80}Rb provide a natural radiation environment (NRE). NRE comprises alpha, beta and gamma radiations along with a small contribution from cosmic rays reaching the earth's surface. These radiations interact with minerals constituting the sediment and deposit energy in them in the form of trapped charges. The ionization efficiency of alpha particles is much higher than beta particles and gamma rays on account of their higher mass and higher charge. The linear energy transfer (LET) of alpha is higher than that of beta and gamma and the energy deposition occurs over a much shorter track length. This leads to a charge saturation vis a vis total trapping centres available /unit volume. The beta particles have a low LET and deposit their energy up to a range of ~2 mm in quartz or feldspar. Due to the straggling effects, the beta energy is deposited in a cylindrical volume with the radius of ~500 μm (Wang and Li, 2001). The gamma energy is deposited via the production of secondary electrons which then deposit their energy in a manner similar to beta particles, uniformly in the crystal. Considering all the above facts, the age equation becomes,

$$\text{Age} = \frac{L}{\chi_{\alpha}\dot{D}_{\alpha} + \chi_{\beta}\dot{D}_{\beta} + \chi_{\gamma}\dot{D}_{\gamma} + \chi_{CR}\dot{D}_{CR}} \quad (1.1)$$

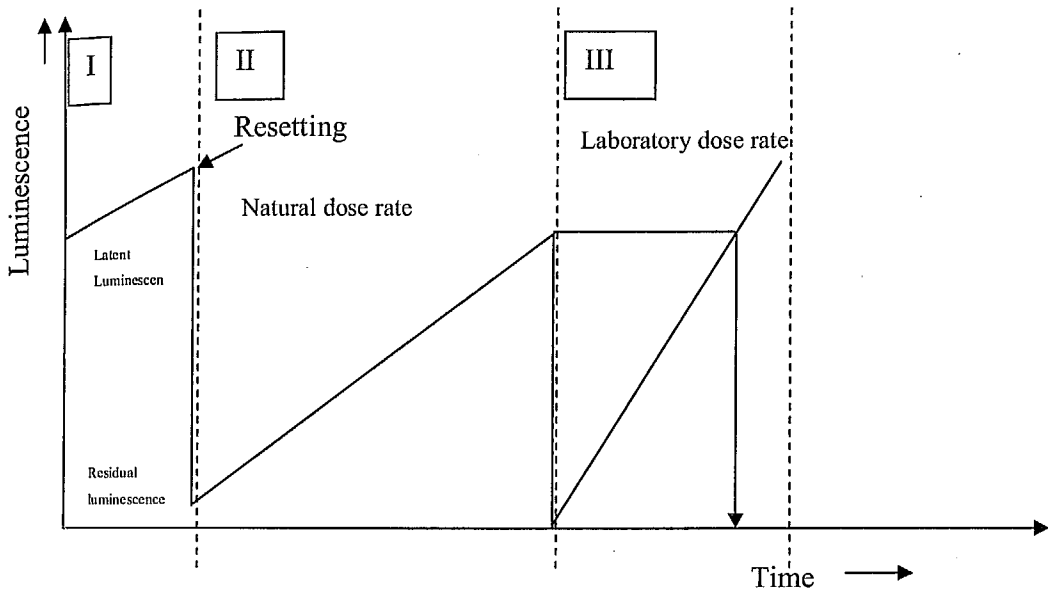


Figure 1.3 Event can be dated. I shows the latent luminescence acquired since the formation of the crystal or any luminescence signal before it was exposed to light, II shows the luminescence acquired due to the natural radioactive elements in the surrounding since the deposition and III shows the regenerated dose response curve using laboratory irradiation.

where \dot{D} is the dose-rate and χ is the luminescence sensitivity of quartz to particular nuclear radiation. The age equation changes depending on whether the size of the sediment grains is comparable to alpha range or much larger than this range. These leads to grain size based analysis protocols. The fine grain method uses fine silt (4-11 μm) and assumes full alpha dose and the coarse grain method uses $> 90\mu\text{m}$ and assumes that alpha particles only affected the outer skin of the grain and this is etched away to leave the interior portion that was unaffected by alphas particles.

In the present thesis, only the coarse grain technique was used. The alpha irradiated skin was removed by etching the outer $\sim 20 \mu\text{m}$ skin of the crystal using 40% hydrofluoric acid (HF) for 80 minutes. Because of this etching $\sim 10 \%$ of the beta contribution also gets lost this was considered in the age equation. Luminescence sensitivity of quartz to beta, gamma and cosmic radiations is the same compare to alphas because of their low LET property. The age equation then transforms to,

$$Age = \frac{L}{\chi_{\beta} [0.9 \times \dot{D}_{\beta} + \dot{D}_{\gamma} + \dot{D}_{CR}]} \quad (1.2)$$

$$Age = \frac{L / \chi_{\beta}}{0.9 \times \dot{D}_{\beta} + \dot{D}_{\gamma} + \dot{D}_{CR}} \quad (1.3)$$

$$Age = \frac{D_e}{0.9 \times \dot{D}_{\beta} + \dot{D}_{\gamma} + \dot{D}_{CR}} \quad (1.4)$$

where, D_e is the laboratory beta dose that produces a luminescence equal to the natural luminescence and is termed as the palaeodose (P) or equivalent dose (D_e).

1.5 Luminescence characteristics of Quartz

SiO_2 (silica) makes up 12.6 % by weight of the Earth's crust it occurs in crystalline and amorphous forms. Depending on the temperature and pressure conditions at the time of formation, it can have 14 structural forms. The most common form is trigonal α -quartz which exclusively comprises $[\text{SiO}_4]^{4-}$ tetrahedron with all oxygens joined together in a three-dimensional system. Under normal atmospheric pressure, α -quartz transforms into hexagonal high-temperature quartz (beta-quartz) at 575°C . The conversion occurs by changes in the bond angle of the oxygen rings accompanied by an enlargement of the crystal lattice. A reverse process takes place during magmatism,

where β -quartz transforms into α -quartz during cooling. As perfect crystal structures do not exist in nature, the luminescence properties of quartz are determined by its defect states. The type of lattice defects depends on the thermodynamic conditions during mineralization. Lattice defects in quartz can be classified according to their structure and size such as, point defects, translational defects such as line and planar imperfections (Kittel, 2002), inclusions of paramagnetic impurities and gas/liquid inclusions. Generally, about 20 different types of paramagnetic defect centers have been observed. These can be subdivided into two main types viz. 1) defects caused by foreign ions and, 2) centers associated with vacant oxygen or silicon positions. Substitution of silicon atoms in the lattice is rare because of the small ionic radius of Si^{4+} (0.42 \AA) and its high valence. So far Al^{3+} (0.51 \AA), Ga^{3+} (0.62 \AA), Fe^{3+} (0.64 \AA), Ge^{4+} (0.53 \AA), Ti^{4+} (0.64 \AA) and P^{5+} (0.35 \AA) have been detected as substitutional impurities. Nuttall and Weil (1980) reported a hydrogenic trapped hole-center with four hydrogen atoms on a silicon lattice position. Al is the most frequent trace element in quartz (up to a few hundreds ppm). Its incorporation into quartz is explained by its common occurrence in the Earth's crust and by their similar ionic radii. Since, compensation of the electric charge is necessary, in the case of certain elements, additional cations such as H^+ , Li^+ , Na^+ , K^+ , Cu^+ , Ag^+ get incorporated at interlattice locations in conjunction with structural channels. The possible incorporation of other cations in these positions (e.g. Ni^+ , Al^{3+} , Fe^{3+} , Co^{3+} , Cr^{3+} , Ti^{4+}) is still being discussed. The second type of defect is attributed to the group with E' and O^{2-} centers, the best known of which is the E_1' center, an oxygen vacancy center. The oxygen tetrahedron is transformed into a planar arrangement of three oxygen ions. The center can exist in three different stages E_1^0 , E_1' and E_1'' corresponding to its thermal stability and its reaction with respect to the impinging irradiation. The luminescence emission may be from the bulk of the material itself or from isolated impurities, clustered defects or grain boundary impurities. Different types of quartz luminescence have been investigated and these provide useful information about the nature of luminescence centers and their distribution in quartz. These reflect specific conditions during quartz formation and can provide a fingerprint of its origin. Despite considerable number of luminescence studies on quartz, a clear correlation between observed emissions and luminescence activators/ lattice defects, has not yet been achieved, due primarily to the complexity of the solid state. Characteristic

emission bands in the luminescence spectra and their possible correlation to particular types of activators or defects are listed in Table 1.1. The luminescence of SiO_2 is weak, and highly variable depending on the manner of its formation or alteration due to pressure and temperature conditions at the time of formation. Generally, crystalline SiO_2 and amorphous silica show similar luminescence emission bands. In the visible region, luminescence of natural quartz consists of two broad emission bands centered around 450 nm (blue emission) and 650 nm (red emission). The blue luminescence band usually comprises overlapping component bands of different polarization and quenching temperatures. Gortén et al., (1996) used a phase-tuning technique to isolate and identify the lines from different centers. They found four major components of the blue cathodoluminescence emission band at 390 nm, 420 nm, 450 nm and 500 nm in a suite of the synthetic and natural quartzes. The 380-390 nm emission is sensitive to radiation and correlates well with the concentration of Al and paramagnetic $[\text{Al/M}^+]$ centers. The 420 nm emission band is related to a radiation produced intrinsic defect i.e., self-trapped exciton emission. Previously, this emission was associated with various other defects such as a carbon impurity, an - O - O - type defect or O^{2-} defects. Rink et al., (1993) observed that the TL emission at 420-435 nm exclusively occurs in igneous quartz of volcanic and granitic origin. Luminescence emission between 500 and 440 nm (2.5 and 2.8 eV) in crystalline SiO_2 and between 565 and 515 nm (2.2 and 2.4 eV) in amorphous SiO_2 have been observed. Emission bands at 175 nm and at 290 nm have been related to intrinsic defects. In contrast, the emission in the IR around 700 nm is assumed to be due to the substitution incorporation of Fe^{3+} into the quartz lattice. Reviews by Krbetschek et al. (1997) and Götze et al. (2001), provide detailed description on the spectral emissions from quartz.

1.5.1 UV emission of quartz: TL and OSL

In case of quartz a single trap and a single recombination center, with no retrapping, the decrease in the number of trapped charges (Randall and Wilkins, 1945) is given by

$$-\frac{dn}{dt} = I \quad (1.5)$$

Table 1.1 Details about the luminescence emission of quartz and the method used to investigate it. TL, PL, CL and RL stands for thermoluminescence, photoluminescence, cathodoluminescence and radioluminescence respectively.

| EMISSION | IDENTIFICATION | METHOD |
|------------------------------|---|------------|
| 175 nm (7.3 eV) | Intrinsic emission of pure SiO ₂ | CL |
| 290 nm (4.28 eV) | E' center (oxygen vacancy) | PL, CL |
| 330 - 340 nm (3.75 - 3.6 eV) | E' center (oxygen vacancy), [AlO ₄ /Li ⁺] center, [TiO ₄ /Li ⁺] center | TL |
| 380 - 390 nm (3.2 - 3.1 eV) | [AlO ₄ /Li ⁺] center, M ⁺ = Li ⁺ , Na ⁺ , H ⁺ & [H ₃ O ₄] ⁰ hole center | RL, CL, TL |
| 420 nm (2.9 eV) | Intrinsic emission, Self-trapped exciton | CL, RL |
| 470 - 500 nm (2.6 - 2.45 eV) | [AlO ₄] ⁰ center, Extrinsic emission, [GeO ₄ /M ⁺] ⁰ center | CL, RL, TL |
| 510 - 570 nm (2.4 - 2.2 eV) | Self-trapped exciton due to Ge bond breaking Oxygen vacancy | CL |
| 580 nm (2.1 eV) | Oxygen vacancy | TL, CL |
| 620 - 650 nm (1.97 - 1.9 eV) | Non-bridging oxygen ions E' center (oxygen vacancy), Na ⁺ , H ⁺ , OH ⁻ , Non-bridging oxygen hole center with several precursors (e.g. hydroxyl group, peroxy linkage) | PL, CL |
| 700 nm (1.71 eV) | Substitutional Fe ³⁺ | CL, PL |

where n is the concentration of trapped charges, I is the luminescence intensity. If n_c is the concentration of free charges in conduction band, m is the trapped holes, n is the total trapped charge, then charge neutrality will imply $(n + n_c) = m$ and quasi equilibrium condition will imply $-\frac{dn_c}{dt} \approx 0$.

The relation for first order kinetics is

$$-\frac{dn}{dt} \propto n \quad (1.6)$$

i.e.

$$-\frac{dn}{dt} = pn \quad (1.7)$$

where p is the detrapping probability. If thermal energy is the stimulation source and the thermal energy at a particular temperature is given by Maxwell and Boltzmann distribution then we have

$$-\frac{dn}{dt} = ns \exp\left[-\frac{E_t}{kT}\right] \quad (1.8)$$

where E_t is the trap depth. The above equation has the solution,

$$n(t) = n_0 \exp\left(-s \int_{t_0}^t \exp\left[-\frac{E_t}{kT}\right] dt\right) \quad (1.9)$$

If the temperature varies linearly with time i.e., $T = T_0 + \beta t$ where T_0 is the initial temperature and β is the heating rate then

$$n(T) = n_0 \exp\left(-\frac{s}{\beta} \int_{T_0}^T \exp\left[-\frac{E_t}{k\theta}\right] d\theta\right) \quad (1.10)$$

where θ is a dummy variable representing temperature. After inserting this $n(T)$ in eqn. (1.5),

$$I_{TL}(T) = sn_0 \exp\left[-\frac{E_t}{kT}\right] \exp\left(-\frac{s}{\beta} \int_{T_0}^T \exp\left[-\frac{E_t}{k\theta}\right] d\theta\right) \quad (1.11)$$

This equation represents thermally stimulated luminescence (TL) glow curve for a single trap population. For many trap types and a single recombination center, the glow curve has as many peaks, each corresponding to a trap depths and following the same kinetics. A TL glow curve from sedimentary quartz measured in UV emission is shown in Fig. 1.4. Here the peaks occur at 110°C, 140°C, 230°C, 325°C and 375°C.

Among these 110°C, 325°C and 375°C are the common peaks. For dosimetric purpose 325°C and 375°C peaks are used extensively because of their higher stability. As the 325°C peak is optically stimuable the signal from this trap is used in the thesis.

Under optical stimulation, the relevant equation is (Chen and McKeever, 1997),

$$-\frac{dn}{dt} = pn \quad (1.12)$$

where p is the detrapping probability is governed by optical energy such that $p = \phi \sigma$, where ϕ is the flux of stimulating photons and σ is the photo-ionization cross section. Under this situation, the solution for the OSL intensity is given by,

$$I_{OSL} = -\frac{dn}{dt} \quad (1.13)$$

$$I_{OSL} = n_0 p \exp[-pt] \quad (1.14)$$

$$I_{OSL} = I_0 \exp[-t/\tau] \quad (1.15)$$

For traps with different photo-ionization cross section for the incoming photon flux, the net OSL will be a superposition of several single exponentials. Fig. 1.5 shows a combination of two OSL components called fast and medium in terms of their optical bleachability when the sample is stimulated by blue light of ~470nm. These signals arise from 325°C TL peak of quartz after preheating to 240°C at 2°C/s (Smith and Rhodes, 1994).

Instead of a continuous wave stimulation where the stimulation intensity is constant, it is also possible to carry out a ramped optical stimulation with the intensity increasing linearly with time. This is known as the linearly modulated optically stimulated luminescence (LM-OSL; Bulur, 1996). The flux in this case would then be $\phi = \gamma t$, where γ is ramping rate and t is time. Hence,

$$-\frac{dn}{dt} = n\gamma\sigma t \quad (1.16)$$

The solution is,

$$n = n_0 \exp\left[-\frac{\sigma\gamma}{2}t^2\right] \quad (1.17)$$

and the intensity is,

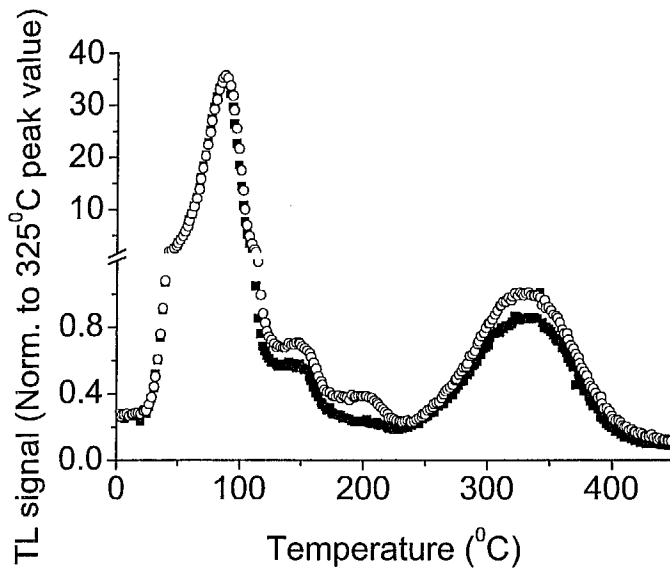


Figure 1.4 The TL glow curve of quartz from sedimentary origin (of two sub samples; open and filled circles). There are three main TL peaks centered at 110°C, 325°C and 375°C.

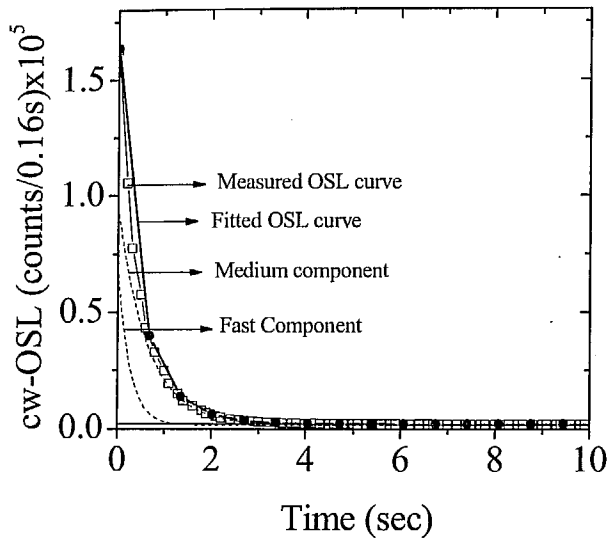


Figure 1.5 The Blue stimulated luminescence in UV emission band. The stimulated photons flux was constant throughout the stimulation duration i.e., conventionally called cw-OSL.

$$I_{OSL} = n_0 \gamma \sigma t \exp \left[-\frac{\sigma \gamma}{2} t^2 \right] \quad (1.18)$$

This is shown in Fig. 1. 6 where the stimulating blue photon flux is ramped from 0 to 40 mW/cm² in 100 s. The UV emission after preheating the sample to 240°C, has two major peaks implying that the first one is the fast and the second one is the medium component in terms of their bleaching rate. This medium component may further comprise many components and the stimulation duration may be a limiting factor to decipher other components. Studies on quartz show that the OSL signal from 325°C TL glow peak comprises up to 7 components (Singarayer and Bailey, 2003, Jain et al., 2003b). Based on the results of all the studies, Bailey (2001) used the UV emission centered on ~380 nm to develop an empirical model for quartz. This model (Fig. 1.7) comprises 5 electron traps and 4 recombination centers. Level 1 is a relatively shallow electron trap giving a TL peak at ~110°C. Level 2 is not a common emission (Bailey, 2001). The Levels 3 and 4 yield TL peaks at 325°C and both give rise to photo-stimulated luminescence signals. These levels also provide the fast and medium OSL components respectively. The terms fast and medium refer to the relative depletion rates of these signals under photo-stimulation. A thermally stable deep trap (termed thermally disconnected trap) is included in the present model (Level 5). From physics point of view, there exists a variety of electron trapping centers with a thermal stability significantly greater than that of Levels 3 and 4. Level 5 is included here as a representation of these centers. In case of hole trapping centers, Level 6 and Level 7 (thermally unstable non-radiative recombination centers) are similar in many respects to the reservoir centre (R center) postulated by Zimmerman (1971). Level 8 is the luminescence center (L center) which is responsible for the OSL and TL emissions at 380 nm. And the Level 9 (thermally stable non-radiative recombination center) represents all recombination centers other than the R centers that are either non-radiative or emit photons at energies outside the UV window. This is the present knowledge on quartz OSL UV emission which is normally used for dosimetric and dating studies.

1.6 Objectives

A key element in luminescence dating of sediments is the assurance of resetting of geological luminescence to zero or near zero residual level by day light exposure. If

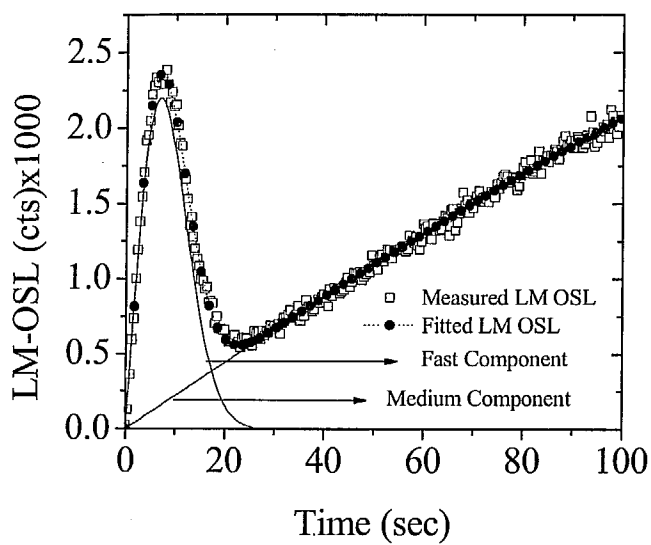


Figure 1.6 LM-OSL of the quartz in UV emission where the Blue light photons flux was ramped linearly during stimulation.

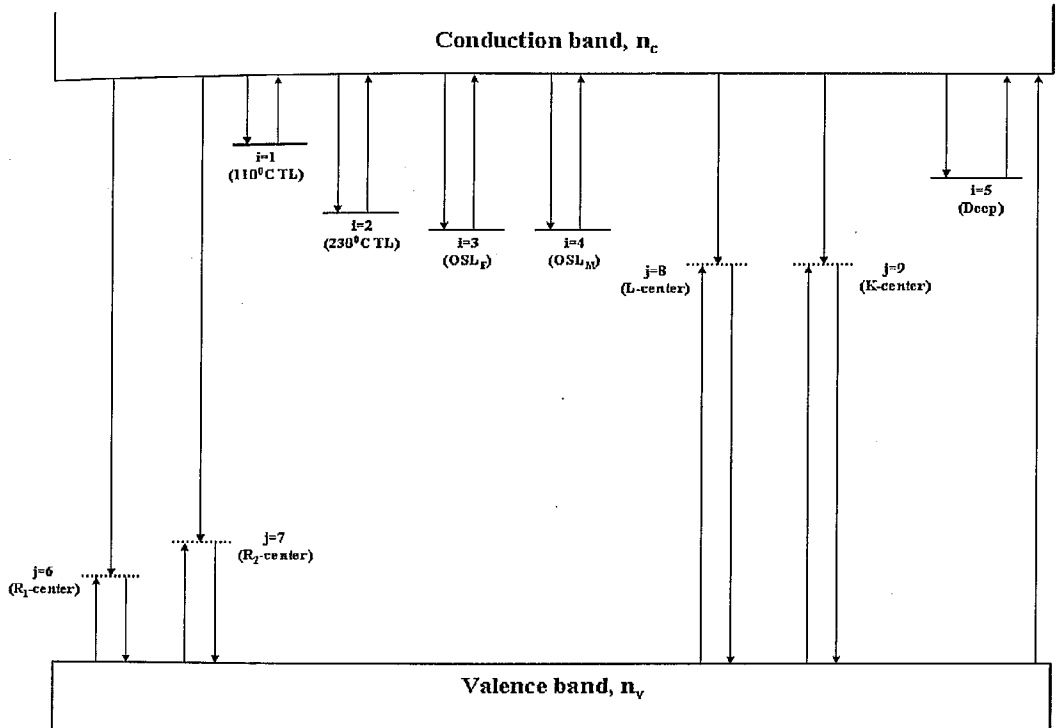


Figure 1.7 Empirical model of quartz in UV emission band (after Bailey 2001) with 5 trapping centers and 4 recombination centers.

the residual level is different for different grains i.e., heterogeneous bleaching, then a spread in the palaeodose distribution would occur. Presently much of the effort is concentrated towards understanding and dealing with the bleaching heterogeneity. One of the different ways to tackle the bleaching heterogeneity problem is to make luminescence measurements using smaller aliquots and as an extreme limit, use single grain and then use ages corresponding to the most bleached grains. However even in well bleached sediments where all grains should have been well bleached to their residual value, a spread in palaeodose was observed. Based on the present thesis, this is attributed to heterogeneity in the beta radiation dose seen by the grain. This thesis thus examines the heterogeneity of radiation dose rate and develops a possible *modus operandi* for the analysis of such samples. The dose rate heterogeneity becomes important at single grain level, where so far, only a constant average dose and dose rate are used. We demonstrate that dose rate heterogeneity occurs due to beta dose arising from ^{40}K in feldspar. This provides a major fraction of beta dose. We argue that individual grains receive different dose rates and hence the usage of mean dose rate is erroneous. This microdosimetry problem is examined in detail and a new age equation is developed.

1.6.1 Bleaching heterogeneity

Optical dating has been widely used to date aeolian sediments, for example desert dunes, wind transported dust and coastal dunes (Singhvi et al., 1982; Singhvi and Wintle, 1999; Murray and Olley, 2002). These sediments have prolonged exposure to clear daylight during transport and consequently their geological OSL signals are fully zeroed at the time of sediment deposition. However for fluvially transported sediments, the OSL zeroing may not be complete due to sub-aqueous sediment transport (Rhodes and Pownall, 1994; Murray et al., 1995; Olley et al., 1998). The daylight flux (both in respect of the spectrum and intensity) is attenuated due to transport specific parameters such as water depth, sediment load, turbidity, turbulence, light spectrum, grain size and distance of transportation. In many situations, the probability of complete zeroing of all sediment grains is low. Fig 1.8 gives the solar spectrum with the sun 60° below zenith. From the Fig. 1.9 only a very minimal proportion of intensity of 520 nm – 600 nm photons traverse through 7m water column.

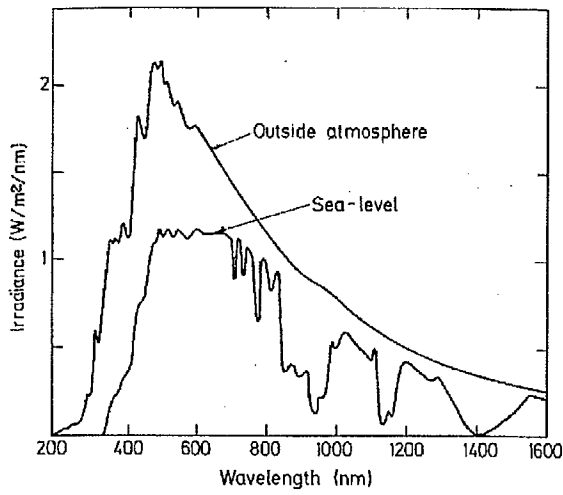


Figure 1.8 Solar Spectrum: outside the atmosphere and at sea level with the sun 60° below zenith (Oriel Solar Simulator handbook, based on works by M.P. Thekaekara; taken from Aitken, 1998).

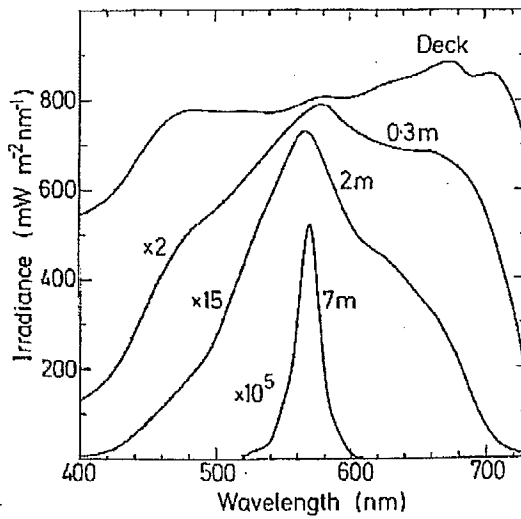


Figure 1.9 Solar spectra at various depths of water column (after Berger 1990). The sedimentation concentration was in the range 15-21 mg.l⁻¹ (taken from Aitken, 1998).

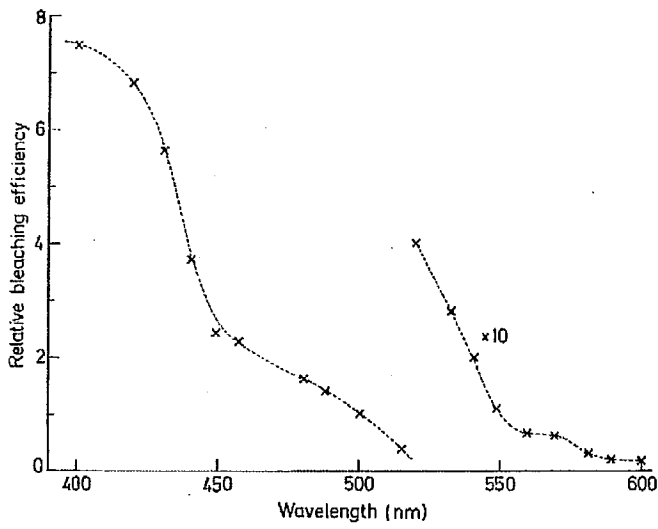


Figure 1.10. Bleaching efficiency versus wavelength (after Spooner 1994) of quartz (taken from Aitken, 1998).

This region of the daylight spectrum is several times less efficient in bleaching the natural luminescence in quartz compared to 400-450 nm photons (Fig. 1.10). Palaeodoses are measured using samples containing a small number of grains (or single grain) a distribution of values is seen and the average usually provides an age overestimate. Jain, et al., 2004a summarize various approaches for testing the completeness of bleaching. These are,

1. Direct measurements of the bleaching rates a function of turbidity, water depth or transport distance and deduction of an appropriate analysis protocol that probes only the most bleachable signal (Ditlefsen, 1992; Berger, 1990; Berger and Luternauer, 1987; Rendell et al., 1994; Rhodes and Pownall, 1994; Gemmell, 1997).
2. Dating of known age samples (Murray and Olley, 2002). It is reasonable to assume that the sample was sufficiently well bleached if the OSL age estimates are in agreement with the independent ages. However, such a test may not be appropriate if the sample of interest is much younger than the sample with the verified OSL age. Small age offsets are concealed by the uncertainties in the age measurements in older samples but nevertheless can be significant in younger material.
3. Age determination in modern samples (Stokes et al., 2001; Colls et al., 2001, Jain et al. 2003a). Although important for dating young samples, this approach may not be very relevant to studies extending back to the older samples, because present day transport conditions may not have been applicable in the past. Nevertheless, this provides the best bet.
4. Comparisons of ages based on different mineral fraction with different bleaching rates and seek a concordance of ages to ensure a total predepositional bleaching.

The above procedures help identify the existence of partial bleaching. However they do not offer a solution to remedy the problem after it is identified. The following are the suggestions after a heterogeneous bleaching is established. There are two categories of approaches namely, i) analysis of dose distribution and ii) analysis of OSL signal. These are described briefly in the following.

1.6.1.1 Analysis of dose distribution

If all the grains had the same bleaching history a relatively narrow dose distribution should be observed from a statistically significant number of D_e estimates. In cases where individual grains have been photobleached to different levels at the time of deposition, then a variation in D_e at both the aliquot and single grain level is seen, leading to an asymmetric distribution of D_e 's. A plot of D_e 's against natural OSL intensity, makes it possible to assess the bleaching heterogeneity of a sample (Li and Wintle, 1992, Clarke, 1996). In a well-bleached sample, although the natural intensities may be variable, the D_e estimates should be the same within errors. In contrast, poorly or heterogeneously bleached samples exhibit variability both in D_e and natural intensity due to remnant doses from previous depositional phases (Clarke, 1996). In situations where the single-aliquot data indicate a mixture of well-bleached and poorly bleached grains, it has been suggested that the realistic D_e would lie towards the lower D_e end (most-bleached) of the D_e distribution (Duller, 1996; Olley et al., 1998, 1999). According to Colls (1999), the standardised

$$t = r \sqrt{\frac{N-2}{1-r^2}}, \text{ (mean} = 0; \text{SD} = 1; \text{N} = \text{no. of aliquots, } r = \text{Pearson coefficient)}$$

plots of D_e versus signal intensity are examined to test for partial bleaching. Using the standardised plots it is possible to readily visualise the covariance within the dataset and test for the significance of any trend between D_e and the OSL intensity by examining the statistical significance of the resulting Pearson's correlation coefficient (r). The significance of the trend was estimated by establishing the correlation coefficient for each data set and generating a test statistic (t). Comparison of the value for this test statistic to a one-tailed Student's-t distribution (using $N-2$ degrees of freedom) allows the identification of statistically significant relationships. In this way the well bleached aliquots/grains is identified.

The following procedures are based on the fact that the dose distribution would be asymmetric if the grains do not have same dose rate and bleaching histories. Olley et al., (1999) assumed that the dose distribution in any sample is the result of two dose populations, one well bleached and another unbleached.

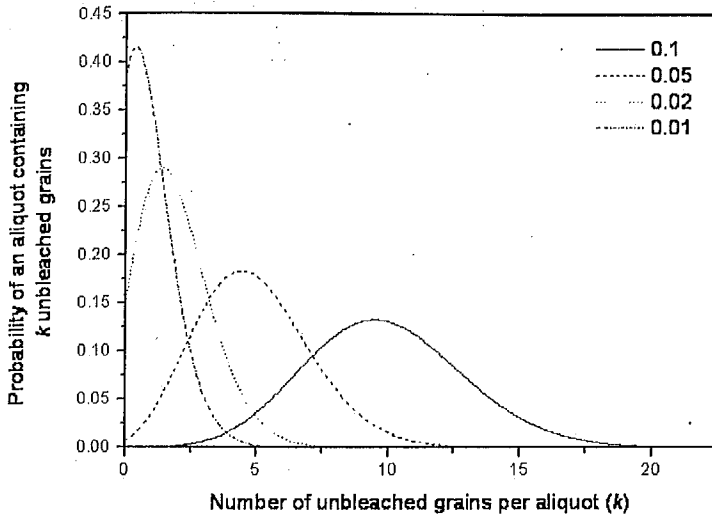


Figure 1.11a The probability distributions for $p=0.01, 0.02, 0.05$ and 0.1 . These are equivalent to the contamination of a well-bleached sample by 1 %, 2 %, 5 % and 10 % of unbleached grains, respectively (after Olley et al., 1999).

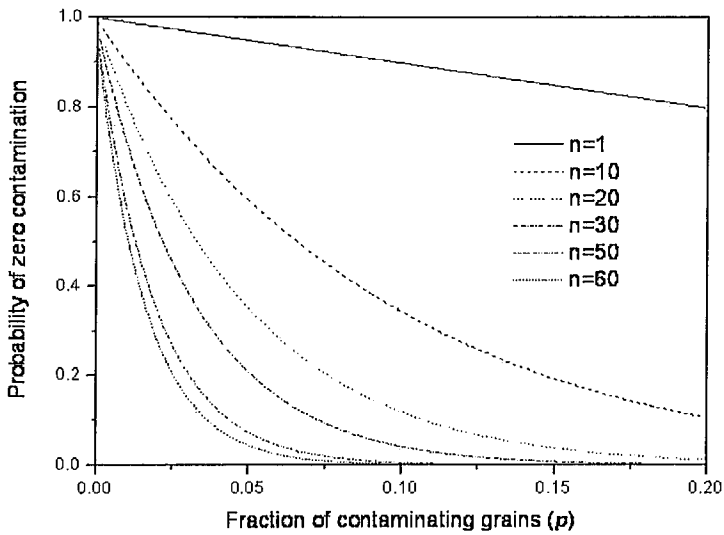


Figure 1.11b. The probability of selecting only well-bleached grains in aliquots consisting of n grains, versus the proportion of unbleached grains in a sample (after Olley et al., 1999).

The probability of selecting k unbleached grains are predicted by binomial distribution as follows,

$$E(n, k, p) = (nCk) p^k (1-p)^{n-k} \quad (1.19)$$

where p is the probability of selecting an unbleached grain, and n is the total number of grains selected. Fig. 1.11a shows the probability distributions for 1 %, 2%, 5 % and 10 % contamination of a well bleached sample by unbleached grains (after Olley et al., 1999). The distribution reaches an asymptotically symmetry with the increase of contamination by unbleached grains. The probability of selecting 60 grains that are all well bleached effectively decreases to zero when the proportion of unbleached grains rises above 5 % (Fig. 1.11b). This study, suggests that less number of grains in an aliquot and least value of D_e of an asymmetric dose distribution are to be considered for the age evaluation. This model was verified with quartz samples from fluvial deposits and an empirical suggestion was that the mean of the least 5 % of the dose points would provide an optimum result for partially bleached samples. The least x % is highly a subjective nature of D_e selection because the proportion of bleached grains in a sample depend on many factors and hence becomes sample dependent.

The following two procedures also deal with the selection of the most bleached dose distribution from the measured distribution in an objective manner. These methods reflect the same approach but provide a different way of getting the results. The precision and accuracy of the SAR procedures can be estimated from the results of the laboratory bleached and irradiated quartz grains by conducting a dose recovery test (DRT) wherein the sample grain is bleached in the laboratory, given a beta dose and then the same dose is recovered using the SAR protocol. As per Fuchs and Lang (2001), if the aliquots are less in number and for relatively lower doses (i.e., for sample with their paleodose in the linear part of the dose response curve) the following procedure can be used. The well bleached aliquots/grains are isolated using the following steps, viz. 1) the D_e values for each sample are ordered from lower to higher values; 2) starting with the two lower most D_e values, arithmetic mean D_e values are calculated with the number of values increasing by one in each step; 3) this procedure is repeated until a relative standard deviation of 4 % (the value derived from the dose recovery test) is exceeded. This mean value of all the aliquots till this point is then used for age calculation. Zhang et al. (2003) followed the same approach

but the 3rd step gave a different value. He used RSD of first regenerated (sensitivity corrected) points instead of RSD of DRT based on the assumption that the degree of bleaching of a sample can be assessed by comparing the difference in scatter between natural and the first regenerated OSL signals.

Lepper et al. (2000) attempted to get the true burial dose from the mixed dose distribution. He hypothesized that the measured dose distribution is the convolution of experimental error distribution and distribution due to natural sedimentary process and expressed this mathematically using Fredholm integral equation of first kind,

$$M(D') = \int g(D)f(D', D)dD \quad (1.20)$$

Where D is the true equivalent dose, D' is the calculated equivalent dose, $M(D')$ is the measured distribution, $g(D)$ is the distribution from sedimentary process, and $f(D', D)$ is the distribution from experimental error. Deconvolution of experimental error distribution from the measured distribution gives the natural sedimentary processes. In this manner, dose distribution is obtained without the experimental error. This has the information from both the well bleached and partially bleached grains.

Thomsen et al., (2003, 2006) followed statistical procedures to determine the mean dose in a well bleached dose distribution and to select the dose estimates belonging to the well-bleached part of an incompletely bleached dose distribution. The standard error α , on the weighted mean Z defined as,

$$Z = \frac{\sum_{i=1}^N D_i / \sigma_i^2}{\sum_{i=1}^N 1 / \sigma_i^2} \quad (1.21)$$

can be calculated in two ways :

$$\alpha_{ex}^2 = \frac{\sum_{i=1}^N (D_i - Z)^2 / \sigma_i^2}{(N-1) \sum_{i=1}^N 1 / \sigma_i^2} \quad \alpha_{in}^2 = \frac{1}{\sum_{i=1}^N 1 / \sigma_i^2} \quad (1.22)$$

where D_i are the individual dose estimates, σ_i are the individual estimates of uncertainty on the dose estimates D_i and N is the total number of measurements. The first estimate, α_{ex} , combines information on both the individual estimates of uncertainty (σ_i), and the deviation from the weighted mean ($x_i - Z$). In an ascending order of D_e values, cumulatively where the ratio of α_{in}/α_{ex} equal to 1, the mean of the

values prior to that are taken to provide the true burial dose. This is an objective procedure to select the true burial dose, if the dose distribution arises only from bleaching heterogeneity.

1.6.1.2 Analysis of OSL signal

Singhvi and Lang (1998) discussed the differences in the various components of the OSL decay curve and if a sample had bleached completely, then the D_e obtained by using various parts of the OSL signal would give the same value. Otherwise, the D_e 's will increase with the shining time giving a non flat shine plateau. They proposed a partial bleach method that worked well for the fluvial samples. However this was pre single aliquot times. For single aliquots, the same approach was used by Bailey (2003a) in this $D_e(t)$ -plot. Bailey distinguished the partial bleaching using replacement plots where the D_e 's obtained by using natural OSL signal and laboratory derived OSL signal (after bleaching in laboratory completely) are plotted against the shining time (Fig. 1.12). The name replacement comes because the natural signal is replaced by one of the regeneration dose points. After plotting both the normalized values of D_e 's obtained by using natural OSL and laboratory obtained OSL versus the shine time, the naturally derived D_e values will be flat and merge with laboratory derived D_e values if the sample is well bleached otherwise a rise of naturally derived D_e 's will be observed with the increasing of shining time.

Bailey (2003b) proposed a D_e versus Z -plots where the Z is the 'Total integral' D_e divided by the 'Initial integral' D_e . If the sample is well bleached, all the D_e values fall in $Z=1$ and form a cluster otherwise the points will have a large scatter. As the quartz OSL signal comprises at least 3 components conventionally known as fast, medium, slow components, the D_e obtained using fast component can be considered to be closed to true burial dose based on the reasonable premise that this should have been bleached within 2 seconds of sun exposure because the life time of the fast component is estimated to be in that range. In that case the stripping off components from the OSL signal is necessary (Bailey et al 1997). Deconvoluting individual exponential components from OSL signal is an ongoing research area (Istratov & Vyvenko, 1999; Madhav & Singhvi, 2006).

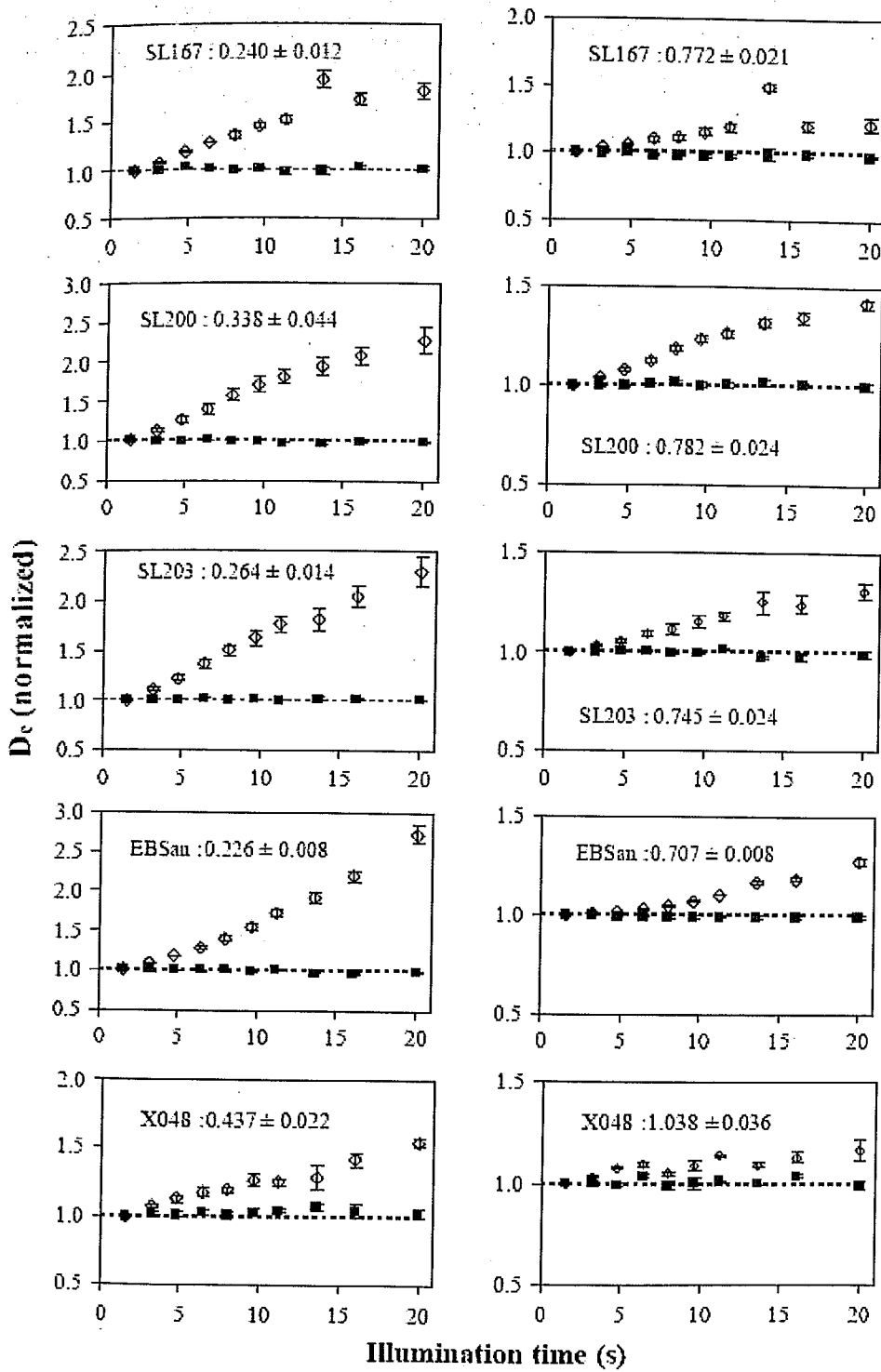


Figure 1.12. Checking partial bleaching in samples using the replacement plot (taken from Bailey, 2003a). Open circles are from the natural sample and the closed circles are from the laboratory bleached aliquots.

LM-OSL to an extent enable isolation of (Bulur, 1996) the different OSL components. LM-OSL signal also has been used as a diagnostic tool for partial bleaching (Agersnap Larsen et al., 2000) and to get the dose corresponding to most bleached grain (Yoshida et al., 2003).

Bailey and Arnold (2006) simulated the luminescence dating process numerically. In this simulation the growth of luminescence signal was simulated using Bailey's model. Various processes ranging from bleaching in parent rock during transportation, bleaching, dose accumulation during burial, measurement, analysis was simulated and the burial dose was estimated using all procedures described above. Being a luminescence processes simulation only bleaching heterogeneity was considered. The D_e 's from young aeolian, fluvial, medium fluvial and old fluvial were simulated and analyzed. The results indicated,

1. In most cases, significantly different estimate of the burial dose are obtained from each of the available age models,
2. In some cases, none of the age models correctly estimated the burial dose and no single age model was appropriate for all cases/samples,
3. It is not possible to choose the most appropriate age model using a single descriptor of the D_e distribution (such as the degree of over-dispersion).

An overall picture on how, on the basis of some observables, D_e can be analyzed using the existing age models is given in Fig. 1.13.

From the forgoing discussion, of the published literature, there is as yet no universally applicable method that adequately address to bleaching heterogeneity, is available. This is a challenge to the luminescence dating community.

1.6.2 Beta dose heterogeneity

Developments in the automated TL/OSL readers (Bøtter-Jensen et. al., 2000) and in photonics have made it possible to measure luminescence from single quartz grain of ~200 μm . The single grain study is most suitable for partially bleached samples as this enables well bleached grains to be isolated. However associated complexities with microdosimetry from using single grains have not been examined in requisite detail. The first report was by Murray & Roberts (1997), who measured the dose from a well bleached single quartz grains from Allen's cave deposits of southern Australia.

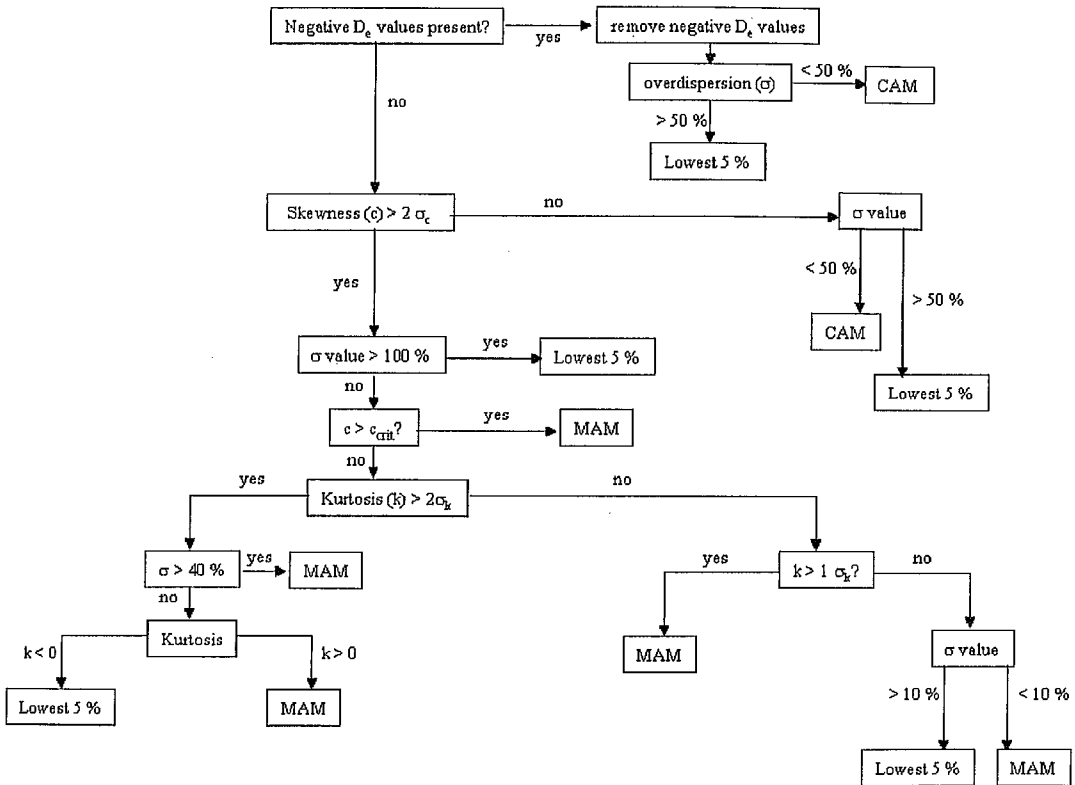


Figure 1.13. The flow diagram of optimizing the usage of method for dose distribution based on some statistical parameters (after Bailey and Arnold, 2006). CAM and MAM are Central Age Model and Minimum Age Model respectively. The critical values for skewness and kurtosis are the result of the simulation results. For more details see Bailey and Arnold, 2006.

The distribution of palaeodose (Fig. 1.14), from multi grain aliquots and single grain using the protocols for additive and regenerative dose, was bimodal with one peak at ~23 Gy containing ~83 % of the population, and the second at ~34 Gy with ~17 % of the population. The mean of the dose distribution was 22.7 Gy with the standard deviation of about ± 50 % of the mean value. Various possible causes of such large spread in the dose distribution were examined including the remobilization of buried sediment. Remobilization could not be the cause for this bimodality, because it would be impossible to move the sample by 2 feet to obtain the high dose (34 Gy) population. The anomalous fading was checked and no evidence of fading after 70 days of storage at room temperature was found. Thermal transfer was checked and this too was ruled out as the thermal transfer charges contribution would be less than 1 % for the preheat used and the consistency of this mean age with C-14 also helped to rule out this possibility. Then, based on the premise that each grain has its own dose response curve, growth curve of individual grains were checked. The growth curves from some selected grains indicated that they were all not linear and varied from sublinear to supralinear. This could have caused the high spread in additive dose procedure but not in regenerative procedure. Thus, all of the luminescence properties of the crystal such as anomalous fading, thermal transfer, dose response curves could not explain the dispersion of doses. Next the dosimetry was checked. The measured values of internal dosimetry and water content are 1.2 % and 5 % respectively. Even by reducing them to 0 %, the large spread could not be explained and the situation remained so till the present work which attributed to variation of the external variations in radioactivity over distances of a few millimeters a factor that has important implication.

On the same problem Olley (1997) tried to explain this large spread in terms of the spatial dose rate variations due to the presence of carbonate nodules among the aeolian sand grains. The carbonate fraction delivers a gamma and beta dose rate of about 0.25 Gy/ka whereas the dose rate from the Aeolian fraction is ~4 Gy/ka. All grains received 0.8 Gy/ka of gamma dose rate but differ in beta dose rate depending on the surrounding material. If the surrounding material is carbonate then the total dose rate is 0.94 Gy/ka and 3.4 Gy/ka if they are carbonate free sediments. If the mean dose rate of the sediments is used to calculate the ages of individual grains, then the grain surrounded by aeolian sediment will be ~70% older, and the grain

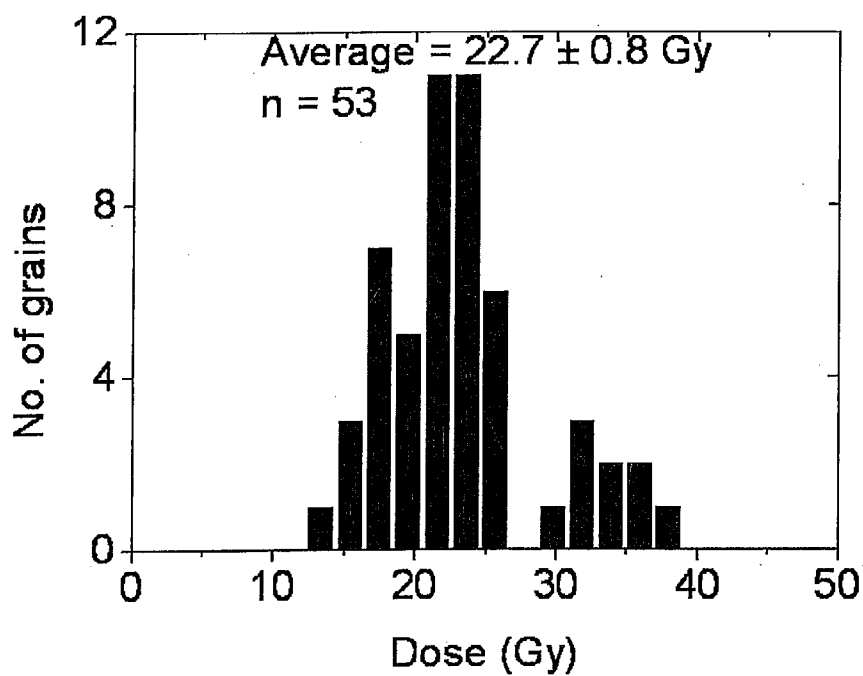


Figure 1.14. Single quartz grains dose distribution from Allen's cave deposits from southern Australia (after Murray and Roberts, 1997). First ever observed bimodal dose distribution.

surrounded by carbonate 60 % younger which is almost equal to ± 50 % standard deviation in their dose distribution and hence the above calculations indicate that this spread could be accounted for by the heterogeneity in the beta dose distribution alone, although the non-linear growth curves of some grains may augment the spread of the measured additive dose distribution.

After attributing the heterogeneity in the beta dosimetry to the large spread in the single grain dose distribution, Nathan et al. (2003) examined of potential problems in heterogeneous radiation environments and identify the likely magnitude of these effects on D_e distribution. He used the simulation toolkit MCNP-4C Monte Carlo electron/photon transport code and experimentally verified the observations. The simulations were done for three cases.

In the first case (A), 4 boxes of 8 mm cube was filled with 7.09 ppm U ore and $Al_2O_3:C$ of 100 μm size sparsely distributed. Each box had additionally either mm size steel balls or glass balls or plastic balls or no balls. After storing for sometime the dose distribution of $Al_2O_3:C$ grains from each box were measured and the same sets were simulated using MCNP code also. The experimental results show that there was no distinctive trend seen except some increase (24–25 %) in RSD in the dose distribution from plastic balls to steel balls. This same trend was seen in numerical simulations also. In the second case (B), the balls were replaced by non-radioactive calcium carbonate of different sizes (1, 4 and 10 mm) sparsely distributed. The distribution for 10 mm spherical diameters shows a greater probability of receiving low dose rates than that for 1 mm diameter. In the third case (C), the non-radioactive particles were replaced by highly radioactive granite particles, so that the effects could be seen due to the presence of heterogeneous distribution of radioactive sources. The dose distribution is different than Gaussian with significant skewness and characterized by absorbed doses in grains several times higher than the mean dose.

The conclusions were,

- Smaller heterogeneities are expected to give results closely approximated by the simple infinite matrix calculation with a low degree of asymmetry,
- The size of the media particles matter most as attenuates the actual dose rate than the estimated infinite matrix dose rate,

- The attempt to model a wide range of potential scenarios in order to reproduce the bimodality in the first ever published literature (Murray & Roberts, 1997) on single grain dose distribution was not successful and all the simulated distribution were unimodal.
- So far only 3 publications exist, where some attempts to address to the beta heterogeneity problem, exist.

From the above literature survey, the candidate found that the beta heterogeneity and the bleaching heterogeneity are the two problems to be tackled adequately particularly when the single grain ages are to be interpreted. These two problems are complex in nature. The efforts so far by using the well established statistical methods and/or the available computing facilities for simulation.

Chapter 2

Experimental details and Methodology

2.1 Experimental Details

In this chapter, the experimental details along with the methodology of measuring the equivalent dose of the sample are presented. The analysis procedures for the computation of the equivalent dose for the age estimation are also discussed.

A TL-OSL reader comprises a stimulation source, a photon detection and counting system, a beta irradiator, a readout and system control unit (Fig. 2.1). A standard PC provides for system controls and real time data acquisition plus display. In the present study a RISØ-TL-OSL TL-DA-12 and a single grain reader TL-DA-15 were used.

2.1.1 Stimulation

In case of quartz the stimulation wavelength is $\sim 470 \pm 20$ nm (Bøtter-Jensen et al., 2003a). For this, an array of blue LEDs is used, and the illumination power is controlled electronically. An optical feedback servo-system ensures the stability of the

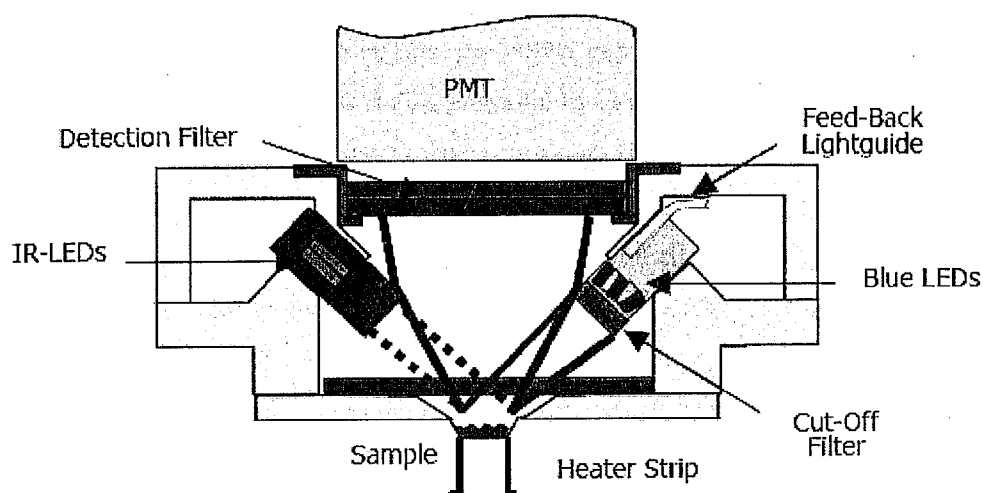


Figure 2.1 Stimulation and detection unit (taken from Internal Report, Risø National Laboratory, Denmark). IR-LEDs and Blue LEDs are used for optical stimulation and linear rate heating for thermal stimulation. Standard bi-alkali photomultiplier tube EMI 9235QA is the photon detection unit.

stimulation power. The LEDs are arranged in 4 clusters each containing seven of them. The distance between sample and stimulation source is ~20 mm. The total power delivered by the blue stimulation source to the sample from these 28 LEDs can go upto 40 mW/cm² (Bøtter-Jensen et al., 2003a). A green long pass filter (Schott GG-420) is incorporated in front of each blue LED cluster to minimize the amount of directly scattered blue light reaching the detector system (Bøtter-Jensen et al., 1999).

For feldspars, IR stimulation is used. As this present study focused on quartz, IR stimulation was used only to check for feldspar contamination from the processed quartz (Duller & Bøtter-Jensen, 1993). In the Risø system, IR LEDs are arranged in 3 clusters of seven LEDs with a emission wavelength centered at 875 nm. The maximum power delivered to the sample from the 21 IR LEDs is 135 mW/cm².

In both these stimulation wavelengths, the power supplied can be ramped linearly so that a Linearly Modulated-OSL is also possible. In Continuous Wave OSL (CW-OSL) the stimulation source intensity is kept constant and OSL decay is obtained. In Linearly Modulated OSL, the stimulation source intensity is linearly increased from zero to a maximum. For Thermoluminescence (TL), the stimulation source is heat and provided by a ramped temperature profile providing typically 1°C/s – 10°C/s. During an OSL measurement, it is required that sample temperature should be held constant (Spooner, 1994) for reproducible results. This calls for a good electronic control of temperature in a highly reproducible manner and an optimal thermal contact between the heating medium and the detector. In Risø readers the heating strip is made of Kanthal (a high resistance alloy). The temperature control is by a feedback circuit which compares the difference between the linear ramp and the thermocouple output and the difference controls the power to the heater strip. The thermocouple used in the reader is an Alumel-Cromel alloy and is mounted underneath the heater strip. The precession of temperature control is $\pm 4^{\circ}\text{C}$, and the error in reproducibility of heating rate is <1%. All measurements of TL/OSL were done in an ultra pure Nitrogen (Grade IOLAR-I) gas atmosphere which protects the heating system from oxidation at high temperature and serves as a medium for heat conduction from the heater plate to the grains and quenches spurious non radiative luminescence.

2.1.2 Detection unit

The color of the light emitted by quartz can range over the entire visible electromagnetic spectrum extending both to UV and near infra red regions (Fig 2.2).

To avoid any interference of stimulation light, extensive use of band pass and edge cut filters is made. The photon detection system comprises a standard bi-alkali photo multiplier tube EMI 9235QA having a maximum detection efficiency at around 400 nm. The distance between the photocathode and the sample is 55 mm, giving a detection solid angle of approximately 0.4 steradians (Bøtter-Jensen et al., 2003b). The emission wavelength of luminescence signal from quartz most suitable for the dating of sediments is in the UV range and 7.5 mm Hoya U-340 filter was used. This provides a detection window from 280 nm to 370 nm.

2.1.3 Stimulation of single grains

The luminescence from single grains is achieved by stimulating grains kept in specially designed sample holder. They are rhodium plated aluminium discs containing 100 holes, 300 μm deep by 300 μm in diameter, arranged in the form of a 10 by 10 grid with 600 μm spacing between hole centers. Irradiation and heating are thus performed simultaneously on all 100 grains whereas the OSL signal can be measured separately from individual grains by using a focused laser beam. The standard stimulation source in single grain attachment is a 10 mW Nd:YVO₄ solid state diode pumped laser emitting at 532 nm focused at a spot < 20 μm in diameter. The maximum energy fluence rate at the sample is approximately 50 W/cm². The laser spot is steered by two orthogonal mirrors attached to two programmed high precision motors. This set up is schematically given in Fig. 2.3.

2.1.4 Irradiation

The irradiator houses a 40 mCi activity ⁹⁰Sr/⁹⁰Y beta source (Fig. 2.4). The maximum energy of the beta particles is 2.27 MeV. An important aspect of beta irradiation is the spatial heterogeneity of dose delivered by the beta source. The dose homogeneity was tested by Jaiswal (2005), who computed dose to grain in different rings of single grain discs. In the Risø system supplied variability of dose to grains across a disc was <10%.

All the above units of stimulation, detection and irradiation were linked via Minisystem to a standard PC facilitated both the system control and a real time data acquisition (Bøtter-Jensen, 1997).

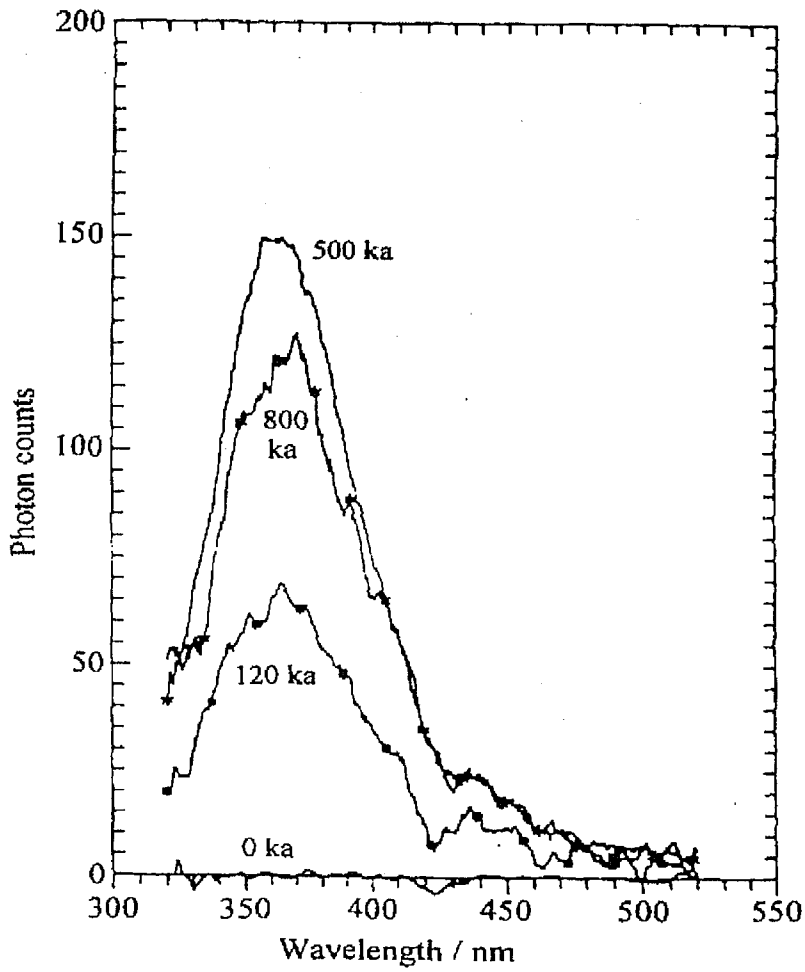


Figure 2.2 Emission band of a typical quartz after optical stimulation at the wavelength of 614 nm (after Huntley et al., 1991).

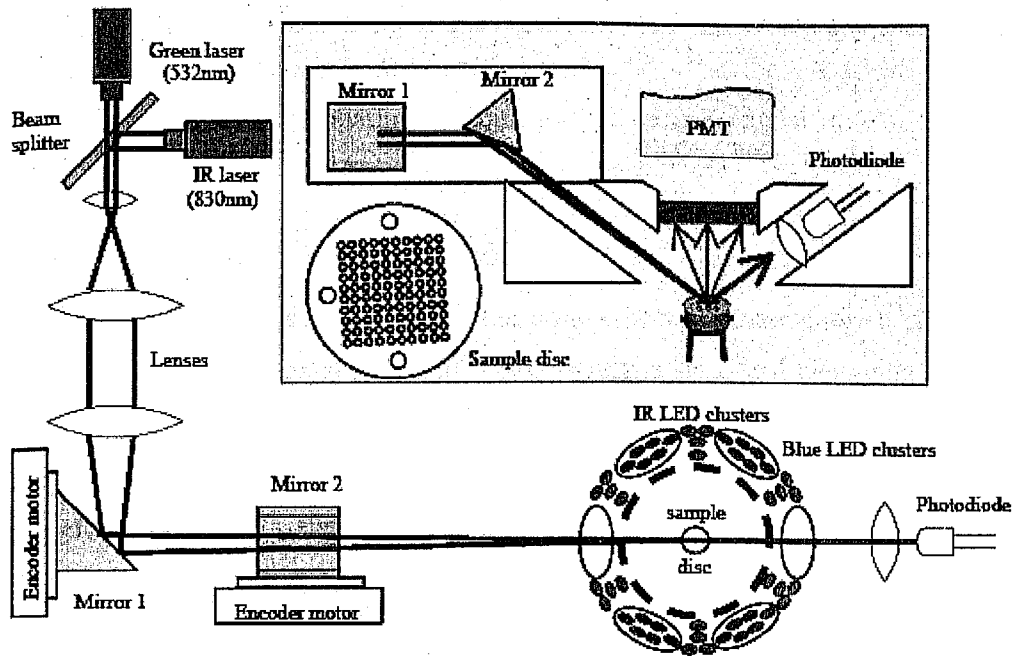


Figure 2.3. Schematic diagram of Risø Single Grain OSL reader (taken from Internal Report, Risø National Laboratory, Denmark).

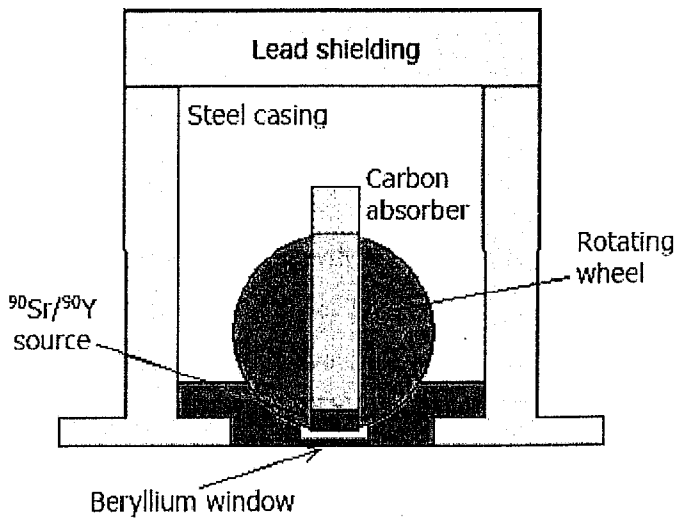


Figure 2.4 Irradiation unit (taken from Internal Report, Risø National Laboratory, Denmark). 40 mCi activity $^{90}\text{Sr}/^{90}\text{Y}$ beta source is the irradiation unit.

2.2 Methodology

In this section, the protocols for age estimation are described. Basically an age computation comprises estimation of equivalent dose and annual dose (dose rate). Procedures for estimation of dose and dose rate are briefly discussed below.

2.2.1 Measurement of Equivalent Dose

The equivalent dose is estimated from the luminescence signal acquired during the burial time from the ambient radiation. Traditionally, a statistical averaging of signal using multiple identical aliquots of the same sample was used for the estimation of equivalent dose. With the advent of OSL, single grain measurements have emerged as the preferred method. A statistical rigor in the ages is achieved by analyzing a large number of single aliquots single grains. The single grain measurements provide the equivalent dose of every single grain that satisfies the analytical rigor. Two methods are being used to measure the equivalent dose from multiple aliquots and single aliquots/ single grain are

- a) multiple aliquot additive/ regenerative dose method
- b) single aliquot/ single grain method.

2.2.1.1 Multiple Aliquot – Additive Dose (MAAD)

In this case the sample after chemical processing and purification is divided into several “identical fraction” fractions, which are given incremental beta doses ranging from zero (natural, as received), β_1 to β_N . The luminescence yield when plotted against the applied dose provides the growth curve and this when extrapolated to zero luminescence provides the equivalent dose. This is explained in Fig. 2.5 and a typical measurement is also given. In the additive dose procedure, a dose response curve is constructed. Extrapolation to zero dose value assumes that the mathematical form of the growth curve is known and that any sub- or supra-linear behaviors can be accounted for. Recommendation on optimum measurement for minimum error in equivalent dose, was given by Felix and Singhvi (1997) who examined this aspect in some detail. In the present study MAAD ages were obtained in several samples.

2.2.1.2 Multiple Aliquot – Regenerative Dose

In this procedure, a replication of samples history is made. A regeneration growth curve is constructed by bleaching discs under a sunlamp/solar simulator and then

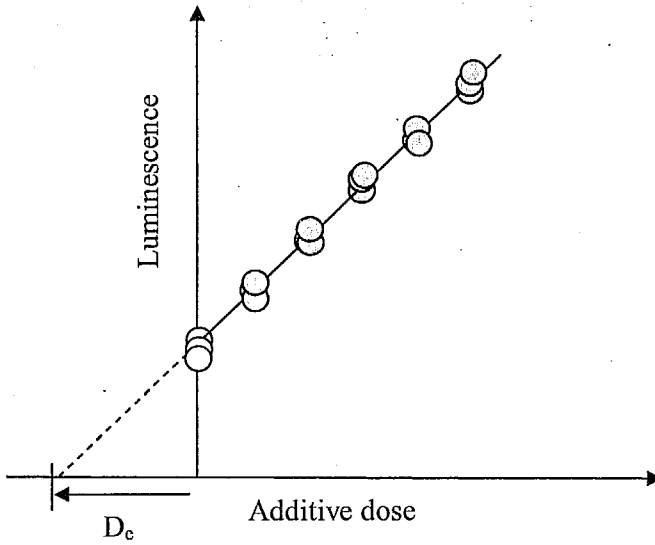


Figure 2.5(a). Schematic diagram explaining multiple aliquot additive dose method. The open circles are the naturally accrued luminescence points while the closed ones are the laboratory irradiated luminescence points. Each dose points are from 3-5 aliquots.

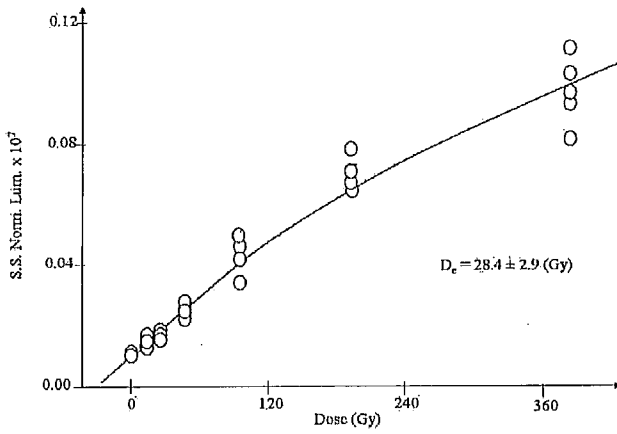


Figure 2.5(b). Actual measurement of multiple aliquot additive dose method of Wahiba sands from Oman. The 0.1s short shine normalization was done for all the aliquots.

sequentially irradiating them. The laboratory regenerated signals ($(N+Sun, N+Sun+\beta_1, \dots, N+Sun+\beta_N)$) are used to construct the dose response curve (Fig. 2.6) and the natural luminescence is read on this curve to get the equivalent dose.

A limitation of Multiple Aliquot method is that, it is analysis of an average behavior of a mixed population of grains such that any contamination by any undesirable grain (for example unbleached grain or an anomalously fading grain) is included. First of all, the main assumption in the multiple aliquot procedure is that all the fractions of the sample is identical in terms of its thermal, bleaching and radiation history. To ensure that all aliquots have an identical weight in regeneration growth curve, normalization procedures are useful but these often have methodological and sample difficulties and dependent errors. Difficulties arise from difference in intrinsic natural sensitivity of grains (often only upto 10% of the grains provide 90% of the signal, Fig 2.7) differences in the dose response of individual grains provide other source of major variants. These differences are not easily accounted for, and depending upon individual situations, methods such as weight normalization, short shine normalization, dose normalization etc. are used these have been discussed in detail by Jain et al., 2003a.

2.2.1.3 Single Aliquot – Additive Dose

This method helps avoid the need for normalization and hence provides improved measurement precision. The additive dose method can be applied to single aliquot procedure also. In this procedure, the naturally acquired luminescence of individual aliquots is measured using a short duration (0.1 sec) stimulation without depleting the signal. The same aliquot is then irradiated and the luminescence yield is measured again using a short duration stimulation without depleting all the signal. This is repeated to construct a growth curve. Extrapolation of the dose response curve to the dose axis provides the equivalent dose. Any uncertainty about the response of sample in low dose can imply difficulty in a realistic extrapolation. This method is not suitable for thermoluminescence as the signal readout causes the total depletion of the signal.

2.2.1.4 Single Aliquot – Regenerative Dose (SAR)

Murray and Roberts (1997) and Murray and Wintle (2000) suggested the single aliquot regeneration procedure which presently is the most used protocol.

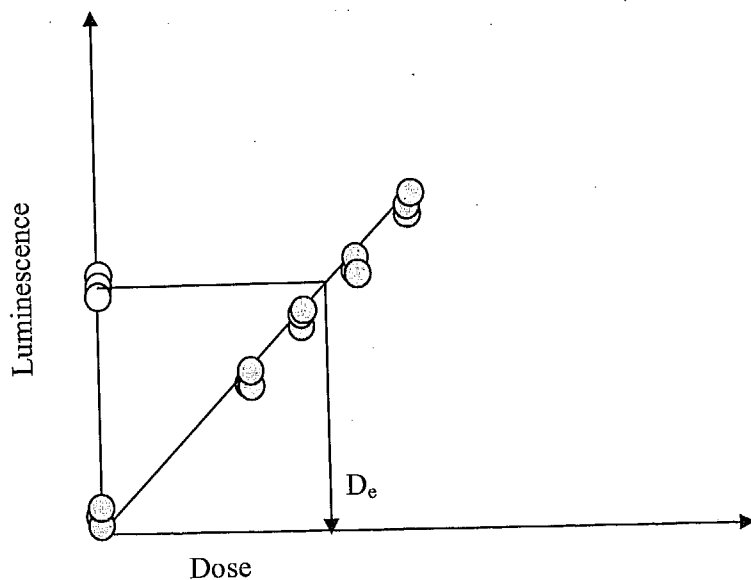


Figure 2.6 Schematic diagram explaining multiple aliquot regenerative dose procedure. The open circles are the naturally accrued luminescence points while the closed ones are the laboratory irradiated luminescence points. Each dose points are from 3-5 aliquots.

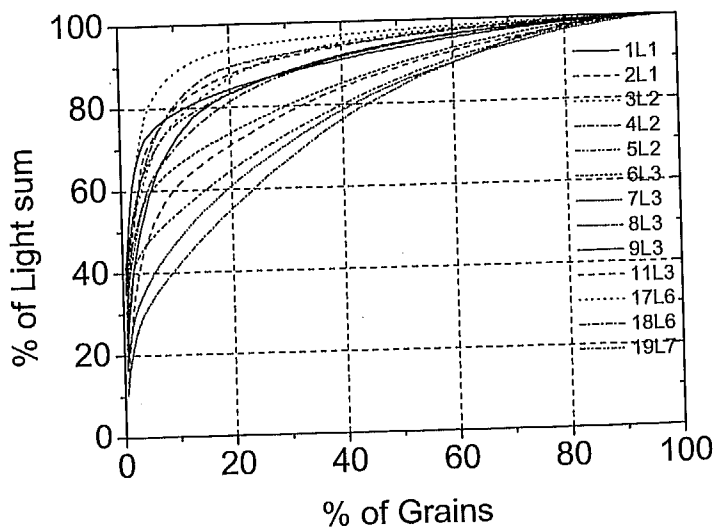


Figure 2.7 Proportion of bright grains in the sample. Normally 5 – 10 % of the grains are bright. This figure is for sand grains from Wahiba sands.

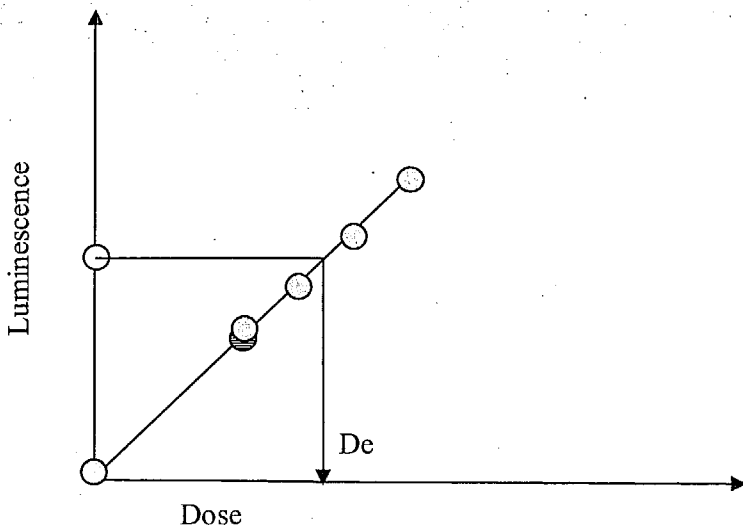


Figure 2.8(a) Schematic diagram explaining the single aliquot regenerative dose procedure (SAR; Murray and Wintle, 2000). Filled circles shows the laboratory irradiated luminescence points and the open circle is the luminescence due to natural ambient radiation environment. The shaded circle point is used to calculate the recycle ratio which is the ultimate measure of the sensitivity changes during the measurement procedure.

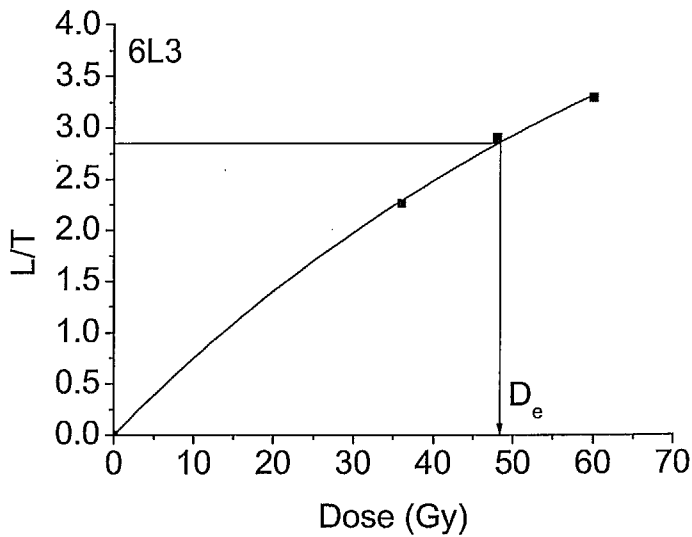


Figure 2.8(b) Estimation of D_e using SAR procedure for 6L3 (Wahiba snads from Oman). The growth curve is fitted to single saturating exponential function.

The possibility of sensitivity changes due to repeated thermal, optical and irradiative treatments on the same sample as part of the measurement schedule is circumvented by the inclusion of a correction factor based on a measurement of test dose luminescence which is administered after every regenerative dose (Fig 2.8).

In the single aliquot procedure approximately 50-60 grains are measured together, the aliquot to aliquot variability in luminescence characteristics like dose response, sensitization etc., can occur. Further more, it has been reported that the OSL decay curve is not a simple exponential but a multi exponential suggesting a multi-traps origin of the signal. So far upto seven components have been reported but generally the OSL decay can be explained by a set of three exponentials with the fastest component contributing to upto 60-70 % of the signal (Jain et al., 2003b; Singarayer and Bailey, 2003, Madhav et al., 2006). Presence of three components with their own growth curves implies the need for careful analysis.

2.2.1.5 Standard Growth Curve (SGC)

This method was followed in some of the samples analysed in the present thesis. The SGC-SAR protocol is aimed towards reduction of the measurement time of a sample. In the normal SAR, the natural sensitivity corrected (L_n/T_n) luminescence is measured and after getting the dose response curve, the L_n/T_n is interpolated into the dose response curve to get the equivalent dose. Normal SAR run for each sample includes, many cycles of irradiation, preheat and readout. Roberts and Duller, (2004) and Burbidge et al, (2006) suggest that instead of using individual dose response curves for the aliquots, in some situations, a common dose response curve can be used for the aliquots of the same sample. The common dose response curve is called SGC. Based on a detailed analysis we propose that the standard growth curve can be obtained from 5-10 aliquots and can be used as SGC if the R^2 of the fitting is greater than 0.9. This procedure was adapted in the analysis of some of the samples.

2.2.1.6 NCF-SAR

Stokes and Singhvi (personal communication) proposed that in the normal SAR procedure, while accounting for the sensitivity changes after the readout of natural OSL, the sensitivity changes that occur during the preheat and read out of the natural signal are not corrected. Stokes and Singhvi suggested that the use of 110°C TL peak to monitor such a sensitivity change. The sample as received is given a nominal beta

dose and its TL upto 160°C is readout. This provides a record of initial OSL sensitivity. The sample is then preheated and OSL measured. The sensitivity is then measured again for same nominal beta dose and a TL read out. The ratios of sensitivities after readout to the previous sensitivity, provides a correction factor for SAR ages. The protocol is given in Fig. 2.9. The use of the 110°C peak as a surrogate for the OSL signal is based on the observed correlation between the intensity of 110°C peak and OSL signal. Studies using NCF indicated improved results in equivalent doses in the dose distribution.

2.2.1.7 Experimental errors

The estimation of the experimental error associated with the data are described below. The source of random error is the photon counting statistics and instrumental uncertainty. These two sources combined together for total random error in palaeodose. The error due to counting statistics is quantified by the relation (Galbraith, 2002; Jacobs et al., 2006),

$$rse_{cs} = \frac{\sqrt{\sum_i S_i + \hat{B}_n / k}}{\sum_i S_i - \hat{B}_n} \times 100 \quad (2.1)$$

where rse_{cs} is the relative standard error due to counting statistics, S_i is the signal from the i^{th} channel integration, \hat{B}_n is the average background OSL signal from n number of channels and k is equal to m/n where m is the number of channels used for signal and n is that used for background.

The total experimental reproducibility is estimated as follows. For each aliquot/grain 10 repeated L_x measurements (L_1, L_2, \dots, L_{10}) are normalized relative to L_1 and plotted against the measurement cycle and a regression line is drawn (linear or quadratic). Ideally it should be linear. The error is computed (Jacobs et al., 2006) using

$$rse_{L_x} = \sqrt{\frac{\sum_{i=1}^n (y_i - \hat{y}_i)^2}{n-2}} \times 100 \quad (2.2)$$

where rse_{L_x} is the relative standard error due to the luminescence measurements, y is the normalized luminescence signal $\left(\frac{L_x}{T_x}\right)$ for a specific grain/aliquot, \hat{y}_i is the

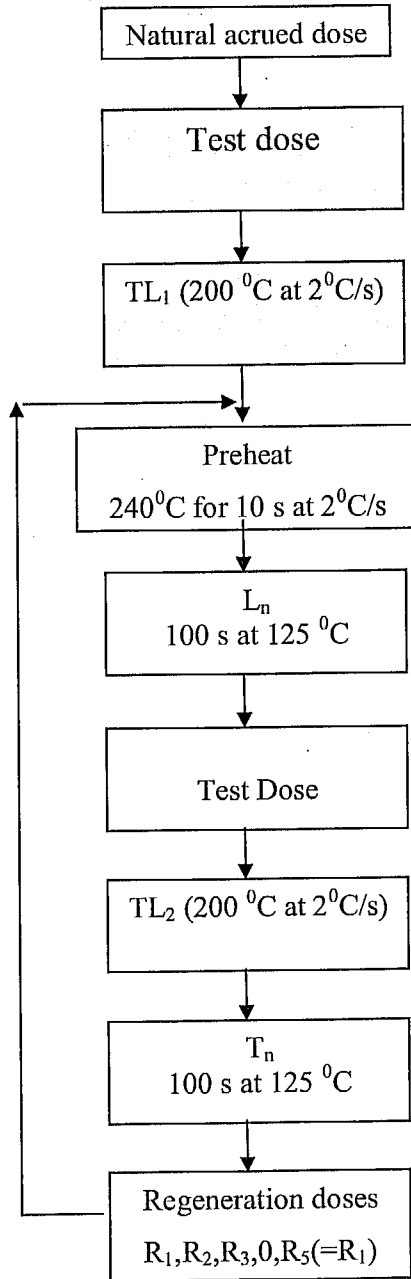


Figure 2.9 Sequence for NCF-SAR protocol. The shaded steps are the additional ones to the normal SAR sequence.

normalized value predicted from the trend line for that grain/aliquot, $\sum_{i=1}^n (y_i - \hat{y}_i)^2$ is the sum of the squares and $n-2$ is the corresponding degrees of freedom associated with the sum of the squares. This error is inclusive of counting statistics error. So, to estimate instrumental uncertainty, the counting statistics error should be subtracted from the experimental reproducibility i.e.

$$rse_{in} = \sqrt{(rse_{Lx}^2 - rse_{cs}^2)} \quad (2.3)$$

The estimated instrumental uncertainty value in the present case for single aliquot was 1.2 % and for the single grain using the above method is 3.5 %. This has been considered for all the measured dose points.

2.2.2 Measurement of Dose rate

The annual radiation dose can be estimated by knowing the elemental concentration of the natural radioactive elements viz ^{238}U , ^{232}Th and ^{40}K and the cosmic rays. The radioactivity and the concentration (in ppm) of U & Th are estimated using thick source, ZnS(Ag), alpha counting (TSAC) system (Aitken, 1985). The α count rate from a calibrated alpha counter can be converted into the ppm concentration using standard conversion relation (Aitken, 1985). Gamma ray spectrometry using NaI(Tl) was used to estimate the K by comparing the counts in 1.46 MeV photopeak of a sample with that from a calibrated KCl standard. From the U, Th and K concentration, the dose rates in Gy/ka was computed. This computed value is the average dose rate and so far it has been considered that all the grains received this dose rate during their burial.

2.2.3 Analysis

Analysing the values obtained from the multiple aliquot procedure provides a single equivalent dose based on measurements on 40+ aliquots. Single aliquot and single grain measurements provide a range of equivalent dose from which the true equivalent dose is extracted using a variety of statistical procedures. Most of the procedures for age calculation are presented in Section 1.6.1.1. Here a brief detail about the age models is given.

2.2.3.1 Common Age Model

In an ideal sample (in which all grains receive the same dose), the equivalent dose estimates would be consistent with a common value. Thus for e.g., for a grain i with estimated equivalent dose $\hat{\delta}_i$ and standard error S_i , the common age model will provide $\hat{\delta}_i = \delta + \varepsilon_i$, where δ is the true common equivalent dose and ε_i is the deviation of δ_i from δ . If this deviation is assumed to be a random quantity with mean (expected value) 0 and variance S_i^2 , then the estimate of the common equivalent dose δ will be the weighted average

$$\hat{\delta} = \frac{\sum_{i=1}^n w_i \hat{\delta}_i}{\sum_{i=1}^n w_i} \quad (2.4)$$

where $w_i = 1/S_i^2$. The standard error of this estimate is $(\sum w_i)^{-1/2}$. If the deviation ε_i are normally distributed, then $\hat{\delta}_i$ is the maximum likelihood estimation of δ (Galbraith et al., 1999).

2.2.3.2 The Central Age Model

Common age model is used sparingly; as it does not account for all the errors. A more generalized version is central age model, in which $\hat{\delta}_i = \delta_i + \varepsilon_i$, for $i=1, 2, \dots, n$ where δ_i is the true equivalent dose of grain i and ε_i is again a random quantity with mean 0 and variance S_i^2 . In this model, the true equivalent dose of individual aliquots/grains, δ_i , are not equal, but are a random sample from a normal distribution with mean δ and standard deviation σ . This means that all the grains have considerable spread in dose during the burial time which could be due to beta dose heterogeneity, and some dose prior to deposition (due to partial bleaching). This spread due to the both causes may be considered to be σ and the experimental error is ε which is normally distributed. The central age model thus has two unknown parameters, δ and σ . If $\sigma = 0$, then the central age model reduces to the common age model. However it may be more appropriate to assume that $\sigma > 0$.

If ε_i is normally distributed, it follows that $\hat{\delta}_i$ is normally distributed with mean δ and σ , which can be estimated by standard maximum likelihood methods, and the

standard errors can be estimated by inverting the observed information matrix. It can be shown that the maximum likelihood estimates, denoted by $\hat{\delta}$ and $\hat{\sigma}$, are the values of δ and σ satisfying the equations.

$$\hat{\delta} = \frac{\sum_{i=1}^n w_i \hat{\delta}_i}{\sum_{i=1}^n w_i} \quad (2.5)$$

and

$$\sum_{i=1}^n w_i^2 \left(\delta - \hat{\delta} \right)^2 = \sum_{i=1}^n w_i \quad (2.6)$$

where $w_i = 1/(\sigma^2 + s_i^2)$. The Eq. (2.5) is a weighted average similar to equation 3 but with different weights w_i . Eq. (2.5) and Eq. (2.6) can be solved numerically to obtain $\hat{\delta}$ and $\hat{\sigma}$. A simple method is to choose a range of plausible values of σ , and for each σ calculate w_1, w_2, \dots, w_n , and the δ from Eqn.2.5 and thence $\sum w_i^2 \left(\delta - \hat{\delta} \right)^2 - \sum w_i$. Then $\hat{\sigma}$ is the value of σ for which $\sum w_i^2 \left(\delta - \hat{\delta} \right)^2 - \sum w_i$ is zero. This can be found by interpolation, then $\hat{\delta}$ can be found by using $\hat{\sigma}$ in equation 2.5 (Galbraith et al., 1999).

2.2.3.3 Minimum Age Model

Although it is convenient and simple, the central age model may not always be appropriate. Furthermore, it has no explicit physical justification except in the general sense that unknown effects may induce random deviations from the common age model.

A more explicit generalization is one in which some quartz grains are taken as fully bleached prior to deposition and burial, whereas others as partially bleached, yielding larger equivalent dose and optical ages. To model this in a plausible way, we start with equation 2.4 but now the true equivalent dose δ_i is a random sample from a completely bleached portion before burial. Each of these grains acquires the minimum equivalent dose, denoted by γ . Partially bleached grains have a larger equivalent dose, drawn from a truncated normal distribution with parameters μ and σ . The lower truncation point is γ , which is the same equivalent dose as that acquired by the fully

bleached grains. If the distribution is not truncated, it would have mean μ and σ that are no longer the mean and standard deviation, it is however convenient to retain them as the parameters; they are simply adjustable parameters that take the unknown spread in the log equivalent dose of the partially bleached grains.

From equation 2.4 it can then be shown that the probability density function of an observed equivalent dose $\hat{\delta}$ is $f_i(z)$, given by

$$f_i(z) = \frac{p}{\sqrt{2\pi s_i^2}} \exp\left\{-\frac{(z-\gamma)^2}{2s_i^2}\right\} + \frac{1-p}{\sqrt{2\pi(\sigma^2 + s_i^2)}} \frac{1-\Phi\left(\frac{\gamma-\mu_0}{\sigma_0}\right)}{1-\Phi\left(\frac{\gamma-\mu}{\sigma}\right)} \exp\left\{-\frac{(z-\mu)^2}{2(\sigma^2 + s_i^2)}\right\} \quad (2.7)$$

Where $\mu_0 = \frac{\mu/\sigma^2 + z/s_i^2}{1/\sigma^2 + 1/s_i^2}$, $\sigma_0 = \frac{1}{1/\sigma^2 + 1/s_i^2}$ and where $\Phi(z)$ is the cumulative

distribution function of the standard normal distribution. The Eq. (7) tells that p proportion of grains have the mean dose of γ with the standard deviation of S_i and considered to be well bleached grains. The rest $(1-p)$ is partially bleached. Here the assumption is that the dose distribution of all the grains is normal distribution. The maximum likelihood estimates of p , γ , μ , and σ are those values for which the log likelihood L is a maximum, where $L = \sum_{i=1}^n \ln f_i(\hat{\delta}_i)$. There are now no simple

equations for \hat{p} , $\hat{\gamma}$, $\hat{\mu}$, and $\hat{\sigma}$, so these and their standard errors are most easily computed numerically by using an optimization program (Galbraith et al., 1999).

2.2.3.4 Finite Mixture Model

This model is based on assumption that the measured dose distribution will be comprise more than one normal distribution, depend upon the population of grains with varying dose (Galbraith and Green, 1989). The obtained dose distribution is statistically fitted to a superposition of many Gaussian functions and the fraction of grains contributing to a dose value is computed from those functions the true burial

dose was calculated. Following the analysis of Van der Tauw et al. (1997), the suitability of age model fitting can be assessed using two statistical tests:

The 'Bayes Information Criterion' (BIC; Schwartz, 1978), calculated as $BIC = -2L_{max} + p \log(n)$ where L_{max} is the maximum log likelihood value for a particular combination of Gaussian functions, p the number of free parameters in the combination, and n is the sample size (number of D_e values).

The log-likelihood ratio test, in which a critical value is computed as $2 \times \Delta_{LL}$ (where Δ_{LL} = difference in maximum log-likelihood estimates between two competing combination Gaussian functions) and then compared to the χ^2 distribution.

For the BIC tests it is the model yielding the lowest BIC value that is viewed as using the optimal number of parameters.

Both the minimum age model and the finite mixture model are mainly focused on the lowest dose population because the well bleached grains are thought of having relatively low dose compared to the partially bleached grains. This is also because the burial dose is considered to be same for all the grains. But if the sample suffers by beta dose heterogeneity then the above point would be invalid (i.e., lowest dose wouldn't be the true representative of burial dose).

In the present thesis, the equivalent dose was obtained using all the above mentioned models but the reported values are from the arithmetic mean value and the common age model value only.

Chapter 3

Chronology of Aeolian sequences

3.1 Introduction

This chapter presents experimental results on wind transported desert sand samples. Three sequences of aeolian deposits from different region of the world were collected for a detailed study. The choice of these samples was dictated by the need of obtaining well bleached natural samples to determine their palaeodose distribution if there were additional causes of dispersion of equivalent doses. The main focus was to establish the effect of beta dose heterogeneity, and to develop a protocol for estimation of age if the beta dose heterogeneity did result in a dispersion in equivalent doses. The first step was to examine if the effects of partial bleaching and beta dose heterogeneity could be decoupled.

3.2 Wahiba Sands

3.2.1 Sample Description

Wahiba dunes were formed by the winds associated with southwest Monsoon and the Shamal winds (Singhvi & Kar, 2004, Glennie & Singhvi, 2002). This chapter describes only the luminescence dating aspects. The geological importance of this study will be discussed elsewhere.

3.2.2 Experimental details

A) Sample Preparation

The samples were collected in specially designed metal tubes (Chandel et al. 2006). Sampling tubes were hammered in dark into freshly exposed surface and were sealed in dark. In the lab outer 2-3 cm of sample in sampling tube was used for radioactive analysis and sample in the interior part was treated with 1 N HCl and 30 % H₂O₂ for removing the carbonates and organic materials respectively. The sample was sieved to get size fraction of 90-150 μm . The quartz grains were then separated by density separation employing 2.58 g/cm³ sodium polytungstate liquid. The extracted quartz grains were etched in 40 % HF for 80 minutes to remove the α -dose affected $\sim 20 \mu\text{m}$ outer layer. Thus obtained pure quartz grains were mounted on stainless steel discs and checked for feldspar contamination using IRSL and then used for equivalent dose measurement.

B) Equivalent dose Analysis

Single aliquot regenerative dose (SAR) (Murray and Wintle, 2000) procedure (Fig. 3.1) and the multiple aliquot additive dose (MAAD) procedure (Aitken, 1985) were used (Fig. 3.2) to estimate the equivalent dose. Some of the samples were analysed using standard growth curve (SGC) procedure. The SGC procedure (Roberts and Duller, 2004; Burbidge, et al., 2006), involves the use of an average dose response curve (SGC) from 10+ aliquots and sensitivity corrected luminescence from other aliquots is read on the SGC to obtain the equivalent dose. SGC procedure assumes that luminescence vs. dose growth variations in luminescence characteristics are minimal such that an average behaviour can be used for all aliquots. Jaiswal, et al., (in

preparation) suggested the use of SGC for sample where the R^2 is ~ 0.9 using 10 aliquots growth curves. One such SGC is shown in Fig 3.3. This has growth curves of 10 aliquots and the R^2 is 0.99. The sensitivity change during read out of natural signal was corrected. One such curve is shown in Fig. 3.4 and the observed NCF is 0.966 i.e., the sensitivity of the sample has been brought up by 3 % by preheat and natural OSL measurement (L_n).

C) Measurement details

A preheat of 260°C for 10 sec and a cut heat 240°C with $2^\circ\text{C}/\text{sec}$ as heating rate was used. Preheat temperature was selected from preheat plateau of the samples as shown in Fig 3.5. Blue light (470 nm) stimulated luminescence (BLSL) was detected in the UV range using EMI 9635Q PMT with 3 mm Hoya U-340 optical filters in front of PMT. All measurements were carried out using an automated Risø TL/OSL TL-15 Reader (Bøtter-Jensen et al., 2000). Purity of quartz was confirmed using IR stimulation before measurement and no feldspar contamination was found in the sample. The dose recovery test also showed that in respect of their luminescence characteristics the samples were well behaved (Fig 3.6). The dose rate of each sample was estimated using thick source alpha counting (TSAC) for U and Th concentrations and gamma counting using NaI(Tl) for K concentration. The average water content in the sample during burial was assumed to be 5 %.

3.2.3 Results

The dose distributions are given in Fig 3.7 and the details of ages are provided in Table 3.1. The choice of appropriate equivalent dose was non trivial (Bailey & Arnold, 2006). For well bleached samples the dose distribution is Gaussian and in principal an arithmetic mean can be used for age estimation. Application of replacement plot (Bailey, 2003a) suggested these samples are well bleached. Thus the equivalent dose can be scaled by the corresponding dose rates (Gy/ka) to get the true burial ages (ka). The ages with the values of equivalent dose and their dose rates are tabulated in Table 3.1.

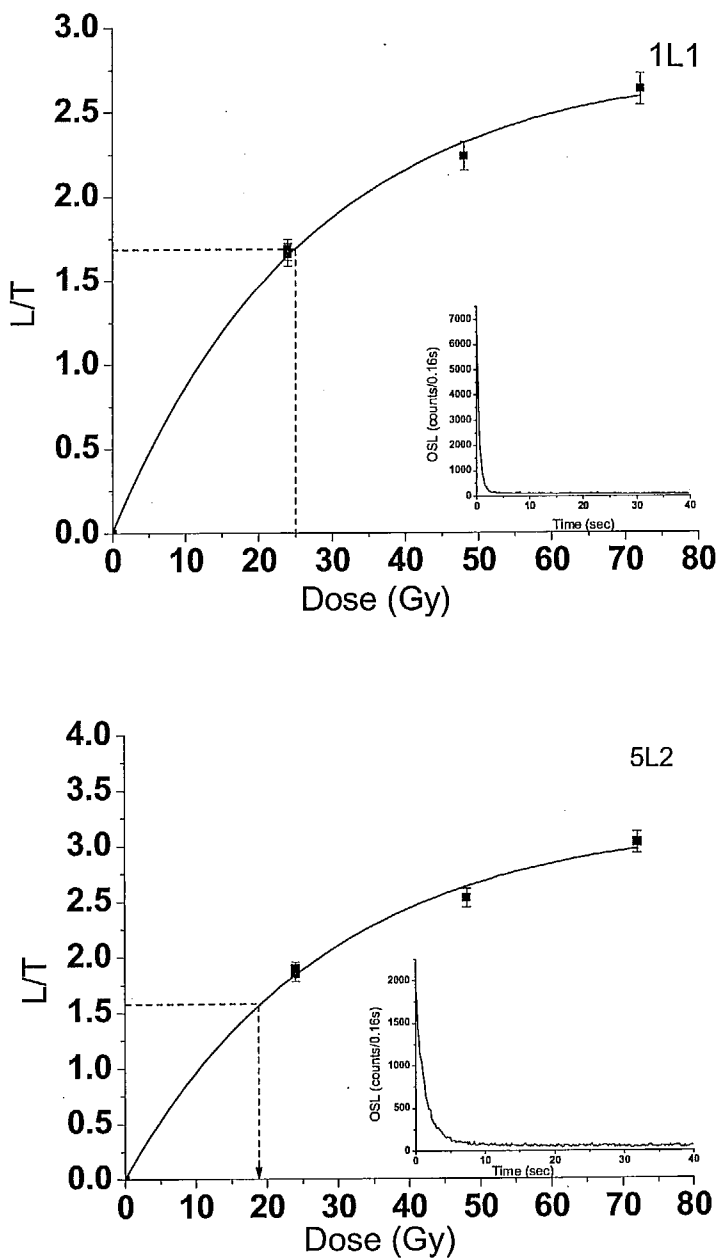


Figure 3.1 The dose response curve (growth curve) using SAR procedure for Oman samples, a) 1L1 and b) 5L2. The inset shows the OSL decay curve.

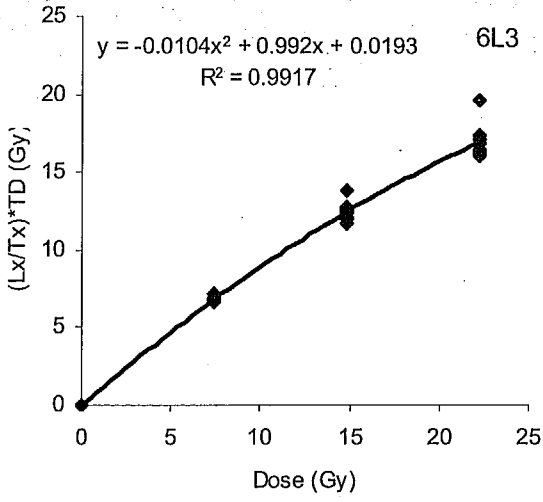


Figure 3.2 A typical MAAD growth curve of sample 6L3.

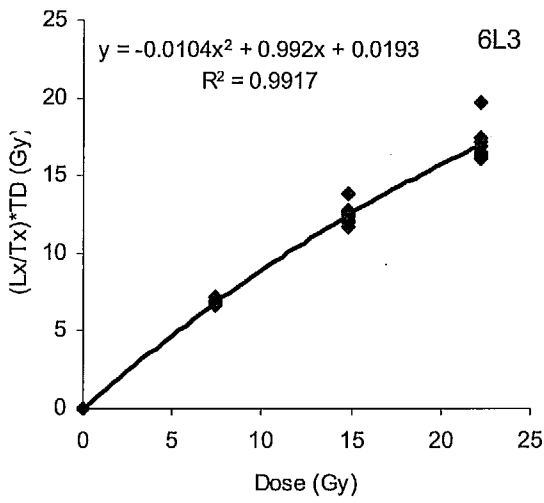


Figure 3.3 Standard growth curve obtained using 10 aliquots of 6L3.

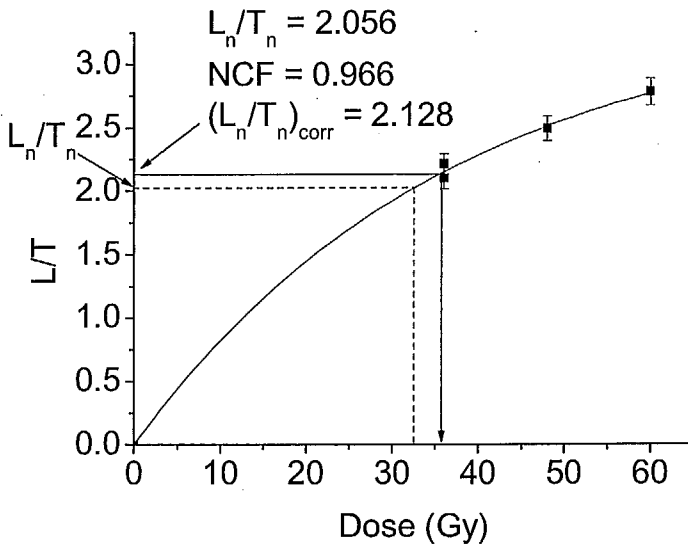


Figure 3.4. The dose response curve of 7L3 and the effect of natural sensitivity correction in obtaining D_e value.

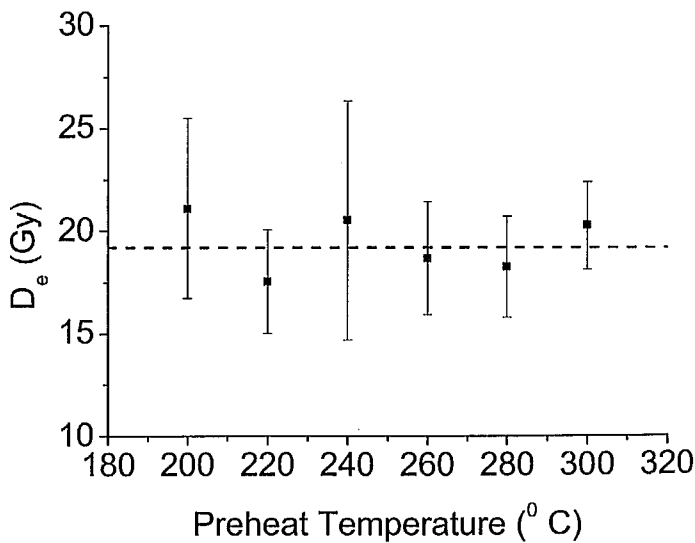


Figure 3.5. Preheat plateau of 1L1. Preheat 260°C was used for the D_e measurements.

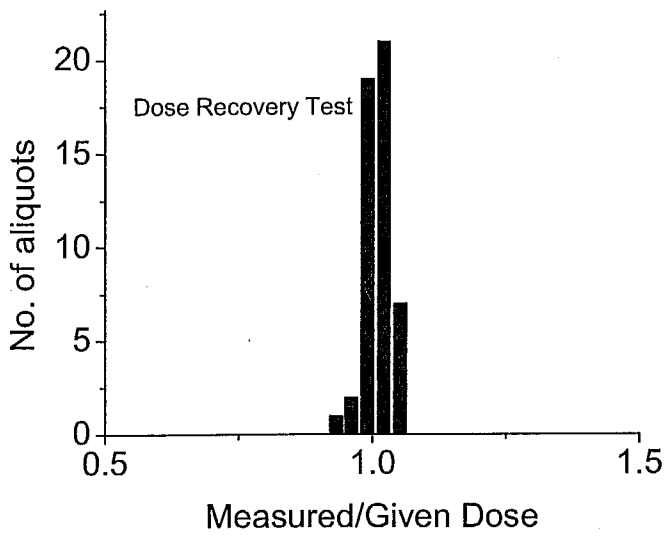


Figure 3.6 The dose recovery test for the sample 7L3 of Wahiba sands.

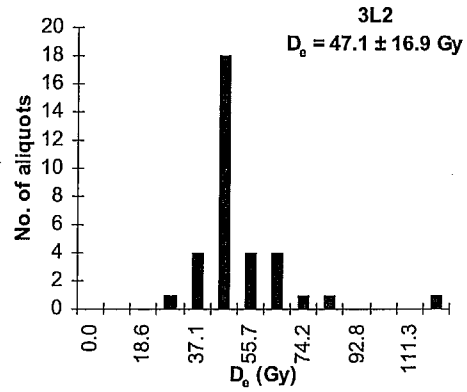
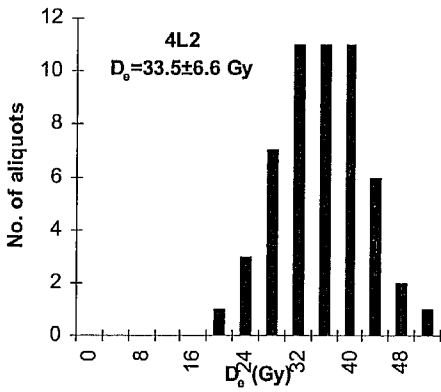
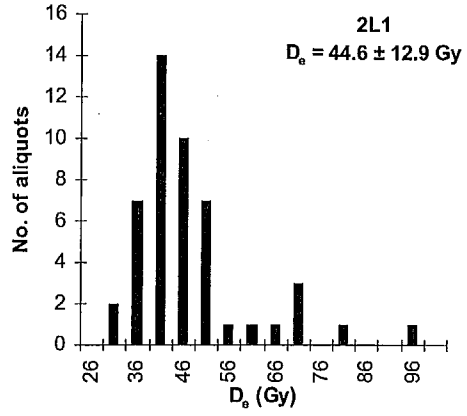
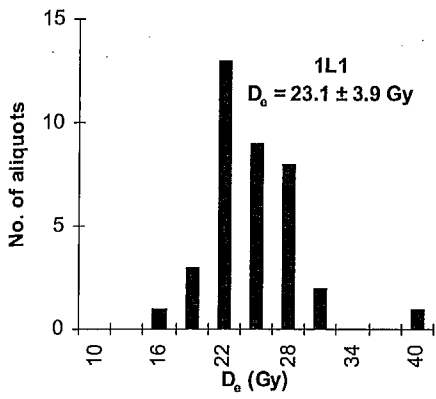


Figure 3.7 Histograms of dose distribution of Wahiba sands. The bin width is the median value of the individual error .

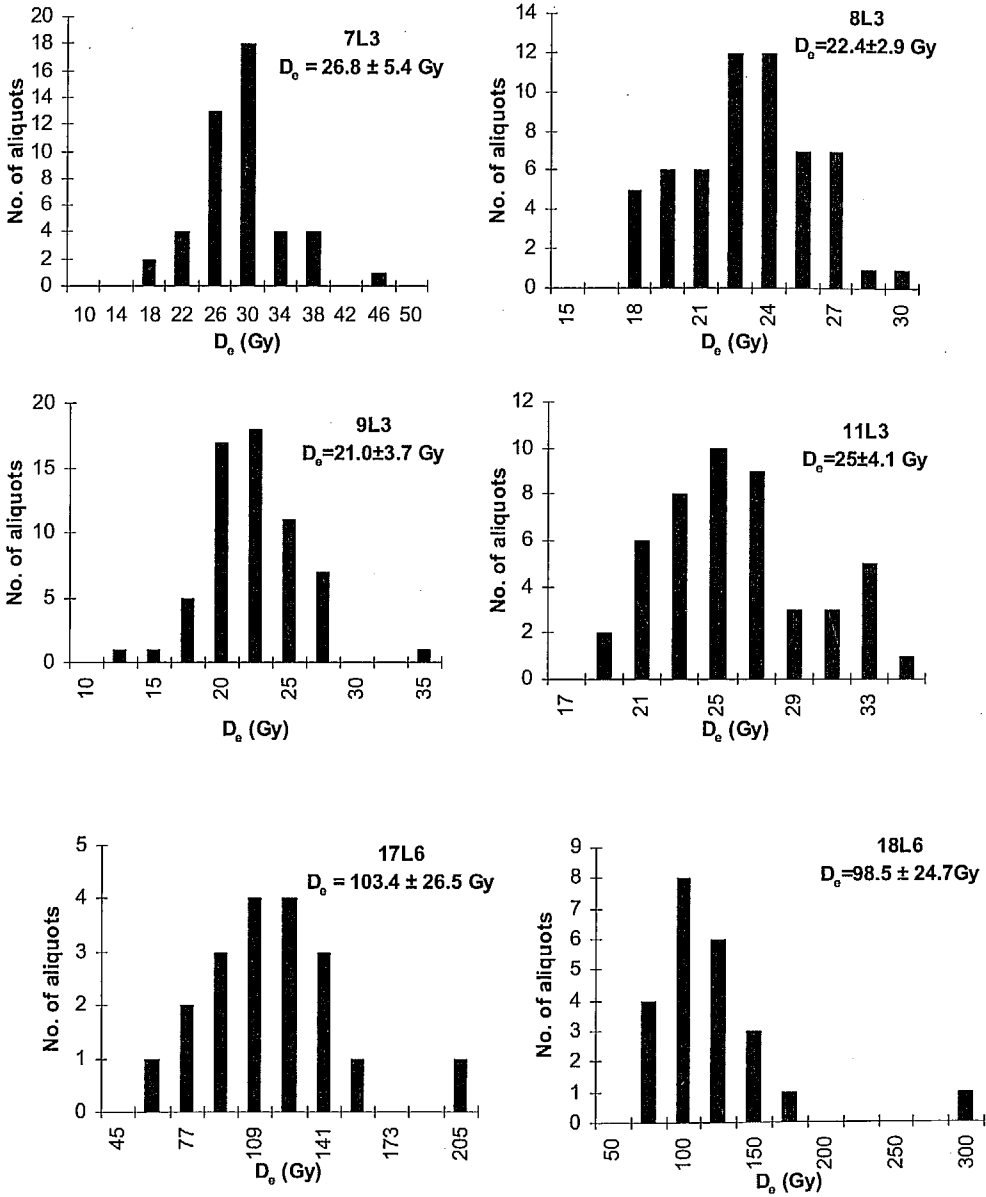


Figure 3.7 Histograms of dose distribution of Wahiba sands. The bin width is the median value of the individual error.

Table 3.1. Wahiba sands results.

| Sample code | (Mean) De (Gy) | U (ppm) | Th (ppm) | K (%) | Water Content (%) | Dose rate (Gy/ka) | (Mean) Age (ka) | Method |
|-------------|-------------------|-------------|-------------|-------------|-------------------|-------------------|--------------------|-------------|
| 1L1 | 23.1 ± 3.9 | 1.11 ± 0.13 | 0.94 ± 0.47 | 0.41 ± 0.04 | 5 | 0.9 ± 0.1 | 26.6 ± 4.7 | SAR |
| 2L1 | 44.6 ± 12.9 | 1.12 ± 0.12 | 1.02 ± 0.44 | 0.91 ± 0.09 | 5 | 1.3 ± 0.1 | 33.2 ± 9.9 | NCF-SAR |
| 3L2 | 47.1 ± 16.9 | 1.17 ± 0.08 | 1.73 ± 0.3 | 0.42 ± 0.04 | 5 | 0.9 ± 0.1 | 49.9 ± 18.1 | NCF-SAR |
| 4L2 | 33.5 ± 6.6 | 1.04 ± 0.1 | 0.98 ± 0.38 | 0.88 ± 0.09 | 5 | 1.3 ± 0.1 | 25.9 ± 5.4 | NCF-SAR-SGC |
| 5L2 | 19.2 ± 2.2 | 1.01 ± 0.08 | 0.96 ± 0.29 | 0.99 ± 0.0 | 5 | 1.4 ± 0.1 | 13.8 ± 1.7 | NCF-SAR-SGC |
| 6L3 | 48.5 ± 8.9 | 1.12 ± 0.11 | 0.8 ± 0.6 | 1.41 ± 0.14 | 5 | 1.8 ± 0.1 | 27.0 ± 5.4 | NCF-SAR-SGC |
| 7L3 | 26.8 ± 5.4 | 1.07 ± 0.24 | 0.95 ± 0.86 | 1.35 ± 0.14 | 5 | 1.7 ± 0.1 | 15.4 ± 3.4 | NCF-SAR-SGC |
| 8L3 | 22.4 ± 2.9 | 0.85 ± 0.01 | 1.8 ± 0.54 | 0.35 ± 0.04 | 5 | 0.8 ± 0.1 | 27.5 ± 4.1 | NCF-SAR-SGC |
| 9L3 | 21.0 ± 3.7 | 1.27 ± 0.01 | 0.63 ± 0.37 | 0.25 ± 0.03 | 5 | 0.7 ± 0.1 | 28.7 ± 5.4 | NCF-SAR-SGC |
| 11L3 | 25.0 ± 4.1 | 1.21 ± 0.07 | 0.95 ± 0.27 | 0.55 ± 0.06 | 5 | 1.0 ± 0.1 | 24.5 ± 4.3 | NCF-SAR-SGC |
| 17L6 | 103.4 ± 26.5 | 1.21 ± 0.11 | 2.58 ± 0.41 | 0.86 ± 0.09 | 5 | 1.4 ± 0.1 | 72.7 ± 19.3 | NCF-SAR |
| 18L6 | 98.5 ± 24.7 | 0.86 ± 0.08 | 1.55 ± 0.28 | 1.02 ± 0.10 | 5 | 1.4 ± 0.1 | 69.1 ± 18.0 | SAR |
| 19L7 | 6.9 ± 2.8 | 0.66 ± 0.08 | 0.78 ± 0.31 | 0.61 ± 0.06 | 5 | 0.95 ± 0.05 | 7.3 ± 2.9 | SAR-SGC |

3.3 Mexican dunes

3.3.1 Sample Description

The Mexican dunes are complex pattern of sand dunes of multiple generations. Luminescence ages were used to provide chronometry frame work for this spatially diverse and complex pattern of dunes (Beveridge et al., 2006). A suite of 23 samples from this region were analyzed to bracket the ages of various event chronology of the dunes.

3.3.2 Methods used

The equivalent doses were determined using single aliquot regeneration (SAR) procedures (Murray & Wintle, 2000) with blue light excitation for fine sand grain sizes using Risø TL/OSL Reader equipped with a beta source (0.120167 Gy/s) for irradiation and blue LEDs (470 nm). For samples which have IR sensitive grains (possibly as inclusions with in the grains, multiple HF etch did not help), modified SAR (Olley, 2004) procedure comprising IRSL prewash was followed. According to this method, before every OSL measurement the IR exposure was done at 70 °C for 100 seconds to bleach the IRSL from IR sensitive grains. Single grain OSL measurements on some selected samples were also carried out. A preheat temperature of 260°C for 10 min and the cut heat temperature 240°C at a heating rate of 2°C/s was used. A typical SAR growth curve is given in Fig. 3.8. The inset shows OSL decay curve. The dose rates were determined on bulk samples using a high resolution hyper pure Ge gamma ray spectrometer. The cosmic ray dose rate was estimated for each sample as a function of depth, altitude and geomagnetic latitude (Prescott & Stephen, 1982). The water content was assessed in the laboratory using field samples as received.

3.3.3 Results

The dose distribution histograms are given in Fig. 3.9. The median error was used as the bin widths. In this sequence, some of the samples were not well bleached, therefore the 'least 10%' values were taken to be a realistic estimate of their burial dose.

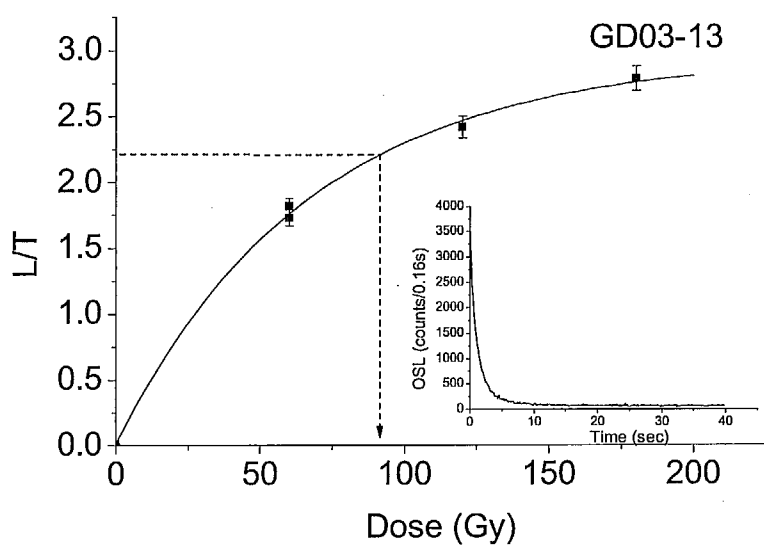


Figure 3.8. The SAR dose response curve for sample GD03-13 (oldest sample). The inset shows the shine down curve.

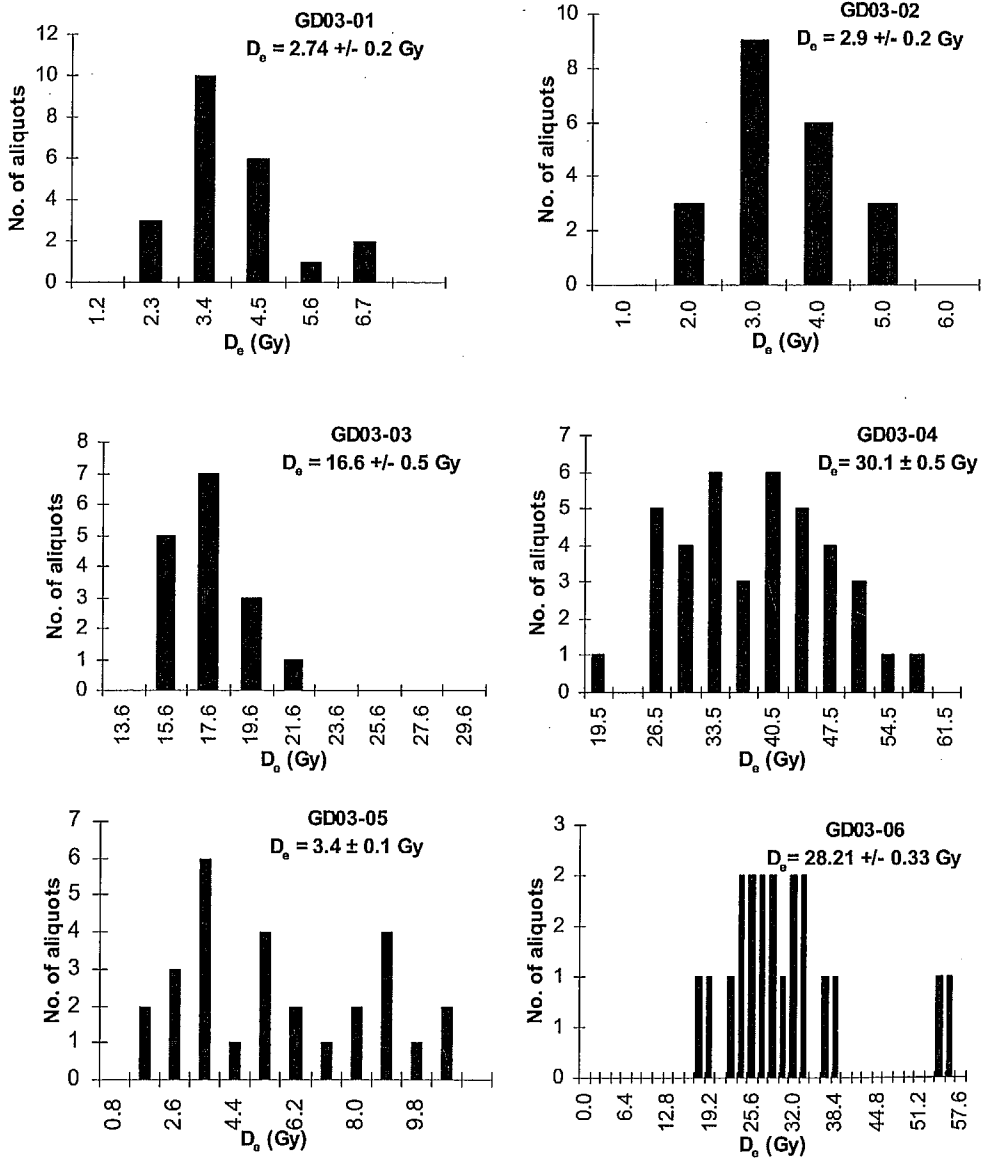


Figure 3.9 Histogram of dose distribution Gran Desierto sample.

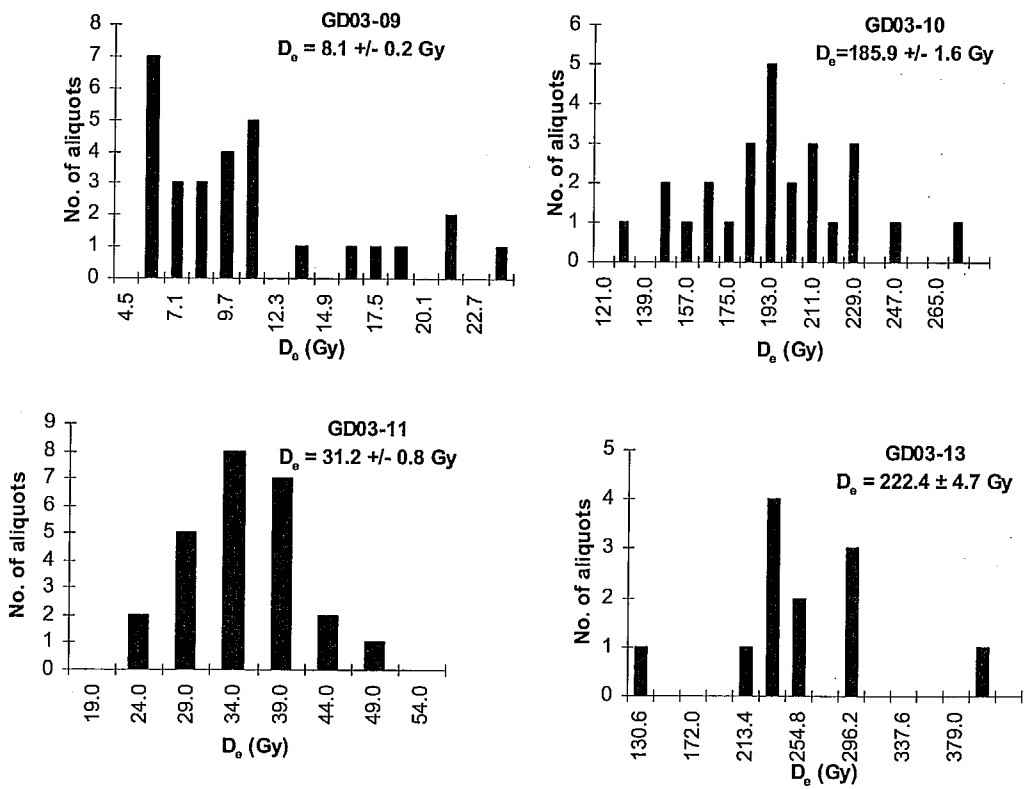


Figure 3.9 Histogram of dose distribution Gran Desierto sample

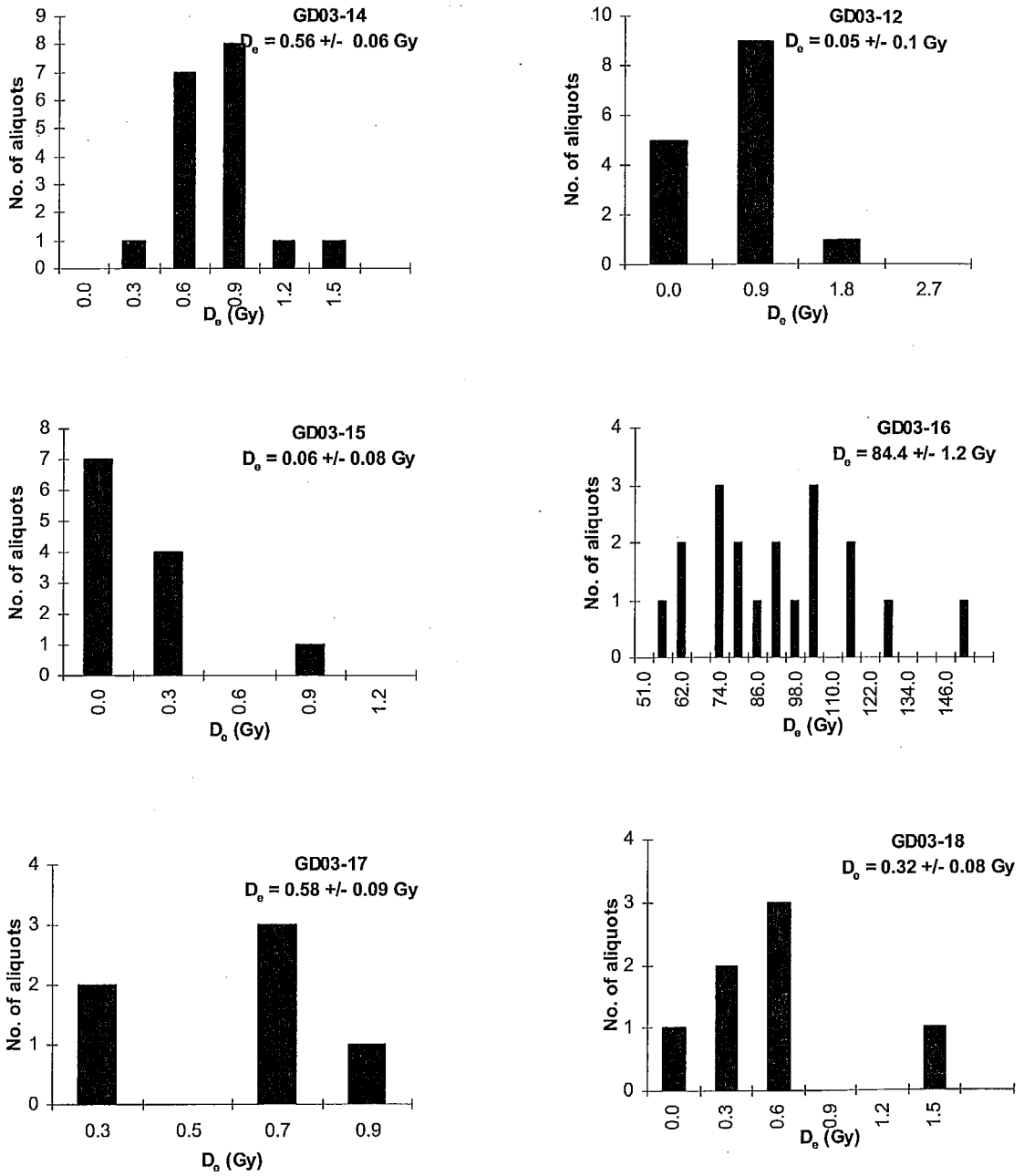


Figure 3.9 Histogram of dose distribution Gran Desierto sample

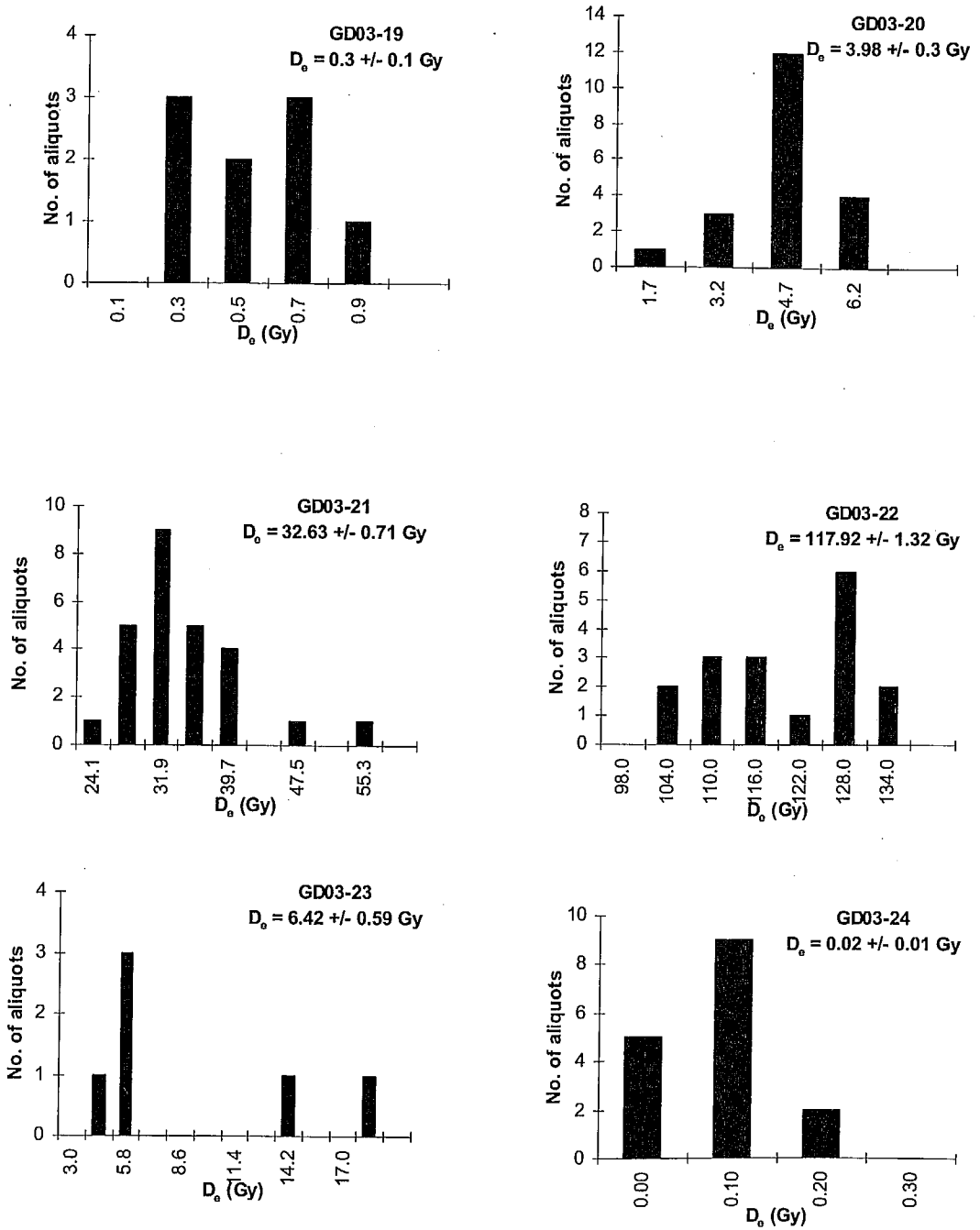


Figure 3.9 Histogram of dose distribution Gran Desierto sample.

Table 3.2. Mexico dunes samples results.

| Sample code | U (ppm) | Th (ppm) | K (%) | Cosmic ray | Water content | Dose Rate (Gy/ka) | No. of Aliquots (no. for analysis) | Weighted Mean Age (ka) | Least 10% Age (ka) |
|-------------|---------|----------|-------|------------|---------------|-------------------|------------------------------------|------------------------|--------------------|
| GD03-01 | 1.19 | 4.22 | 2.22 | 0.1891 | 5 ± 0.25 | 2.8 ± 0.1 | 28 (22) | 1.0 ± 0.1 | 0.5 ± 0.04 |
| GD03-02 | 2.10 | 5.98 | 2.51 | 0.2178 | 3 ± 2 | 3.5 ± 0.2 | 25 (21) | 0.8 ± 0.1 | 0.5 ± 0.1 |
| GD03-03 | 1.10 | 3.68 | 1.71 | 0.1883 | 5 ± 0.25 | 2.3 ± 0.1 | 23 (06) | 7.3 ± 0.4 | 6.0 ± 0.4 |
| GD03-04 | 1.63 | 3.98 | 1.80 | 0.1882 | 8 ± 2 | 2.4 ± 0.1 | 40 (39) | 12.5 ± 0.6 | 9.6 ± 0.5 |
| GD03-05 | 1.85 | 4.95 | 1.53 | 0.2819 | 5 ± 0.25 | 2.5 ± 0.1 | 32 (29) | 1.4 ± 0.1 | 0.6 ± 0.2 |
| GD03-06 | 1.34 | 3.64 | 1.90 | 0.1862 | 10 | 2.4 ± 0.1 | 20 (20) | 12.0 ± 0.5 | 7.3 ± 1.8 |
| GD03-07 | 1.15 | 3.42 | 1.79 | 0.2836 | 5 ± 0.25 | 2.4 ± 0.1 | 20 (18) | 0.02 ± 0.01 | Modern |
| GD03-09 | 2.04 | 7.24 | 1.71 | 0.1607 | 3 ± 2 | 2.8 ± 0.1 | 40 (29) | 2.9 ± 0.2 | 1.7 ± 0.2 |
| GD03-10 | 2.32 | 3.68 | 1.41 | 0.1171 | 3 ± 2 | 2.2 ± 0.1 | 26 (26) | 85.3 ± 4 | 61.5 ± 3 |
| GD03-11 | 0.91 | 2.99 | 1.41 | 0.1862 | 3 ± 2 | 1.95 ± 0.1 | 26 (25) | 16.0 ± 0.9 | 11.6 ± 0.6 |
| GD03-12 | 1.01 | 2.84 | 1.42 | 0.2755 | 5 ± 0.25 | 2.0 ± 0.1 | 26 (15) | 0.02 ± 0.05 | Modern |
| GD03-13 | 0.93 | 3.12 | 1.60 | 0.1757 | 3 ± 2 | 2.1 ± 0.1 | 26 (12) | 104 ± 5.5 | 87.4 ± 4.4 |

| | | | | | | | | | |
|---------|------|------|------|--------|----------|-----------|---------|--------------|------------|
| GD03-14 | 0.80 | 2.67 | 1.43 | 0.1886 | 8 ± 2 | 1.8 ± 0.1 | 25 (18) | 0.32 ± 0.004 | Modern |
| GD03-15 | 0.99 | 3.12 | 1.35 | 0.2866 | 5 ± 0.25 | 2.0 ± 0.1 | 20 (12) | 0.03 ± 0.03 | Modern |
| GD03-16 | 1.00 | 3.55 | 1.49 | 0.1931 | 5 ± 0.25 | 2.0 ± 0.1 | 20 (19) | 41 ± 2 | 26.7 ± 4.7 |
| GD03-17 | 1.08 | 3.26 | 1.57 | 0.2382 | 5 ± 0.25 | 2.2 ± 0.1 | 20 (07) | 0.3 ± 0.04 | 0.13 ± 0.1 |
| GD03-18 | 1.06 | 3.09 | 1.39 | 0.2848 | 5 ± 0.25 | 2.1 ± 0.1 | 20 (08) | 0.15 ± 0.04 | Modern |
| GD03-19 | 1.00 | 3.52 | 1.49 | 0.2225 | 5 ± 0.25 | 2.1 ± 0.1 | 20 (09) | 0.15 ± 0.04 | 0.08 ± 0.1 |
| GD03-20 | 0.96 | 3.18 | 1.56 | 0.1968 | 5 ± 0.25 | 2.1 ± 0.1 | 26 (20) | 1.9 ± 0.2 | 1.1 ± 0.1 |
| GD03-21 | 0.90 | 2.86 | 1.59 | 0.1914 | 5 ± 0.25 | 2.1 ± 0.1 | 26 (26) | 15.8 ± 0.8 | 12.0 ± 0.6 |
| GD03-22 | 1.44 | 4.52 | 1.54 | 0.1962 | 5 ± 0.25 | 2.3 ± 0.1 | 20 (17) | 52.3 ± 2.3 | 44.4 ± 4 |
| GD03-23 | 1.44 | 4.52 | 1.54 | 0.1962 | 5 ± 0.25 | 2.3 ± 0.1 | 20 (06) | 2.9 ± 0.3 | 1.9 ± 0.8 |
| GD03-24 | 1.52 | 2.95 | 1.35 | 0.2842 | 5 ± 0.25 | 2.1 ± 0.1 | 20 (16) | Modern | Modern |

For the remaining well bleached samples rest weighted mean was taken as burial dose. The results are tabulated in Table 3.2.

3.4 Thar desert

3.4.1 Sample description

These samples were from southern margin of Thar desert located in Sabarmati basin. These samples are the source bordering Aeolian dune sands. The geological objective of this study was to understand dune activity in this area.

3.4.2 Methods used

After chemically cleaning the samples from carbonates and organic matters using HCl and H₂O₂, the quartz and other minerals were separated using difference in their densities. The equivalent dose was measured by single aliquot regenerative dose (SAR) procedure (Fig. 3.10). A preheat of 260⁰C for 60 sec and a cut heat was 240⁰C at the heating rate of 2⁰C/s was used. The stimulation source was blue LEDs (470 nm) and the measurement window was restricted to read UV emission from Quartz. NCF-SAR procedure was also applied to samples. These procedures are mentioned in tabulation along with samples stating the protocols that were used.

3.4.3 Results

The dose distributions are given in Fig. 3.11. These samples were also well bleached and hence the burial dose is the arithmetic mean of the measured dose values. These values are tabulated in Table 3.3.

3.5 Single grain dose distribution

Having established the age of the above mentioned sampling sites using single aliquot measurements, the dose distribution in single grain measurements was examined. Single grain analysis offers the only hope for resolving issues of partial bleaching, variability in luminescence and beta dose heterogeneity.

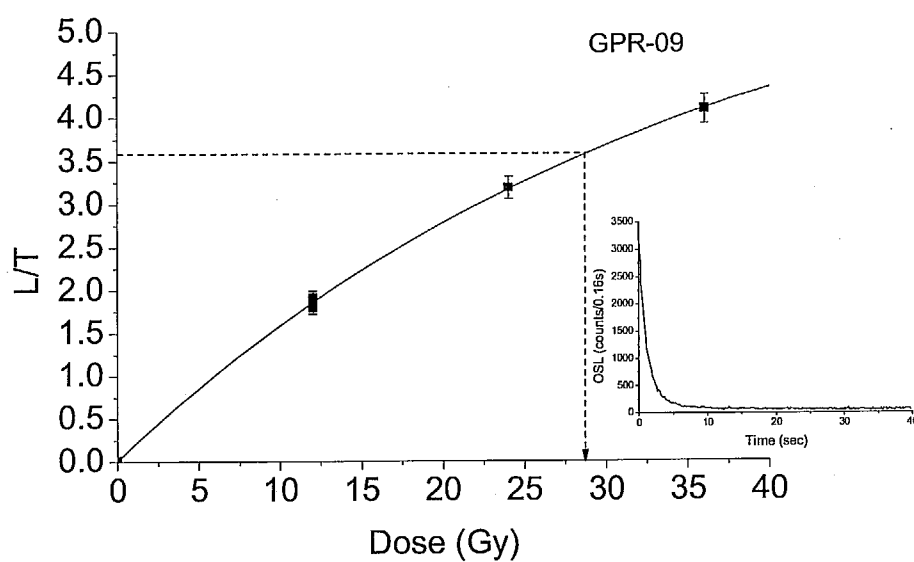


Figure 3.10 The growth curve and shine down curve of GPR-09 (Thar desert sample).

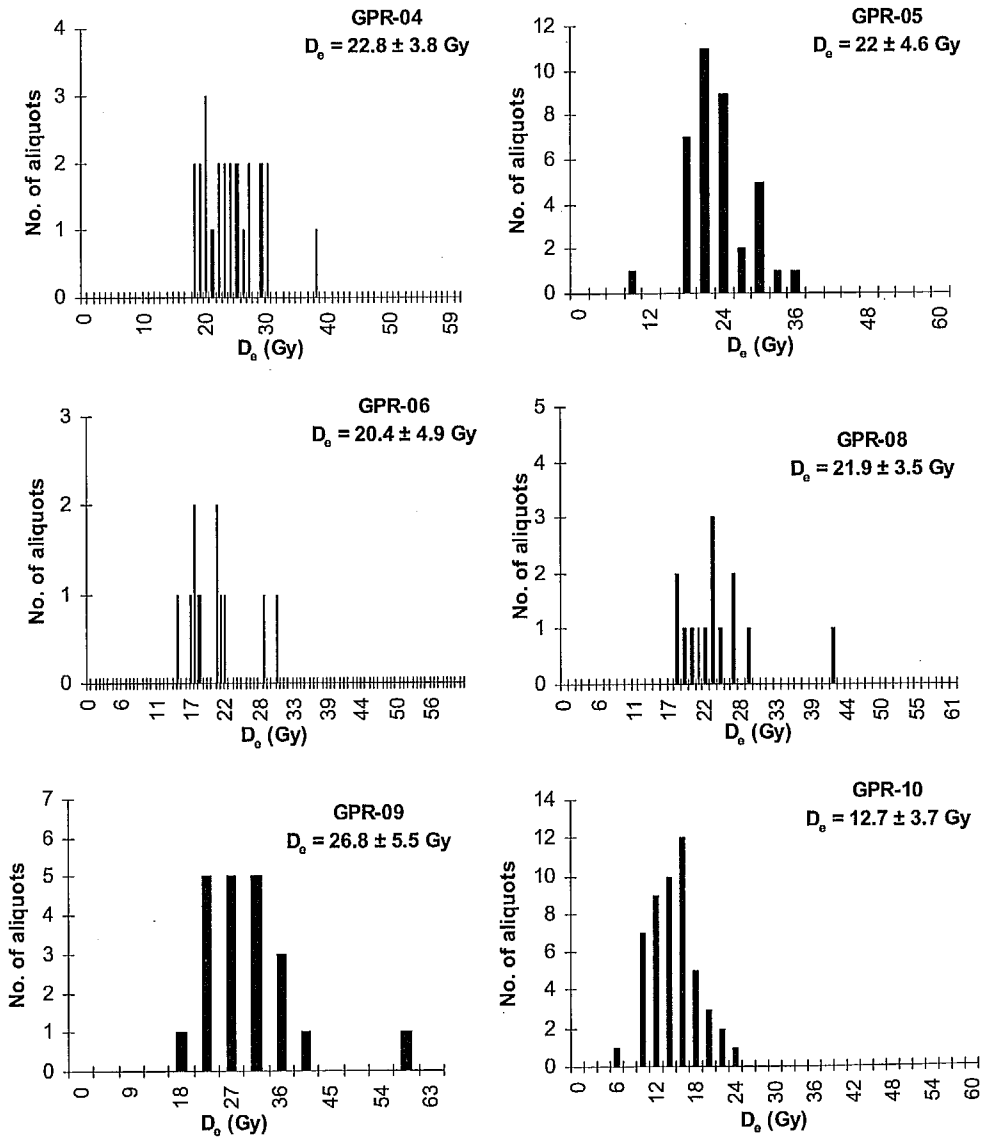


Figure 3.11 Dose distributions of Thar desert samples.

Table 3.3. Thar desert samples results.

| Sample code | Depth | Dose (Gy) | Dose Rate (Gy/ka) | Age (ka) | | Water content (%) | Protocol | No.of Aliquots |
|-------------|-------|------------|-------------------|-----------------|------------|-------------------|-------------|----------------|
| | | | | Arithmetic Mean | Least 10 % | | | |
| GPR-10 | 188 | 13.7 ± 3.7 | 1.2 ± 0.1 | 11.0 ± 3.0 | 7.1 ± 0.6 | 5 | NCF-SAR-SGC | 51 |
| GPR-09 | 238 | 24.6 ± 3.4 | 1.4 ± 0.1 | 18.0 ± 3.1 | 13.6 ± 1.9 | 5 | NCF-SAR | 23 |
| GPR-08 | 288 | 22.9 ± 4.0 | 1.5 ± 0.1 | 15.7 ± 2.9 | 11.9 ± 0.7 | 10 | NCF-SAR | 14 |
| GPR-06 | 388 | 20.4 ± 4.9 | 1.2 ± 0.1 | 16.5 ± 4.1 | 12.2 ± 1.4 | 10 | NCF-SAR | 10 |
| GPR-05 | 438 | 21.1 ± 3.3 | 1.3 ± 0.1 | 16.9 ± 2.9 | 13.1 ± 1.2 | 10 | NCF-SAR | 40 |
| GPR-04 | 488 | 22.8 ± 3.8 | 1.5 ± 0.1 | 14.7 ± 2.6 | 11.5 ± 1.0 | 10 | NCF-SAR | 25 |

Keeping the main objective in mind, samples for single grain measurements were selected. As beta heterogeneity effects are more likely for the samples having low K concentration, the focus was on Wahiba sands ($K < 1.5\%$). The Mexico samples had nearly constant K concentration around 2 %. For the southern Thar desert samples, all the 5 samples were measured as they too had K concentration of $< 1\%$.

The distribution of some selected samples has been plotted in Fig 3.12 as histograms and compared with single aliquot dose distribution of corresponding samples. The bin width is the median of individual errors. In these plots, the spread in single grain dose distribution is more than that of single aliquot measurements by 50 %. In the Table 3.4, RSD (Relative Standard Deviation) of all the single grain dose distributions and that of their corresponding single aliquots are tabulated and the same data is shown in Fig 3.13 as histogram. In following we describe some possible sources for spread in dose distribution.

3.6 Explanation for the spread in dose distribution

The RSD of single aliquot and single grain measurements are very different with $RSD_{SG} \gg RSD_{SA}$. Two factors contribute to the distribution viz., a) sample independent factor and b) sample dependent factor. The sample independent factor sources include a) counting statistics and b) instrumental uncertainty. This source is inevitable in all samples and this error as quantified using counting statistics and measurement on bright samples was 4 % for single aliquot and 10% for single grain. The sample dependent factors comprise (i) bioturbation (ii) partial bleaching (iii) dose heterogeneity and (iv) variations in luminescence characteristics of the grains (Murray and Roberts, 1997; Vandenberghe, et al., 2003).

3.6.1 Bioturbation

Amongst these sources, bioturbation (i.e., mixing due to faunal or soil forming processes) could be ruled out as samples were collected where no obvious evidence of mixing could be noticed. However, at times collection of samples from those doubtful sites become inevitable, in that case proper needs to be followed as discussed by Bateman et al, 2003. In most of the case in the present study, based on field evidences, it was reasonably concluded that bioturbation was not the prominent source (Beveridge et al., 2006; Glennie et al., 2007).

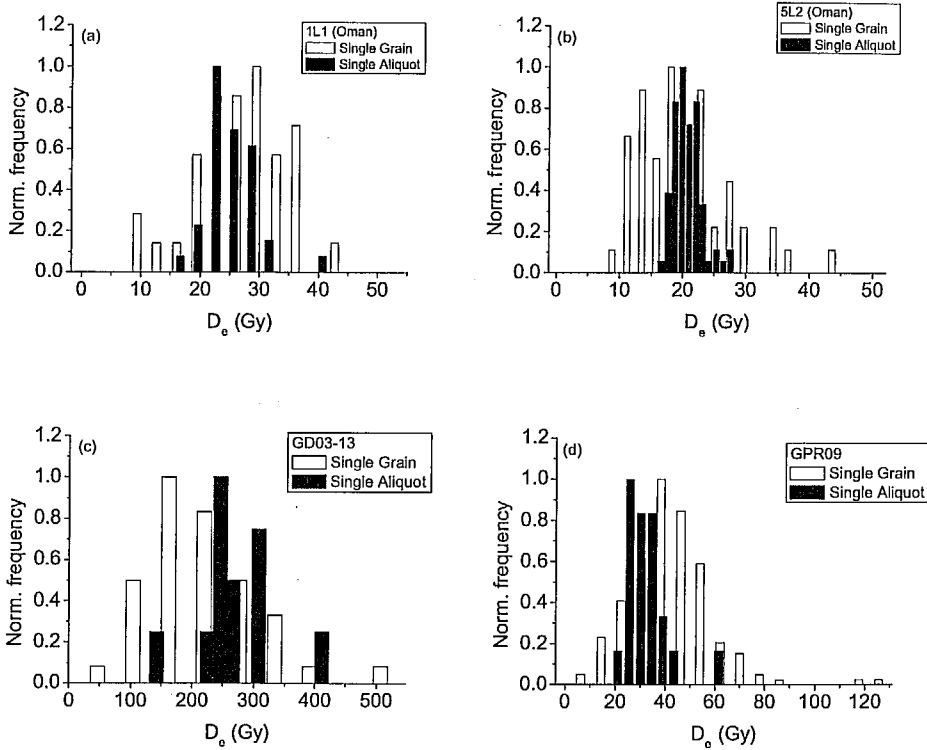


Figure 3.12 Comparison of dose distributions of single aliquot and single grain measurements, a) 1L1, b) 5L2, c) GD03-13 and d) GPR-09.

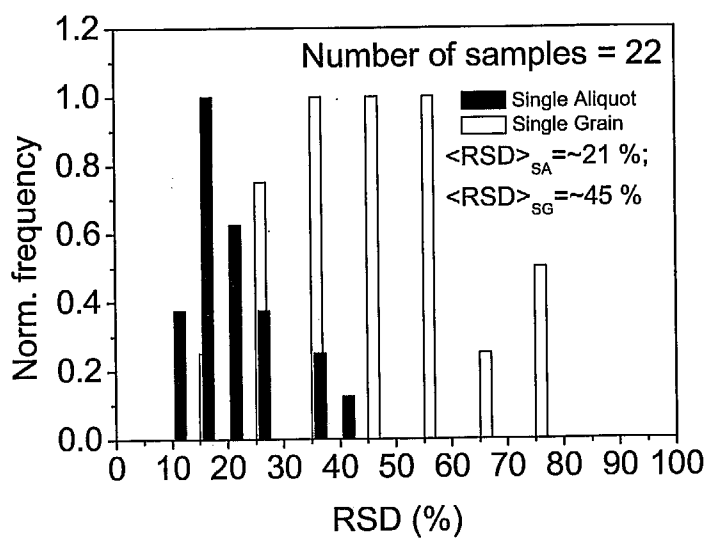


Figure 3.13 Comparison of RSD (%) from the single aliquot and the single grain measurements of 22 samples. The same data set is tabulated in Table 3.4.

Table 3.4. Comparison of RSD of single aliquot and single grain dose distribution.

| Sample Code | RSD ($=\frac{\sigma}{\mu} \times 100$) (%) | |
|-------------|--|------------------------------|
| | Single Aliquot (No. of aliquots) | Single grain (No. of grains) |
| 1L1 | 16.8 (37) | 29.5 (37) |
| 2L1 | 28.9 (50) | 35.9 (22) |
| 3L2 | 35.9 (34) | 33.2 (18) |
| 4L2 | 19.7 (53) | 25 (26) |
| 5L2 | 11.5 (81) | 37.8 (55) |
| 6L3 | 18.4 (26) | 29.6 (6) |
| 7L3 | 20.1 (46) | 37.5 (19) |
| 8L3 | 12.9 (58) | 19.9 (4) |
| 9L3 | 17.6 (61) | 47.2 (29) |
| 11L3 | 16.4 (47) | 54 (25) |
| 17L6 | 25.6 (19) | 50 (67) |
| 18L6 | 25.1 (16) | 71.3 (45) |
| 19L7 | 40.6 (49) | 159.4 (19) |
| GD03-01 | 37.7 (22) | 316 (94) |
| GD03-03 | 11.3 (16) | 158.9 (80) |
| GD03-13 | 24.3 (12) | 46.6 (42) |
| GD03-21 | 20.2 (26) | 63.2 (32) |
| GPR04 | 16.7 (24) | 51.1 (47) |
| GPR05 | 15.6 (37) | 45.5 (29) |
| GPR06 | 24 (11) | 77.3 (47) |
| GPR08 | 17.5 (14) | 53.3 (34) |
| GPR09 | 23.8 (21) | 44 (165) |

3.6.2 Heterogeneous bleaching

The most general case for a sample is that at a grain level pre-depositional bleaching is both heterogeneous and partial. Given that samples are from deserts, as a first approximation it can be assumed that these were well bleached. This aspect was checked further using replacement plot (Bailey et al., 2003a) which indicates that samples were well bleached. The replacement plot procedure is based on the suggestion that the bleaching status of a sample during transportation can be checked by comparing the D_e based on late light signal. Two samples are shown in Fig. 3.14. This test shows that RB3 was partially bleached while 1L1 was well bleached.

3.6.3 Variations in the luminescence characteristics

Variations in the luminescence characteristics of grains can introduce significant scatter in paleodose. In principle variations like sensitivity, dose response curve should not introduce any scatter in data, if it can be assumed that the sensitivity correction using the test dose OSL following every regeneration and natural OSL properly corrects for all such changes. If however, the sensitivity of OSL components changes drastically during measurement process, a larger scatter is to be expected. Such scatters are quantified using dose recovery test of the sample, by giving a known dose after bleaching the natural luminescence and by using SAR protocol to record this dose. Typically the recorded doses are within 4 % and 10 % (Thomsen, 2003) for single aliquot and single grain procedure respectively, and this error is added to other errors in the equivalent dose. In present study the dose recovery was within ~4 % and ~12 % using single aliquot and single grain respectively for these samples. But these numbers do not account for the total RSD values obtained from the actual dose distribution.

3.6.4 Variations in the microdosimetry

The range of beta particle and the energy attenuation of beta particle through matter are shown in Fig. 3.15. A potassium (K) source delivers its dose to surrounding matrix up to a certain range. In the sediments, quartz grains receive most of its beta dose from the K contained in K-feldspar.

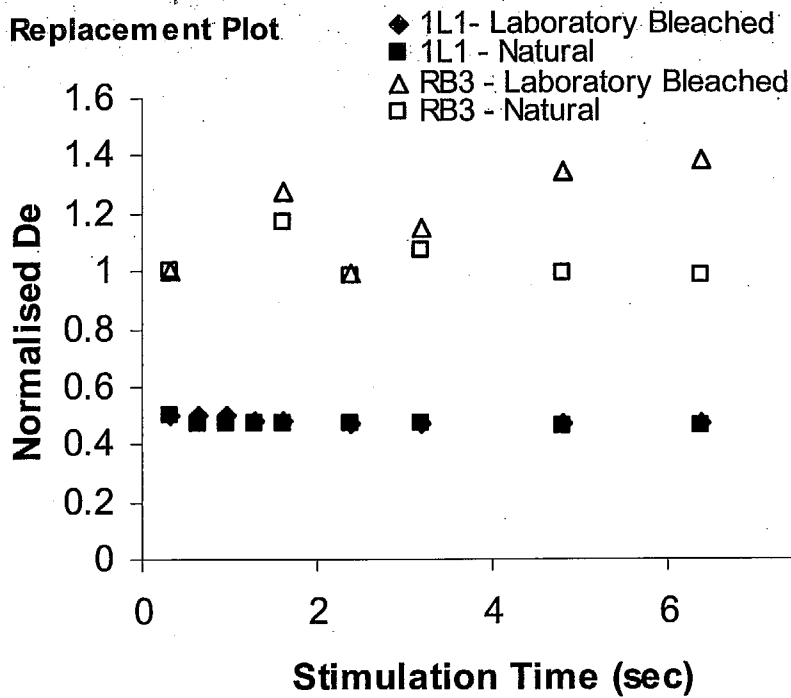


Figure 3.14 Replacement plot of one well bleached sediment (1L1) and one partially bleached sediment (RB3).

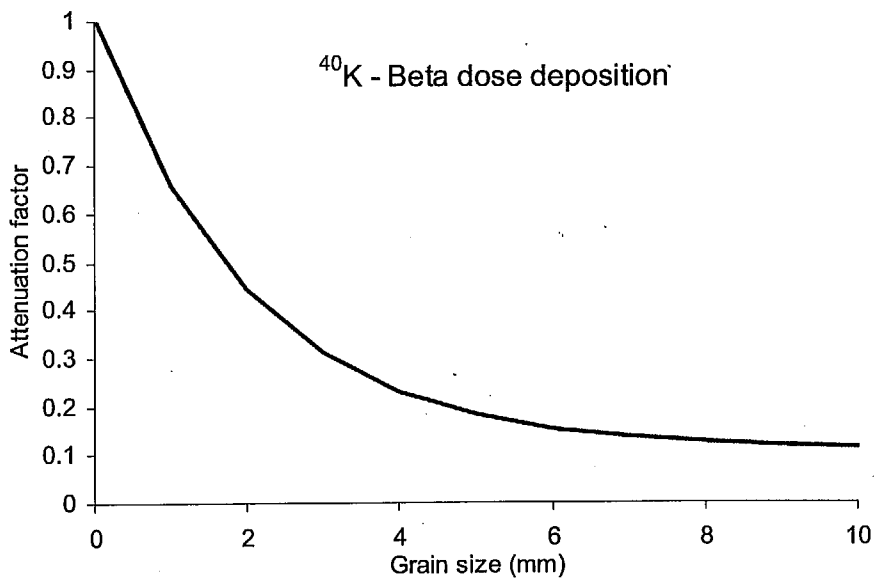


Figure 3.15 Dose deposition of ⁴⁰K's beta in the quartz grain.

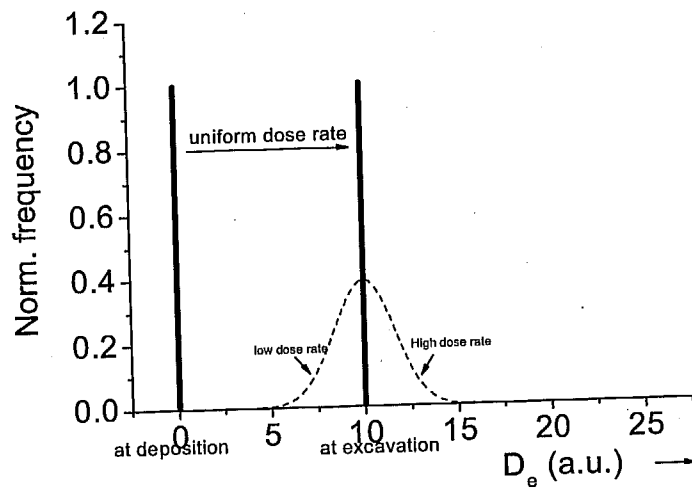


Figure 3.16 Schematic diagram for showing spread in dose distribution due to type of distribution of potassium source particles.

The dose to the quartz grains thus depends on the distribution of the K-feldspar and the manner the beta particles emanating from these, deliver dose along their trajectory. As the beta particle range is ~ 2.27 mm, if the quartz grains which are separated from the K-feldspar particles on spatial scale of millimeter, then these grains will receive variable beta dose leading to a variability in beta doses to grains. This is illustrated in Fig. 3.16. Grains proximal to the source receive maximum dose and the distant grains receive no dose. This could be the reason for large spread in data set. These arise due to the fact that minerals such as K-feldspars and zircon possess internally high radioactivity and hence only a few grains provide for the total K content. This fact leads to heterogeneous distributions of dose.

3.7 Summary

In this chapter, the chronology of Wahiba sands, Mexico dunes and southern Thar desert samples are presented using single aliquot procedure. The measurements of dose distribution of single grains are presented. The RSD in single aliquot and single grain measurements are $\sim 18\%$ and $\sim 35\%$ respectively. These values are obtained after accounting for the experimental error. Being well bleached grains this spread was unexpected and consideration of various possible sources suggest that the heterogeneity of beta dose distribution in the matrix could be the most probable cause for this error. Chapters 4 and 5 examine this aspect in more detail.

The Spatial Heterogeneity of Beta Dose in Sediments

4.1 *The problem*

The equivalent dose distribution in the single grain luminescence dating offers a promise for identification of the most bleached grains for age calculations. However, as discussed in the previous chapter, large range of values of the relative standard deviation (RSD) of the equivalent dose distribution, even for well bleached desert sand samples, indicated the presence of additional effects. One of the possible causes is spatially heterogeneous distribution of beta dose, within a sediment matrix.

We suggest that microscopic fluctuations in the spatial distribution of feldspar containing ^{40}K β emitters (termed as hotspots) can cause heterogeneous distribution of dose rate. In this chapter we model these fluctuations to quantify their effect on the distribution of doses in quartz. The dose to a quartz grain from a given spatial configuration of the hotspots within a sphere of maximum beta range is computed and

this is then averaged over all possible configurations, to arrive at the dose rate/equivalent dose distribution. The net effect of such a distribution is the estimated as a function of potassium concentration (lower the potassium, higher the hotspot heterogeneity and larger is the equivalent dose distribution). This non-uniformity in the spatial distribution of dose arises due to the occurrence of ^{40}K containing feldspar grains, on a scale comparable to the mean range of beta particles from ^{40}K . Even though feldspar may be homogeneously distributed on a macroscopic scale, i.e., at the level of typical sample sizes used for analysis, intrinsic statistical fluctuations occur on the scale of beta particle ranges, especially at low hotspot concentrations.

The approach described here is based on the following scenario of radiation exposure to a quartz grain. The radiation dose received by quartz grains consists of a uniform component and a non-uniform hotspot component. The uniform component is due to gamma and beta radiation emitted by the daughter products of natural uranium and thorium and, is assumed to be homogeneously distributed in sediment. Under such a configuration, a given quartz grain will be irradiated from all the hotspots that occur within a sphere, with its radius defined by the maximum range of beta particles. However, as the number and the position distribution of these hotspots varies from grain to grain, a different microscopic environment for each of the grain is to be expected. The mean inter-particle distance between two hotspots is on a scale at which microscopic non-uniformity becomes evident. Qualitatively, when this distance becomes comparable to, or greater than the mean range of ^{40}K beta particles, statistical fluctuations in their number and spatial distribution will give rise to varying doses to different quartz grains. It is easy to estimate that for about 1% content in a sediment, the mean inter-particle distance between feldspar grains is about 0.4 mm. This is comparable to the mean range of about 0.8 mm (maximum range is 2.27 mm) for ^{40}K beta particles. One then needs to model the consequence of these fluctuations through an appropriate statistical formalism.

It may be noted that it is not just the fluctuations in the number of beta emitters around the grain that are responsible for dose broadening. Fluctuations in this number can be easily accounted for by Poisson statistics and can be shown to yield less than 4% RSD at K concentrations of 1%. The main source of heterogeneity pertains to the fluctuations in the distance of hotspots from quartz grains. The occasional

configurations in which the grains find themselves proximal to hotspots, lead to large doses and hence to non-Gaussian distributions.

In order to address the fluctuations mentioned above, it is necessary to develop a rigorous framework by combining well established statistical techniques with the physical scenario of the problem. For the present, we limit ourselves to a first principles' development of these techniques. In the formulation of the problem, the following assumptions are made,

- a. The sample comprises quartz and feldspar grains, only. The higher internal K content of K-feldspar (stoichiometrically 14%, but some what lower on an average) implies that only a few grains of K feldspars (termed hotspots) are needed to give the average K content of sediments. Typically for 1 % K, the volume fraction of feldspars grains is 7 %.
- b. The quartz grains and hotspots (beta emitters) form a random mixture and have spatially uniform mean concentrations (Fig. 4.1) at the level of the size of a typical sample that is collected. However, the hotspot distributions around quartz show non-negligible statistical fluctuations at microscopic levels, i.e. within distances of the order of mean beta particle range.
- c. All grains including the hotspots are of the same size. In nature, the size distribution will be poly-disperse; however a median diameter of 200 μm is assumed here for simplifying the calculations.
- d. The volume fraction occupied by the hotspots is small ($< 25\%$). This assumption is crucial for assigning uncorrelated probability distributions for the position of feldspar centres. In the present framework this approximation limits the applicability of the theory to samples with low concentrations. At higher concentrations, the feldspar position distributions get correlated and the excluded volume corrections become important.
- e. All the quartz grains have identical luminescence characteristics and therefore can be measured with the same precision.

The objective here is to derive an analytical expression for beta dose contribution from these hotspots to individual quartz grains in an infinite sediment matrix. The results obtained are further confirmed by numerical simulation.

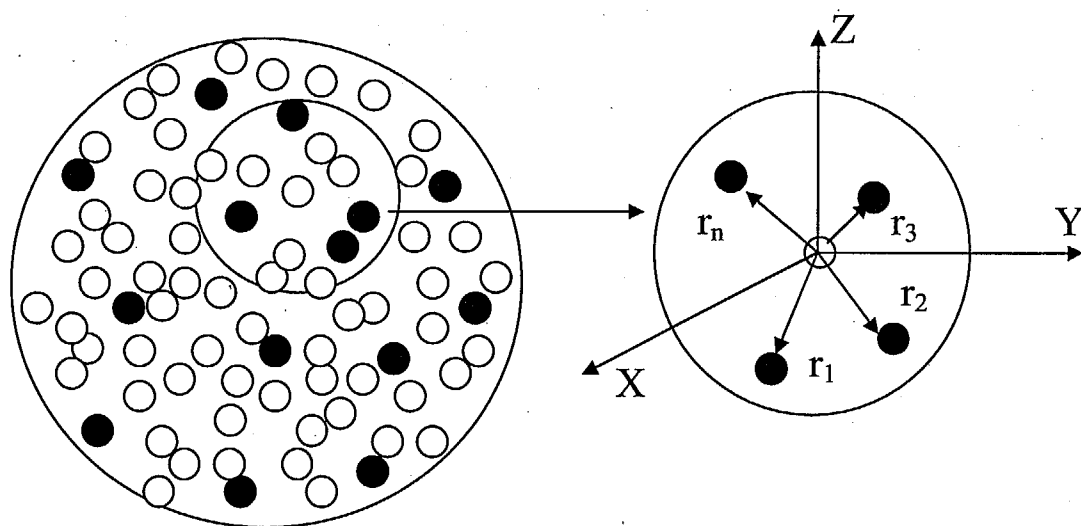


Figure 4.1

a) Distribution of quartz (open circles) grains and ^{40}K hotspots (closed circles).

b) Schematic of dose delivered to a grain located at the centre of the coordinate system. The circle represents the volume of interest and its radius is the maximum range of beta particles from potassium (^{40}K).

4.2 Mathematical Formulation

If it is considered that the sample matrix comprises quartz and feldspar (hotspot) grains, the number of hotspots (μ) present in the sample matrix can be estimated using the stoichiometric K i.e. 14 % (w/w) in a K-feldspar grain. Thus, if sediment comprised feldspar grains only, then the total K concentration will be 14 %. However, typical K concentration in sediments is about 1-2 %. If it is assumed that mineral grains comprising the sediment are spherical, then the number of hotspots for a known K concentration (k), in a sediment volume with a radius corresponding to the range of the most energetic beta particle ($R_{\max} = 2.27$ mm) from ^{40}K can be computed by the relation,

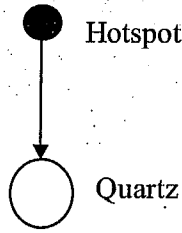
$$\mu = \frac{kR_{\max}^3}{14r^3} \quad (4.1)$$

where, r = radius of the grain (100 μm).

Thus a sample with 1 % K will have 835 hotspots. The dose to a grain is affected by two types of spatial fluctuation of hotspots, i) fluctuation in their actual number in a radius R_m and, ii) positional fluctuations. These can be examined in a statistical framework by examining a hypothetical sphere. We first examine the dose-distance relationship.

4.2.1 Dose-distance relationship

The next question is manner in which the beta energy from a hotspot is delivered to a quartz grain. Since electronic interaction of beta particles with the matrix implies a loss of energy of beta particles along their trajectory in the matrix, the net dose delivered to a quartz grain depends upon the distance between the hotspot and the quartz grain. For example, maximum energy will be deposited at the adjacent grain and no energy is delivered to a grain at a distance exceeding the range of the most energetic beta particle. Thus, the absorbed beta dose in the sphere of influence of hotspot will vary systematically as a function of distance from hotspot. This dose distance relationship can be derived by considering a quartz grain of density ρ_s at some distance R from a hotspot.



The energy deposited per unit time at a volume element is

$$= \frac{Q_H}{4\pi r^2} \frac{dE}{dR} dV \int_{E_{\min}}^{E_{\max}} f(E) dE \quad (4.2)$$

where Q_H = Activity of the hotspot;

r = Radius of the hotspot;

E = beta particle energy at a distance R

$f(E)$ = Energy spectrum of beta particles

$$= \frac{Q_H}{4\pi r^2} \frac{dE}{dR} \frac{dm}{\rho_s} \int_{E_{\min}}^{E_{\max}} f(E) dE \quad (4.3)$$

Energy deposited per unit time at the grain per unit mass is

$$= \int_r^{R_{\max}} \frac{Q_H}{4\pi r^2 \rho_x} \frac{dE}{dR} \left[\int_{E_{\min}}^{E_{\max}} f(E) dE \right] dR \quad (4.4)$$

Eq. (2) becomes,

$$= \frac{Q_H}{4\pi r^2 \rho_x} \left[\int_{E_{\min}}^{E_{\max}} f(E) dE \right] \left[\int_r^{R_{\max}} \frac{dE}{dR} dR \right] \quad (4.5)$$

$$\dot{D}_H = \frac{Q_H}{4\pi r^2 \rho_s} \int_r^{R_{\max}} p(R) \left(\frac{E}{R} \right) dR \quad (4.6)$$

where $p(R)$ = Normalised range spectrum of beta particles from ^{40}K ;

E/R = Stopping power (approximation).

The integral on the RHS of Eq. (4.6) has the dimension of energy. However, it is easier to evaluate a dimensionless integral. Dimensionless variables can be defined as follows,

$$\rho = \frac{r}{R_{\max}}, \quad x = \frac{R}{R_{\max}}, \quad y = \frac{E}{E_{\max}} \quad (4.7)$$

such that $0 < \rho, x, y < 1$.

where E_{max} = maximum beta energy from ^{40}K (1.36 MeV) (Kelly et al., 1959); R_{max} = corresponding maximum range (2.27 mm).

Substituting these dimensionless variables in Eq. (4.6) we get,

$$\dot{D}_H = \frac{Q_H}{4\pi\rho_s R_{max}^2} \frac{1}{\rho^2} \int_p^1 p(x) dx \frac{E_{max}}{R_{max}} \frac{y(x)}{x} \quad (4.8)$$

$$\dot{D}_H = \frac{Q_H}{4\pi\rho_s R_{max}^2} \frac{1}{\rho^2} \int_p^1 p(x) dx \frac{E_{max}}{R_{max}} \frac{y(x)}{x} \quad (4.9)$$

$$\dot{D}_H = \frac{Q_H E_{max}}{4\pi\rho_s R_{max}^3} \frac{1}{\rho^2} \int_p^1 p(x) \frac{y(x)}{x} dx \quad (4.10)$$

where $p(x)$ = Normalised range spectrum function [Eq. (4.30) and Fig. (4.2)];

$y(x)$ = Fitted function for the range energy relationship [Eq. (4.31)].

$$\dot{D}_H = \dot{D}_c g(\rho) \quad (4.11)$$

where

$$g(\rho) = \frac{1}{\rho^2} \int_p^1 p(x) \frac{y(x)}{x} dx \quad (4.12)$$

$$\dot{D}_c = \frac{Q_H E_{max}}{4\pi\rho_s R_{max}^3} \quad (4.13)$$

$g(\rho)$ is the desired dose distance relationship.

4.2.2 Dose distribution

The above relationship gives dose-distance relationship for a pair of a hotspot and a quartz grain. In a sediment matrix several such pairs arise from a random distribution of hotspots in a matrix of quartz grains. Thus a single quartz grain will receive dose from several hotspots placed at variable distances upto the beta range ~ 2.27 mm. Let there be N hotspots in a large volume of radius $R_\infty \gg R_{max}$. R_∞ is chosen because in a real situation the quartz grain may also receive beta dose from a hotspot of U and Th whose spheres of influence (R_{max}) will have some overlap with that of the K -hotspot. R_∞ will encompass all such hotspots that deliver dose to the quartz grain under consideration. Assuming that irradiation from any hotspots follows the law,

$$\dot{D}_{H,i} = \dot{D}_c g(\rho_i) \quad (4.14)$$

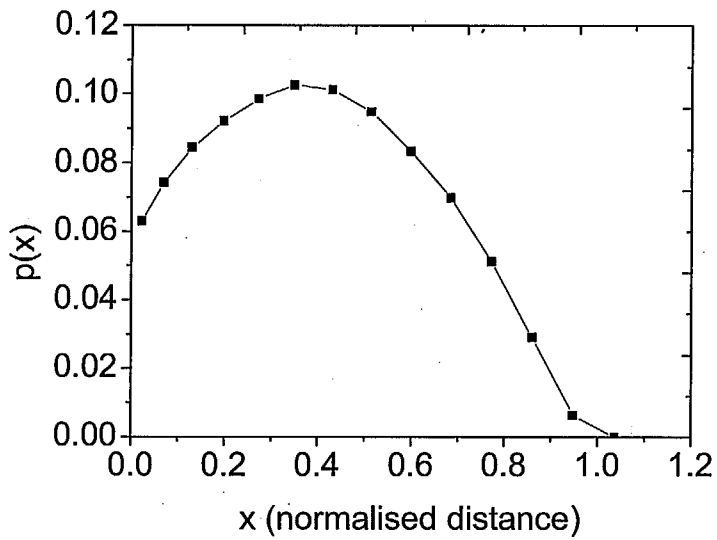


Figure 4.2 Normalized beta-range spectrum of ^{40}K fitted to Eq. (4.30).

$g(\rho_i)$ is a generalized response function such that

$$0 < \rho_i < \rho_\infty, \rho_\infty = \frac{R_\infty}{R_{\max}} \quad (4.15)$$

The number density of hotspots in entire matrix can be defined by γ , such that

$$\gamma = \frac{N}{\frac{4\pi}{3} R_\infty^3} \quad (4.16)$$

The total dose rate due to all the hotspots is given by

$$\dot{D} = \sum_{i=1}^N \dot{D}_c g(\rho_i) \quad (4.17)$$

For a finite duration T of irradiation, it can be assumed that the dose is entirely deposited in the grain due to all the hotspots and can be measured exactly. Hence the mathematical form is,

$$D - \sum_{i=1}^N D_c g(\rho_i) = 0 \quad (4.18)$$

The above equation can be expressed in terms of distribution as follows,

$$\phi(D) = \delta \left(D - D_c \sum_{i=1}^N g(\rho_i) \right) \quad (4.19)$$

In natural sediments however, the quartz grains are likely to be surrounded by varying configuration of hotspots due to statistical fluctuations at the microscopic level. The number of hotspots within R_m , as well as their positions (ρ_i), will vary from grain to grain. The doses will also vary from grain to grain. Consequently, a larger dose distribution is obtained. In experiments, this is observed as the frequency distribution histogram. Mathematically, this distribution is the sum of the individual delta-function distributions of the type shown in Eq. (4.19), taken over all possible configurations after weighting by their probability of occurrence. This is known as configuration averaging. The probability of occurrence is assumed to follow uniform distribution and single particle distribution without correlation.

Now, given a uniform distribution of hotspots,

$$f(\rho_i) \approx \frac{3r_i^2 dr_i}{R_\infty^3} \quad (4.20)$$

$$f(\rho_i) \approx \frac{3\rho_i^2 d\rho_i}{\rho_\infty^3} \quad (4.21)$$

The dose-distribution function due to all the hotspots around the grain is

$$\phi(D)dD = \int_0^{\rho_\infty} \dots \int_0^{\rho_\infty} \frac{3\rho_1^2}{\rho_\infty^3} \dots \frac{3\rho_N^2}{\rho_\infty^3} d\rho_1 \dots d\rho_N \times \delta\left(D - D_c \sum_{i=1}^N g(\rho_i)\right) dD \quad (4.22)$$

This dose distribution in grains arises due to the statistical fluctuations in the position of hotspots and fluctuations in number density of hotspots. Using an arbitrary scaling factor K , the dose can be scaled as follows,

$$\text{Let } \xi = \frac{D}{KD_c} \text{ then } \xi = \sum_{i=1}^N \frac{g(\rho_i)}{K} \quad (4.23)$$

By using the scaled variable ξ , the dose distribution is

$$\phi(\xi)d\xi = \int_0^{\rho_\infty} \dots \int_0^{\rho_\infty} \frac{3\rho_1^2}{\rho_\infty^3} \dots \frac{3\rho_N^2}{\rho_\infty^3} d\rho_1 \dots d\rho_N \times \delta\left(\xi - \sum_{i=1}^N \frac{g(\rho_i)}{K}\right) d\xi \quad (4.24)$$

This is the equation for dose distribution in the integral form. Eq. (4.24) can be verified by simplification.

Let $\bar{\xi}$ be the mean of ξ :

$$\begin{aligned} \bar{\xi} &= \int_0^\infty \phi(\xi) \xi d\xi \\ \bar{\xi} &= \int_0^\infty \left[\int_0^{\rho_\infty} \dots \int_0^{\rho_\infty} \frac{3\rho_1^2}{\rho_\infty^3} \dots \frac{3\rho_N^2}{\rho_\infty^3} d\rho_1 \dots d\rho_N \times \sum_{i=1}^N \frac{g(\rho_i)}{K} \right] d\xi \\ \bar{\xi} &= \frac{1}{K} \int_0^\infty \left[\int_0^{\rho_\infty} \frac{3\rho_1^2 g(\rho_1) d\rho_1}{\rho_\infty^3} \left(\int_0^{\rho_\infty} \frac{3\rho_2^2}{\rho_\infty^3} d\rho_2 \right) \dots \left(\int_0^{\rho_\infty} \frac{3\rho_N^2}{\rho_\infty^3} d\rho_N \right) + \right. \\ &\quad \left. \int_0^{\rho_\infty} \frac{3\rho_2^2 g(\rho_2) d\rho_2}{\rho_\infty^3} \left(\int_0^{\rho_\infty} \frac{3\rho_1^2}{\rho_\infty^3} d\rho_1 \right) \dots \left(\int_0^{\rho_\infty} \frac{3\rho_N^2}{\rho_\infty^3} d\rho_N \right) + \dots N(\text{times}) \right] d\xi \end{aligned} \quad (4.25)$$

Inside the bracket $\int_0^{\rho_\infty} \frac{3\rho_i^2}{\rho_\infty^3} d\rho_i$'s are equal to 1 and are simplified after integrating from

0 to 1, since $g(\rho) \neq 0$ for $0 < \rho < 1$ and $g(\rho) = 0$ for $\rho > 1$ The above equation becomes,

$$\bar{\xi} = \frac{N\bar{g}}{K\rho_\infty^3} \quad (4.26)$$

where

$$\bar{g} = 3 \int_0^1 \rho^2 g(\rho) d\rho \quad (4.27)$$

Using Eqs. 4.15 and 4.16, $\frac{N}{\rho_\infty^3} = \frac{N}{R_\infty^3} R_m^3 = \gamma R_m^3 = \mu$

Eq. (4.26) becomes,

$$\bar{\xi} = \frac{\mu \bar{g}}{K} \quad (4.28)$$

Substitution of Eq. (4.28) in Eq. (4.23) after modifying Eq. (4.23) for the average values of $\bar{\xi}$ and D gives

$$\bar{D} = \mu \bar{g} D_c \quad (4.29)$$

Using Eq. (4.29), the average beta dose rate from the feldspar grains can be calculated and compare with measured value. The average beta dose rate from the ^{40}K can be calculated for the sample having k % of K concentration if μ , \bar{g} and D_c are known. These parameters are estimated below for 1 % of K .

Estimation of μ

If R_{\max} is ~ 2.27 mm and the grain size is $100 \mu\text{m}$, then total number of hotspots (μ) can be estimated as 835 from the Eq. (4.1).

Estimation of \bar{g}

\bar{g} can be calculated from Eq. (4.27). To use this equation, the dose distance relationship $g(\rho)$ should be evaluated first. To evaluate this, we need $p(x)$ and $y(x)$, where $p(x)$ is the range spectrum which was obtained from beta energy spectrum of ^{40}K using the range-energy relation. The $p(x)$ has been fitted with six order polynomial and is shown in Fig. 4.2.

The fitted polynomial was,

$$p(x) = 0.80205 + 6.4937x + 25.5158x^2 + 59.9515x^3 + 92.0188x^4 + 70.9606x^5 + 20.6820x^6 \quad (4.30)$$

The range-energy relationship used here is :

$$R = 412 \times E^{1.265 - 0.0954 \ln E} \quad (4.31)$$

This empirical relationship is applicable for the energy region $10 \text{ keV} \leq E \leq 2.5 \text{ MeV}$ (Herman Cember, 1996). After substituting the functional form of $p(x)$ and $y(x)$ in the Eq. (4.12), the dose distance relationship was obtained and plotted in the Fig. 4.3. This relationship was then substituted in Eq. (4.27). The integration of Eq. (4.27) between 0 and 1 gave a \bar{g} value of 1.329.

Estimation of \dot{D}_c

\dot{D}_c is the characteristic dose rate from a hotspot with 14 % of ^{40}K , 3 ppm of U and 10 ppm of Th. In this calculation, only the average beta dose rate from K is considered. The characteristic dose rate can be estimated from the Eq. (4.13), if the activity of the hotspot is known. The calculated specific activity of hotspot is 3700 Bq/kg. The activity of a hotspot is 4×10^{-5} Bq, and this gives a characteristic dose rate of 706 $\mu\text{Gy/ka}$.

Having estimated the values of μ , \bar{g} and \dot{D}_c , the average beta dose rate due to potassium of 1% in the sample is calculated as, $\bar{D} = 835 \times 1.329 \times 706 = 783 \text{ mGy/ka}$. The text book value of beta dose rate due to potassium is 830 mGy/ka (Aitken, 1985). The difference is only less than 6 %, which confirms that the estimated value and the analytical expression derived above are correct.

4.2.3 Solution of dose distribution

In the formulation of the calculations the boundary conditions are included in the Eq. (4.24). Laplace transform method is appropriate for such integral functions. This method comprises, 1) A Laplace transformation of the equation; thus the most transcendental equation becomes less transcendental, 2) a simplification of the arithmetic and 3) Laplace Inversion to get the solution. In this work, the solution was obtained by both numerical and analytical approaches.

4.2.3.1 Numerical Approach

Solution of Eq. (4.24) using Laplace transform was done as follows.

The Laplace transform is,

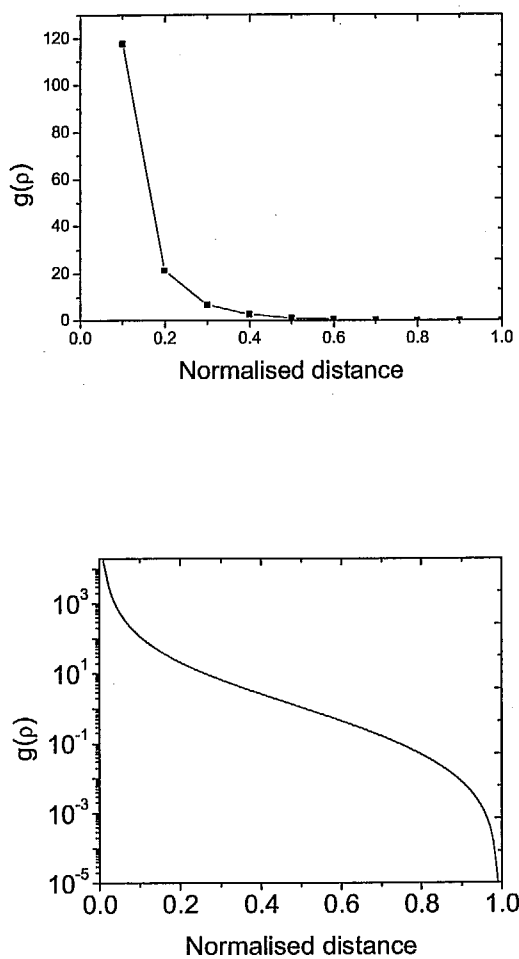


Figure 4.3 Derived dose distance relationship $g(p)$ a) in linear scale and b) in logarithmic scale based on the Eq. (4.12).

$$\phi^*(s) = \int_0^{\infty} e^{-s\xi} \phi(\xi) d\xi \quad (4.32)$$

Eq.(4.24) was substituted in Eq. (4.32) to get the Laplace transformed function in the s variable i.e.,

$$\phi^*(s) = \int_0^{\infty} e^{-s\xi} \left(\int_0^{\rho_{\infty}} \dots \int_0^{\rho_{\infty}} \frac{3\rho_1^2}{\rho_{\infty}^3} \dots \frac{3\rho_N^2}{\rho_{\infty}^3} d\rho_1 \dots d\rho_N \times \delta \left(\xi - \sum_{i=1}^N \frac{g(\rho_i)}{K} \right) \right) d\xi \quad (4.33)$$

$$\phi^*(s) = \int_0^{\rho_{\infty}} \dots \int_0^{\rho_{\infty}} \frac{3\rho_1^2}{\rho_{\infty}^3} \dots \frac{3\rho_N^2}{\rho_{\infty}^3} d\rho_1 \dots d\rho_N \times e^{-s \sum_{i=1}^N \frac{g(\rho_i)}{K}} \quad (4.34)$$

Since each term is identical,

$$\phi^*(s) = \left[\int_0^{\rho_{\infty}} \frac{3\rho^2}{\rho_{\infty}^3} e^{-s \frac{g(\rho)}{K}} d\rho \right]^N \quad (4.35)$$

Since $g(\rho) = 0$ for $\rho > 1$

$$\phi^*(s) = \left[\frac{3}{\rho_{\infty}^3} \int_0^1 \rho^2 e^{-s \frac{g(\rho)}{K}} d\rho + \frac{3}{\rho_{\infty}^3} \int_1^{\rho_{\infty}} \rho^2 d\rho \right]^N \quad (4.36)$$

$$\phi^*(s) = \left[\frac{3}{\rho_{\infty}^3} \int_0^1 \rho^2 e^{-s \frac{g(\rho)}{K}} d\rho + \frac{1}{\rho_{\infty}^3} (\rho_{\infty}^3 - 1) \right]^N \quad (4.37)$$

Let

$$f(s) = 3 \int_0^1 \rho^2 e^{-s \frac{g(\rho)}{K}} d\rho \quad (4.38)$$

$$\phi^*(s) = \left[\frac{f(s)}{\rho_{\infty}^3} + 1 - \frac{1}{\rho_{\infty}^3} \right]^N \quad (4.39)$$

$$\phi^*(s) = \left[1 + \frac{f(s) - 1}{\rho_{\infty}^3} \right]^{\frac{N}{\rho_{\infty}^3} \cdot \rho_{\infty}^3} \quad (4.40)$$

Since $\frac{N}{\rho_{\infty}^3} = \mu$,

$$\phi^*(s) = \left[1 + \frac{f(s) - 1}{\rho_{\infty}^3} \right]^{\mu \cdot \rho_{\infty}^3} \quad (4.41)$$

$$\phi^*(s) = e^{\mu[f(s)-1]} \quad (4.42)$$

From this equation, the actual dose distribution can be obtained by Laplace inversion. As there is no exact mathematical description for this $f(s)$ and $g(\rho)$, the Laplace inversion is not analytically possible and hence the inversion was carried out numerically.

4.2.3.1.1 Numerical Laplace Inversion

Here theoretical framework of numerical inversion is presented. The Laplace transformed function in the scaled variable with the limits 0 to 1 is given as,

$$\phi^*(s) = \int_0^1 e^{-s\xi} f(\xi) d\xi \quad (4.43)$$

Using the Least-Square approximation and Gauss-Quadrature formula, any integral can be written as a summation of orthogonal polynomials with appropriate weight factors. In this work, Gauss-Legendre quadrature formula was used i.e., the orthogonal polynomial used was Legendre Polynomial of degree N (Narayanan & Ramadurai, 1992). According to Hildebrand (Hildebrand, 1987),

$$\int_{-1}^1 f(\xi) d\xi = \sum_{i=1}^N H_i \times f(\xi_i) \quad (4.44)$$

In our work, the limit is not -1 to 1 but 0 to 1. So a linear transformation from ξ to $1-2\xi$ was done and hence we can have the limits from 0 to 1,

$$\int_0^1 f(1-2\xi) d\xi = 2 \sum_{i=1}^N H_i \times f(1-2\xi_i) \quad (4.45)$$

where

$$H_i = \sum_{i=1}^N \frac{4 \times (1 - \xi_i^2)}{(N+1)^2 [P_{N+1}^*(\xi_i)]^2},$$

ξ 's are the zeroes of the shifted Legendre polynomial of degree N.

Now coming to the Laplace transformed function in this work,

$$\phi^*(s) = \int_0^1 e^{-s\xi} f(\xi) d\xi = \sum_{i=1}^N H_i e^{-s\xi_i} f(\xi_i) \quad (4.46)$$

$$\phi^*(s) = \sum_{i=1}^N \frac{4 \times (1 - \xi_i^2)}{(N+1)^2 [P_{N+1}^*(\xi_i)]^2} e^{-s\xi_i} f(\xi_i), \quad s=1,2,\dots,N \quad (4.47)$$

$$\phi^*(s) = \sum_{i=1}^N a_i^s f(\xi_i) \quad s = 1, 2, \dots, N \quad (4.48)$$

Functionally, we have

$$\phi = A f \quad (4.49)$$

and the required function is

$$f = A^{-1} \phi \quad (4.50)$$

The matrix A^{-1} elements were taken from the computed values of 16 digits accuracy by Bellman et al., (1966). The matrix $\phi = e^{-[f(s)-1]}$ is the Laplace transformed function values at particular points of s . The calculations were done in Mathematica 5.1 of Wolfram Research.

To check if Laplace inversion program worked well, a function, whose Laplace transform was known analytically, was used. The function was $f = xe^{-\alpha x}$ and its Laplace transform was $1/(s + \alpha)^2$. Using the above Laplace inversion method this Laplace transform should be inverted to get back the original function. That was done and gave the good results, as shown in the Fig. 4.4.

The Bellman inversion gives only the values of $f(x)$ in a restricted and non-equidistant points. So to get the values at equidistant points, Piessens (1969) extended the Bellman work and gave the relation,

$$\phi(\xi) = \sum_{m=0}^{N-1} C_m P_m^*(e^{-\xi}) \quad (4.51)$$

where

$$C_m = (2m+1) \sum_{j=0}^m a_j^m F(j+1) \text{ and } a_j^m \text{ is the coefficient of } x_j \text{ in } P_m^*(x).$$

To verify this method also, the above known function was used again and the Fig. 4.5 shows that this method also worked well. The Fig. 4.6 shows the results from both the methods (Bellman method and Piessens method) of numerical inversion and the known function.

Having verified the numerical inversion algorithms, we applied this method to estimate the dose distribution. For sample matrix with potassium concentration of 0.5 %, Eq. (4.1) suggests the number of hotspots to be 417. Figure 4.7 shows the completed hotspot dose distribution in single grains of quartz when the sample contains about 0.5 % of K.

4.2.3.1.2 Analytical method

Having obtained the dose distribution by solving the Eq. (4.24) numerically using the dose distance relationship in Eq. (4.12), we now will solve this analytically using Laplace transform method. The dose distance relationship is assumed as given in Eq. (4.52).

$$h(\rho) = \frac{(1-\rho^2)}{\rho^2} \quad (4.52)$$

This dose distance relationship was with the original function $g(\rho)$ and this is given in the Fig. 4.8. This dose distance relationship was used since analytical Laplace inversion is possible when one has an analytical form for the dose distance relationship. The integral equation for the dose distribution function is not exactly like Eq. (4.24) but with small modification in the order of incorporating the positional and number fluctuations in the dose distribution as in Eq. (4.22). And the limit is 0 to 1 instead 0 to ∞ , and the used dose distance relationship is different. So the Laplace transformed function with positional fluctuations is,

$$\phi^*(s) = \int_0^1 3\rho_1^2 d\rho_1 \int_0^1 3\rho_2^2 d\rho_2 \dots \int_0^1 3\rho_N^2 d\rho_N e^{\left(-s \sum_{i=1}^N D_c h(\rho_i)\right)} \quad (4.53)$$

$$\phi^*(s) = \int_0^1 3\rho_1^2 d\rho_1 \int_0^1 3\rho_2^2 d\rho_2 \dots \int_0^1 3\rho_N^2 d\rho_N e^{\left(-s \sum_{i=1}^N D_c h(\rho_i)\right)} \quad (4.54)$$

$$\phi^*(s) = \left(\int_0^1 3\rho^2 d\rho e^{(-s D_c h(\rho))} \right)^N \quad (4.55)$$

where

$$g(s) = \int_0^1 3\rho^2 d\rho e^{(-s D_c h(\rho))} \quad (4.56)$$

By incorporating the number fluctuation governed by Poisson distribution into Eq. (4.55),

$$\phi^*(s) = \sum_{N=0}^{\infty} \frac{\mu^N}{N!} e^{-\mu} (g(s))^N \quad (4.57)$$

$$\phi^*(s) = e^{-\mu} \sum_{N=0}^{\infty} \frac{[\mu g(s)]^N}{N!} \quad (4.58)$$

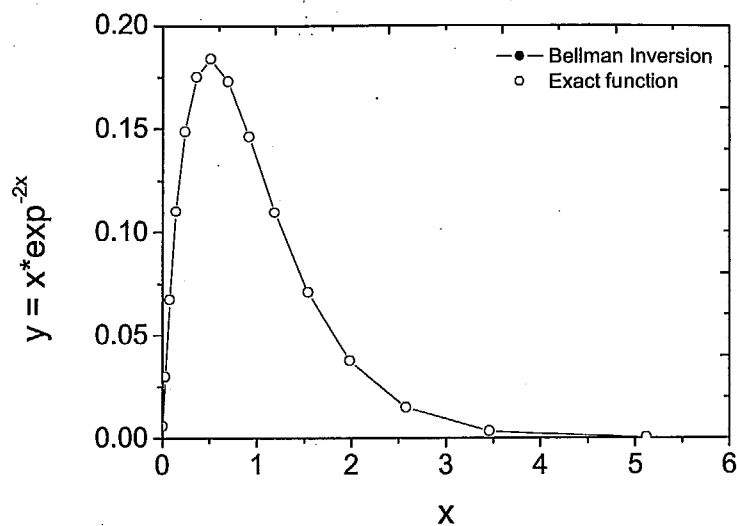


Figure 4.4 Verification of Bellman method of numerical Laplace inversion with the known exact function $x e^{-2x}$.

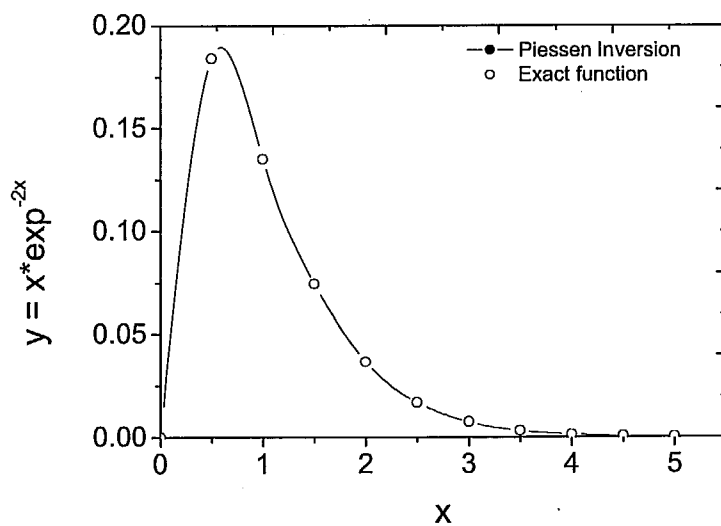


Figure 4.5 Verification of Piessen method of numerical Laplace inversion with the same known function $x e^{-2x}$.

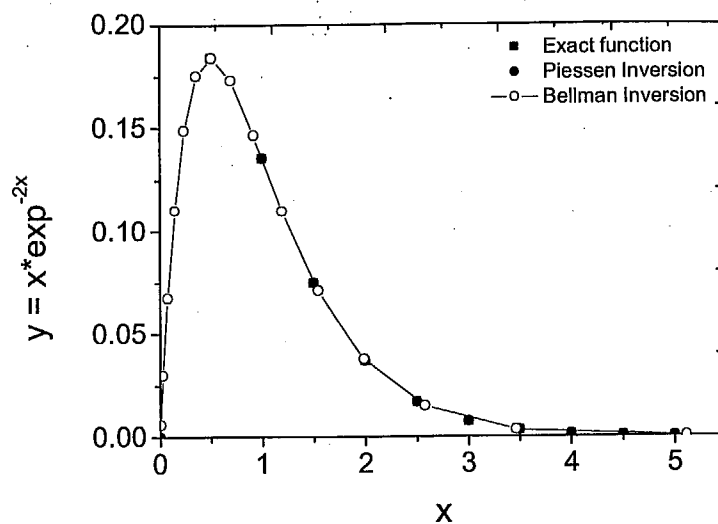


Figure 4.6 Comparison of Bellman and Piessen method of numerical Laplace inversion with the known function $x e^{-2x}$.

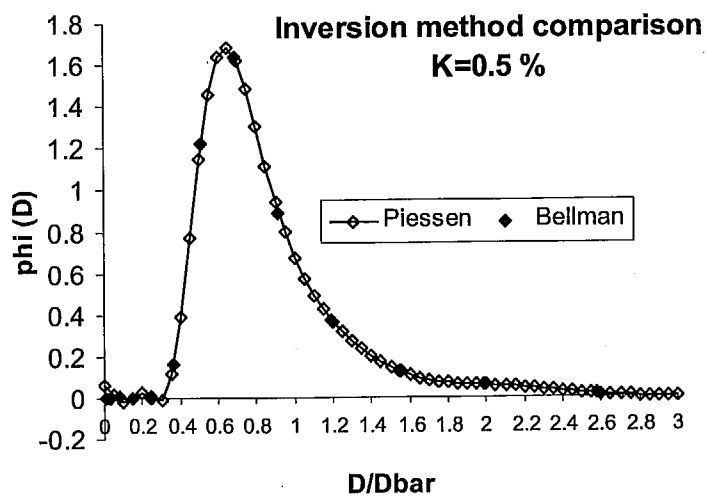


Figure 4.7 Obtained dose distribution function for $K=0.5\%$ by both Bellman and Piessens methods.

$$\phi^*(s) = e^{-\mu} e^{\mu g(s)} \quad (4.59)$$

$$\phi^*(s) = e^{\mu[g(s)-1]} \quad (4.60)$$

The solution to Laplace transformed function may be obtained by Laplace inversion formalism. Formally, the Laplace inversion is

$$\phi(D) = \left(\frac{1}{2\pi i} \right) \int_{c-i\infty}^{c+i\infty} \exp[sD] \phi^*(s) ds \quad (4.61)$$

where, the integration is carried out with respect to s in the complex s -plane along a line parallel to the imaginary axis lying to the right of all the singularities of $\phi^*(s)$. Explicitly

$$\phi(D) = \left(\frac{1}{2\pi i} \right) \int_{c-i\infty}^{c+i\infty} \exp[sD] \exp[\mu(g(s)-1)] ds \quad (4.62)$$

For mathematical convenience, we replace the variable s by q , where

$$q = sD_c \quad (4.63)$$

This makes it easy to seek the distribution of the relative dose, D/D_c ,

$$\phi\left(\frac{D}{D_c}\right) = \left(\frac{1}{2\pi i} \right) \int_{c-i\infty}^{c+i\infty} \exp[qD/D] \exp[\mu(g(q)-1)] dq \quad (4.64)$$

Considering a one-group case, and substituting Eq. (4.52) in Eq. (4.56), we have the g -function

$$g(q) = 3 \int_0^1 \rho^2 \exp[-q(1-\rho^2)/\rho^2] \rho^2 d\rho \quad (4.65)$$

Let us define a new variable of integration

$$x = (1-\rho^2)/\rho^2 \quad (0 < \rho < 1) \quad (4.66)$$

x is a monotonic function of ρ . As ρ varies from 0 to 1, x monotonically decreases from ∞ to 0. Hence we may justifiably use the monotonic inverse

$$\rho = 1/(1+x)^{(1/2)} \quad (0 < x < \infty) \quad (4.67)$$

for replacing the $\rho^2 d\rho$ term in terms of x variable and dx in the integrand of Eq. (4.65). With this the integral in Eq. (4.65) is

$$g(q) = \left(\frac{3}{2} \right) \int_0^\infty \exp[-qx] [1+x]^{-5/2} dx \quad (4.68)$$

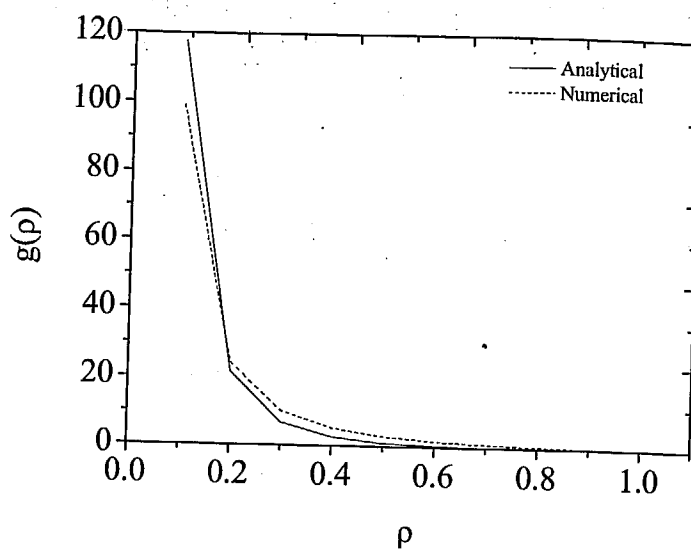


Figure 4.8 Dose distance relationship used for analytical [Eq. (4.52)] and numerical [Eq. (4.12)] approaches.

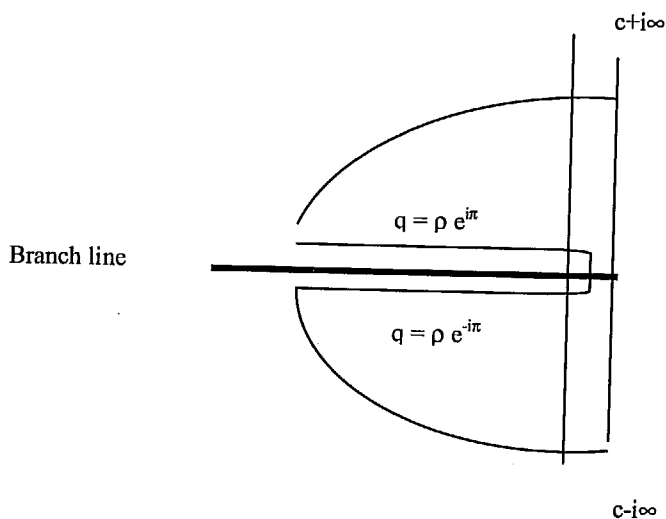


Figure 4.9 Appropriate Integration contour.

It may be readily evaluated as:

$$g(q) = 1 + 2 \left[\pi^{1/2} q^{3/2} \exp(q) - \pi^{1/2} q^{3/2} \exp(q) \operatorname{erf}(q^{1/2}) - q \right] \quad (4.69)$$

Upon substituting in Eq. (4.64), we have

$$\phi(D/D_c) = (1/2\pi i) \int_{c-i\infty}^{c+i\infty} \exp \left[(qD/D_c) + 2\mu \left[\pi^{1/2} q^{3/2} \exp(q) \operatorname{erf}(q^{1/2}) - q \right] \right] dq \quad (4.70)$$

where, $\operatorname{erf}(z)$ is the well-known error function [$\operatorname{erf}(0)=0$, $\operatorname{erf}(\infty)=1$]. From its properties in the complex plane, the following may be inferred. (i) The integrand is bounded in the left half of the q -plane, which is assuring since otherwise $\phi(D/D_c)$ would not exist (since D/D_c is a positive quantity). (ii) The integrand has a branch point at $q=0$ with branch cut extending from $-\infty$ to 0. (iii) It has no other singularities. With these, one may reduce the integral in terms of a real variable ρ by constructing a contour as shown below in Fig 4.9.

The integration on the line $(c-i\infty, c+i\infty)$ turns out to be a sum of integrals along lines $q = \rho \exp(i\pi)$ and $q = \rho \exp(-i\pi)$. Explicit integration also requires the following properties of $\operatorname{erf}(ix)$:

$$\operatorname{erf}(ix) = \pm i \operatorname{erfi}(x) \quad (4.71)$$

where, $\operatorname{erfi}(x)$ is a real function for x real. With these, the solution is

$$\phi(D/D_c) = (1/\pi) \int_{c-i\infty}^{c+i\infty} \exp \left[(\rho D/D_c) + 2\mu \left\{ \rho - \pi^{1/2} \rho^{3/2} \exp(-\rho) \operatorname{erfi}(\rho^{1/2}) \right\} \right] \sin \left\{ 2\mu \pi^{1/2} \rho^{3/2} \exp(-\rho) \right\} d\rho \quad (4.72)$$

This cannot be reduced any further. However, being a one parameter integral it may be evaluated numerically through integration software as a function of D/D_c . Here, just to compare the results with the numerical approach, the variable was scaled from D/D_c to $\xi (= D/\bar{D}_c)$. For the analytical approach the calculated \bar{g} is 2. The dose distribution thus obtained by analytical method by considering the assumed dose distance relationship is given in the Fig 4.10. For large μ , the highly oscillatory nature

of the integrals gives rise to artificial convergence problems. For comparison, the Fig 4.11 shows that the dose distributions obtained by analytical and numerical approaches are comparable.

Results from this analytical method could not be used for further calculation as the $h(\rho)$ is not equal to $g(\rho)$. The exercise was to verify the numerical approach.

4.2.4 Results and Discussion

In this section also the results obtained by numerical method are discussed. To use the numerical Laplace inversion algorithm, one should know that Laplace transform was stable under perturbation, but this is not true for Laplace inversion. So by a small change in $\phi^*(s)$, a rapid oscillatory behavior can be seen in $\phi(\xi)$. By calculating $\phi^*(s)$ and the matrix elements of A with accurate values, the oscillatory behavior can be minimized. It is not possible to filter extremely rapid oscillations of $\phi(\xi)$ using numerical values $\phi^*(s)$ alone, In the Fig. 4.12, where the low dose part has oscillations of high frequency and the higher dose side has low frequency. But the interesting part is the low dose part and is discussed in Chapter 5. The obtained dose distribution function can be fitted to a modified Gumbel distribution (with a slightly modified shape parameter, w). The Gumbel distribution is

$$\phi(\xi) = a \exp \left[-\exp \left(-\left(\frac{\xi - \xi_c}{w} \right) \right) - \left(\frac{\xi - \xi_c}{w} \right) \right] \quad (4.73)$$

The modified Gumbel distribution is used to fit the data and is given as,

$$\phi(\xi) = a \exp \left[-\exp \left(-\left(\frac{\xi - \xi_c}{w_1} \right) \right) - \left(\frac{\xi - \xi_c}{w_2} \right) \right] \quad (4.74)$$

The Fig. 4.12 shows the fitted modified Gumbel distribution function and the actual data. This is a mathematical fit only and no physical process is implied in this fitting. In order to calculate the dose distributions for different K concentrations, we repeated the numerical inversion for each K value. As earlier, the Piessens method of Laplace inversion was used give dose distribution for K values of 0.1, 0.3, 0.5, 1, 1.5, 2 % concentrations in the sample. The results are shown in the Fig 4.13.

By analyzing the dose distribution curves, the low dose and the peak dose had a good relationship with the K concentration. Since we are interested in the low dose part, the relationship between the low dose and the corresponding K concentration was plotted in the Fig 4.14. This relationship had a saturating exponential form as below,

$$p = 0.46[1 - \exp(-2.2 \times K)] \quad (4.75)$$

The significance of this factor has been explained in the next chapter.

The factor 'p' should be 1 when the K concentration increases and attains a maximum. This is because, the greater the concentration of K, the higher the number of hotspots, and hence higher the overlap of the spheres of influence. So all the grains will receive the average dose. This implies that p should be 1 as p is nothing but lowest ξ ($= D/\bar{D}$; \bar{D} is the mean dose). In this model, the volume fraction of hotspots is only 25 % in the sample matrix. If the number of hotspots is increased, then the influential spheres of the neighbors' start overlap with each other. In that case, the excluded volume corrections should be made.

It is worth noting that there occurs a decreasing trend of RSD with respect to the number of hotspots. The decrease is rapid for K concentrations up to 1%. This occurs for the reason discussed above. In the ^{40}K beta dose distribution we did not observe any grains with a zero dose. This suggests that each and every grain in the matrix receives some finite dose from the hotspots. Similarly, we couldn't find any maximum concentration of K after which the RSD does not decrease any further, i.e. the hotspot distribution and the resulting beta dose can not be considered homogeneous for any realistic concentration of K. The results are shown in Fig 4.15.

4.3 Summary

The beta dose distribution in individual quartz grains arising from ^{40}K hotspots was obtained. This has been fitted with modified Gumbel distribution function. The minimum dose and the peak dose are shifted to higher values with an increase in the K concentration. As this model doesn't consider the excluded volume effect which implies that, for the K concentration of more than 2 % this model may not work well. The implications of this study will be discussed in detail in Chapter 5.

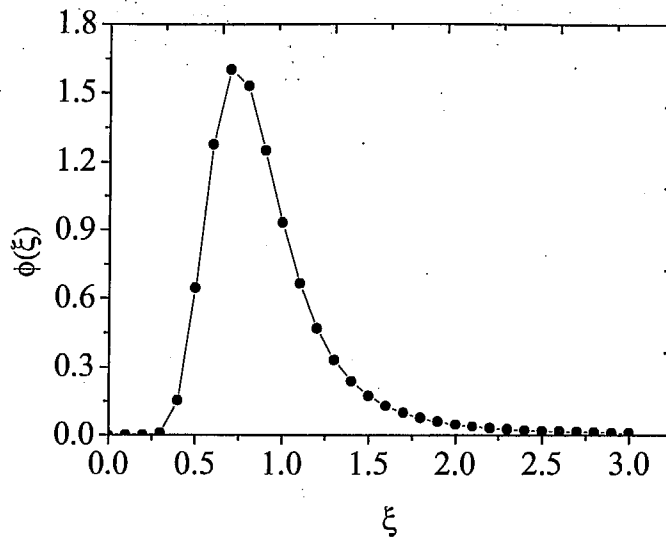


Figure 4.10 The dose distribution obtained by analytical approach for number of hotspots (μ) of 84.

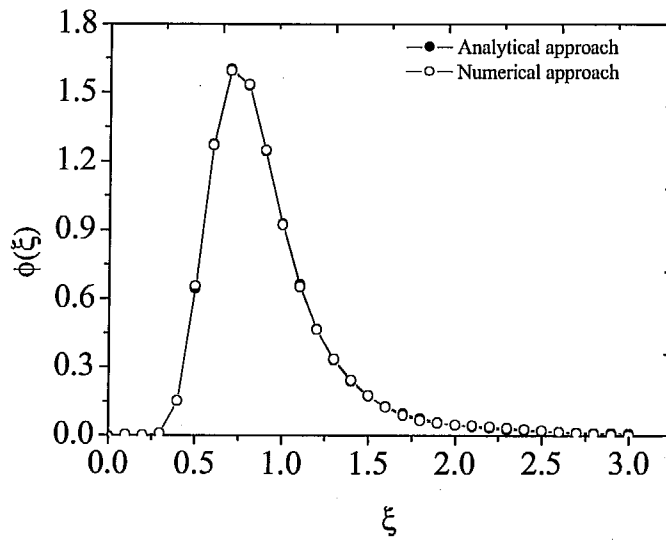


Figure 4.11 Comparison of dose distribution by analytical and numerical approaches for number of hotspots (μ) of 84.

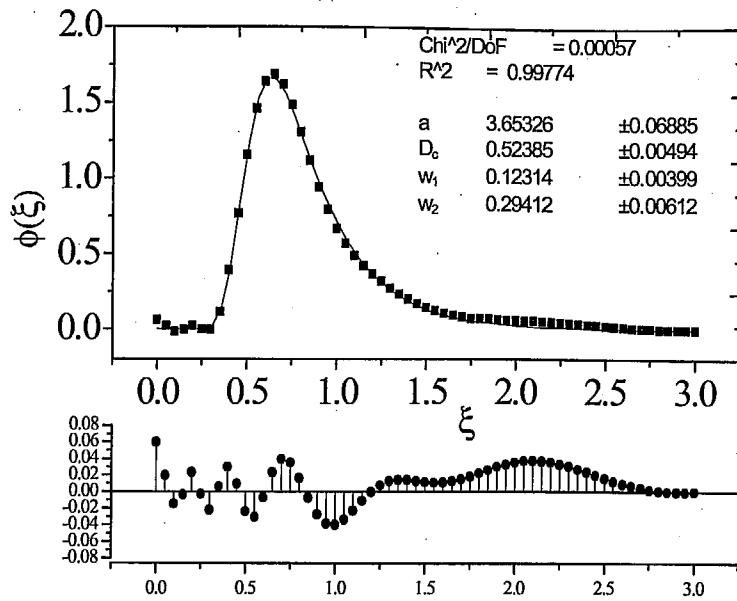


Figure 4.12 Dose distribution and fitting to modified Gumbel distribution given in Eq. (4.74).

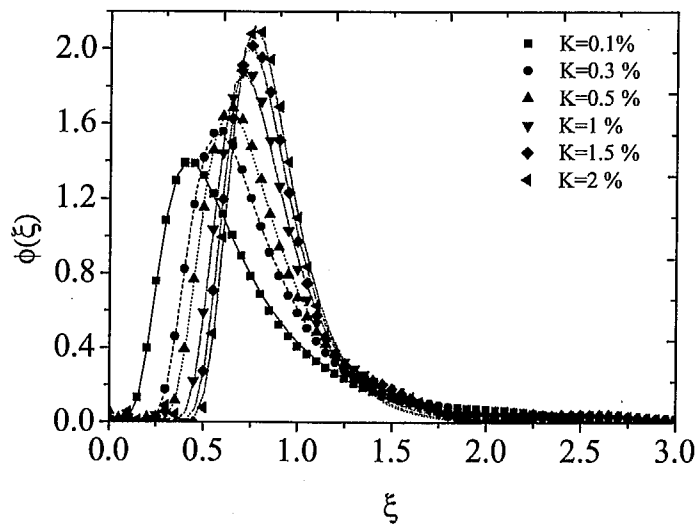


Figure 4.13 Dose distribution results for various K values.

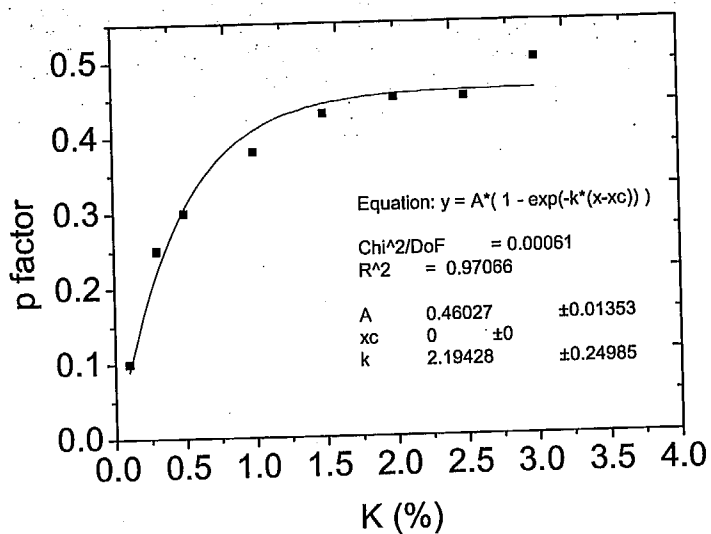


Figure 4.14 Exponential saturation of the 'p' factor with increasing K concentration following the empirical functional form given in Eq. (4.75).

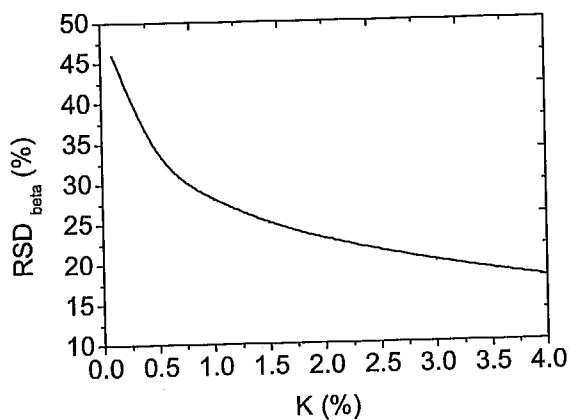


Figure 4.15 Decreasing of RSD with increasing K concentration.

Implication of spatial heterogeneity of beta dose in Sediments

5.1 Introduction

The implications of beta dose heterogeneity concept developed in Chapter 4 are discussed here. Computed dose distributions in scaled dose and in real dose are shown in Fig 5.1(a) and (b). The distribution here is computed for randomly distributed hotspots comprising 3 ppm U, 10 ppm Th and 14 % K. However, as the main source of U and Th is clay size fraction, it can reasonably be assumed that the beta dose rate from U and Th in a sediment matrix, is approximately uniform. The main carrier phase of K is K-feldspar and with upto 14% K. This implies that the dose rate from K can be expected to be non uniform depending upon the concentration of feldspar hotspots in the sediments. Modeling results suggest that for K of less than 2% by weight in the sediment would lead to a large distribution of beta doses delivered to individual quartz grains in a sediment matrix.

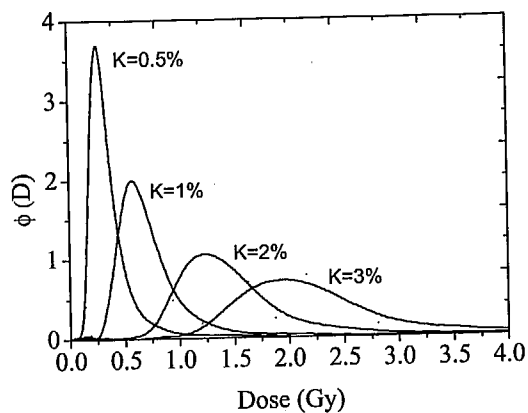
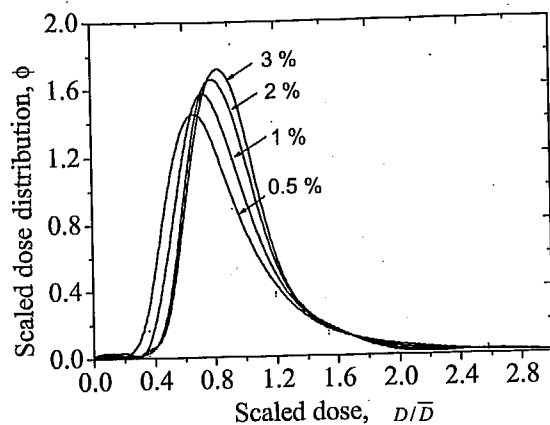


Figure 5.1

- a) The burial dose distribution arising because of the K hotspots in the sample matrix shown in scaled dose and b) in real dose. Here D is the dose, \bar{D} is the mean dose and $\Phi(D)$ is the dose distribution.

As discussed in Chapter 4, such a dose distribution can be described adequately by a modified Gumbel function as the nature of this distribution remains the same irrespective of the total absorbed dose. Thus, it can be generalized that at any time after the burial, the dose distribution function will be a modified Gumbel function with the assumption that the main source of this dose distribution is the beta dose heterogeneity arising from ^{40}K . It can also be reasonably assumed that the gamma dose and the beta dose from U and Th are single valued (uniform) as these are not exclusively associated with the hotspots only.

In a real dating situation, especially of partially bleached sediments additional difficulties arise from dose distribution arising due to partial and heterogeneous bleaching. There are several methods that have been used (Section 1.6.1) to determine the true burial dose from such a dose distribution arising exclusively due to partial and heterogeneous bleaching. We consider that the dose distribution in any sediment is due to the combined influence of two factors, viz., beta heterogeneity and partial bleaching, and methodology to cope with such situations is discussed below.

5.2 Influence of partial bleaching on dose distribution

The bleaching of dose from a single grain is a random event, analogous to a spontaneous radioactive disintegration of an atomic nucleus. During transportation, there is a finite probability that a portion of sediment gets a daylight exposure, and loses its luminescence (i.e., dose). If it is assumed that individual grains in this portion are randomly exposed to daylight such that the average dose in a randomly chosen sub-set from this sediment is not zero at any time. Thus at the time of deposition (burial, $t=0$), a dose distribution in the sediment grain exists. The nature of this distribution depends on daylight bleaching during transport.

The nature of dose distribution from partially bleached sediments can be experimentally verified. The single-grain dose distributions from an aeolian sand (Bush and Feathers, 2003) and modern fluvial sands (Jain, 2007) are plotted in Figs. 5.2-5.3. In these measurements all the negative dose values in the distributions are assigned a zero dose, as negative dose values are only an experimental artifact and cannot exist, as such.

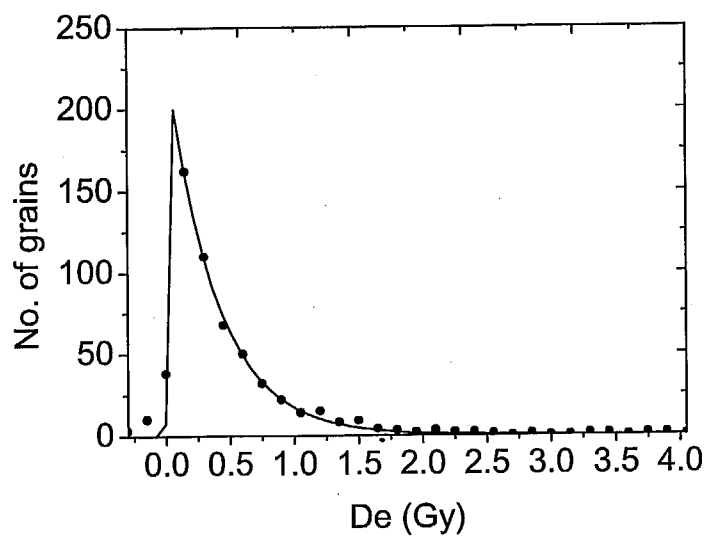


Figure 5.2 Palaeodose distribution in modern surface samples from Aeolian contexts. (redrawn from Bush and Feathers, 2003). The distribution has been fitted to an exponential decay function.

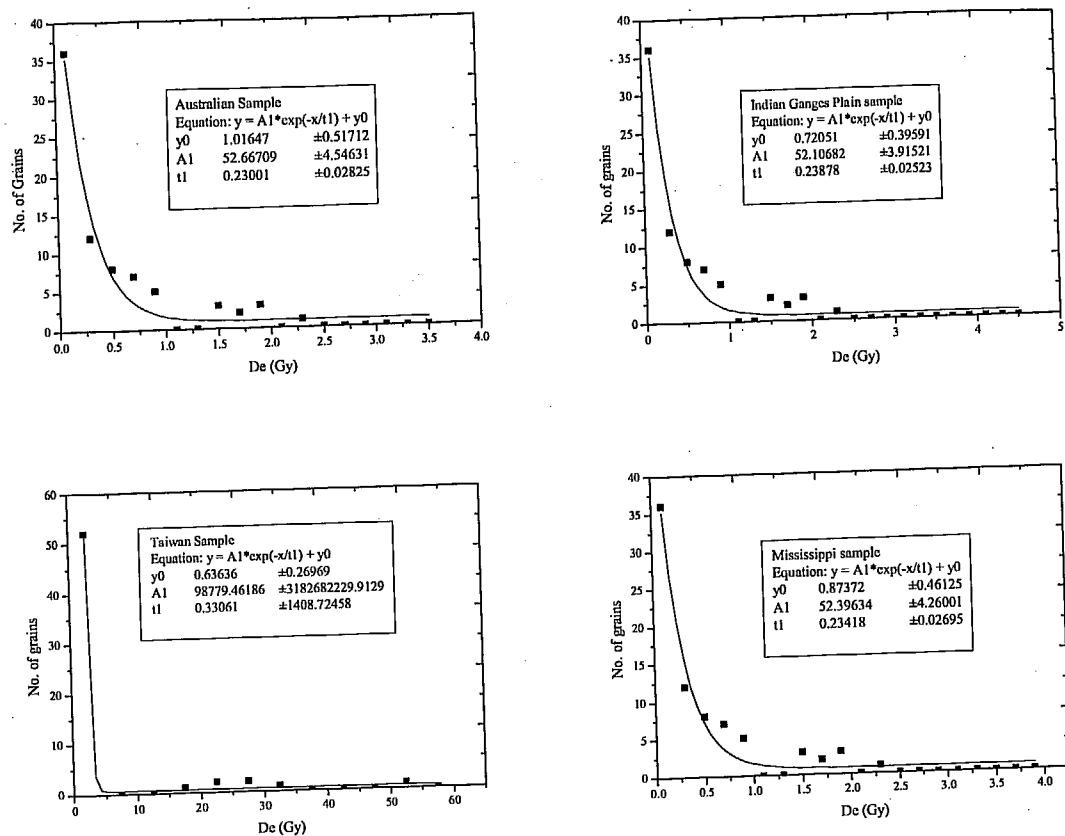


Figure 5.3 Palaeodose distribution in modern surface samples from Fluvial contexts. (redrawn from M. Jain, 2007). All the dose distributions are fitted to an exponential decay function.

Irrespective of average dose in the sample and the origin of deposit, single-grain dose distributions can be approximated to an exponential decay. This dose distribution is a negative exponential as majority of grains have zero dose and frequency of non zero dose reduces exponentially. This leads to a reasonable conclusion that the starting dose distribution (at the time of burial i.e. $t = 0$) of sediment is a negative exponential. After burial the sediment grains with such a dose distributions, begin to accrue their burial dose due to the ambient radioactivity.

From the model developed in previous chapter it was seen that, the burial dose distribution can be mathematically described by modified Gumbel distribution. The measured dose distribution of buried sediment therefore will be a composite of distribution arising from the convolution of negative exponential function and the modified Gumbel function. If all the grains were well bleached, the partially bleached dose distribution will simply be a Dirac delta function at zero dose and hence no change in the convoluted (i.e., total) dose distribution would occur.

However, in case of partial, heterogeneously bleached sediments, the convoluted distribution will have a shape depending on the shape of the dose distribution of partially bleached sediments at $t = 0$, compounded by the dose rate distribution due to K . The equation for convolution can be expressed as,

$$\phi_m(D) = \phi_b(D) \otimes \phi_{pb}(D) \quad (5.1)$$

$$\phi_m(D) = \int_{-\infty}^{\infty} \phi_b(u) \phi_{pb}(u-D) du \quad (5.2)$$

where $\phi_m(D)$ is the measured dose distribution,

$\phi_b(D)$ is the burial dose distribution due to beta dose heterogeneity, and

$\phi_{pb}(D)$ is the partially bleached dose distribution, u is a dummy variable representing D , the dose.

Thus,

$$\phi_{pb}(D) = X^{-1} \exp\left[-\frac{D}{X}\right]; D \geq 0 \quad (5.3)$$

where X ($= \% \text{ of } \bar{D}$) is the mean unbleached dose (Fig. 5.4).

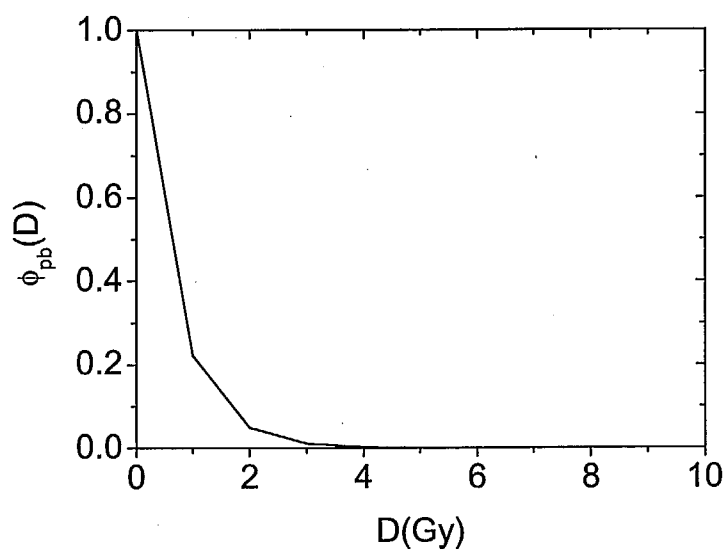


Figure 5.4 Assumed truncated negative exponential distribution of the partially bleached dose with the normalized mean value.

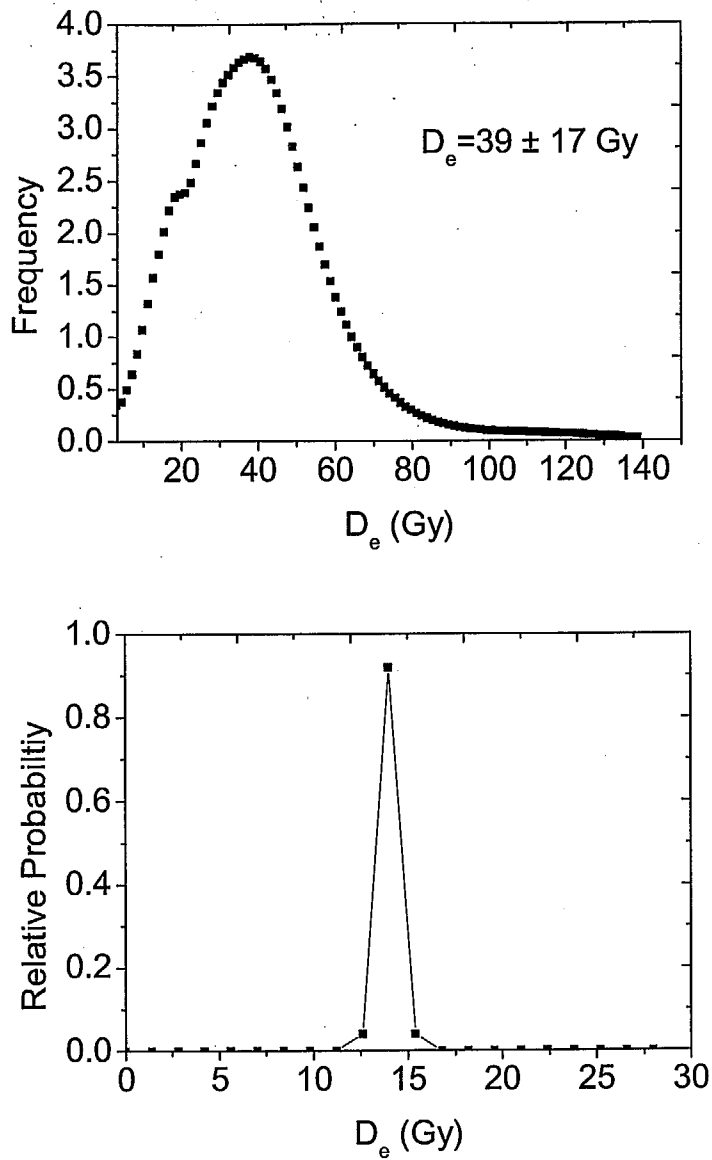


Figure 5.5

a) Measured dose distribution of well bleached sample,

b) Experimental error distribution obtained from the dose recovery experiment for an administered dose ~ 12 Gy.

One can generalize that the measured dose distribution is convolution of the true dose distribution $\phi(Db)$ and experimental error distribution. This can be seen in measured data of equivalent dose (Fig. 5.5.a) and error calculated from a dose recovery experiment (Fig. 5.5.b). The uncertainty introduced by the instrument is typically $\sim 4\%$. Using this uncertainty a deconvolution of the measured distribution was carried out. It was however observed that there is no significant difference between the original (convoluted) and the deconvoluted dose distributions (Fig. 5.6). Therefore, the experimental uncertainty was not considered any further.

Figs. 5.7 (a-d) were constructed by convoluting a partial bleached dose distribution at the time of burial with the Gumbel dose distribution given to the sample by beta irradiation from the hotspots during the burial period. A simulated dose distribution at the time of burial was used. This distribution was derived using the equation of a negative exponential as shown in Eq. 5.3.

Four partial bleaching scenarios were considered with mean dose at the time of burial equal to 90 %, 70 %, 40 % or 10 % of the original dose. It was observed that the shape of the distributions are quite different, and so are the mean doses; the poorer the bleaching, higher the mean dose. However, in all the cases, the least dose remained exactly same, irrespective of the extent of partial bleaching. This implied that a correct value of burial dose can be estimated from the least dose in a measured dose distribution. However, this can be used only if the dose rate, relevant for lower dose part of distribution is known. This is discussed below.

5.3 Age Equation

The luminescence age is given by the relation,

$$Age = \frac{D}{\dot{D}} \quad (5.4)$$

In both single aliquot or single grains procedures, in general, for well bleached samples, the mean values for both dose and dose rate are used. In case it is observed that the dose distribution is suggestive of partial bleaching, then a minimum dose is derived from the equivalent dose distribution but the dose rate is based on the total dose rate derived from K, U and Th. This is because till the present thesis the heterogeneous distribution of dose rate was so far not been even considered.

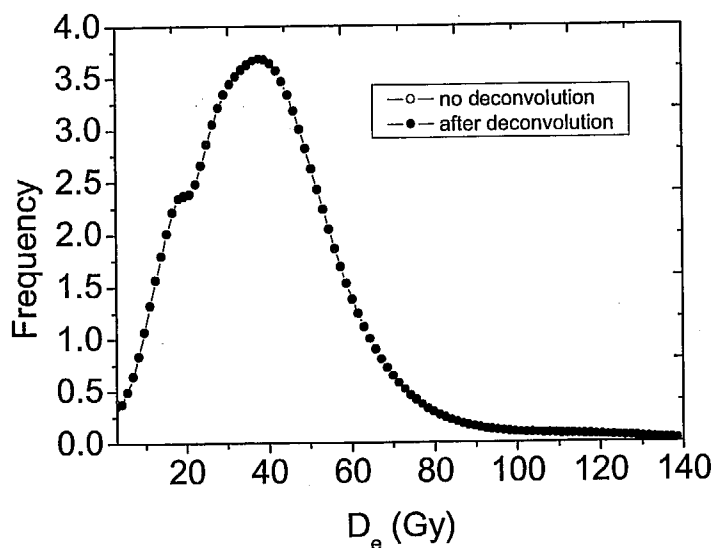


Figure 5.6 Resulting dose distribution after deconvoluting the experimental error distribution (Fig. 5.5b) from the measured distribution (Fig. 5.5a) dose distribution. There is no effect in deconvoluting the experimental error distribution from the measured dose distribution and that is seen in the indistinguishableness of the two curves. See text for the details.

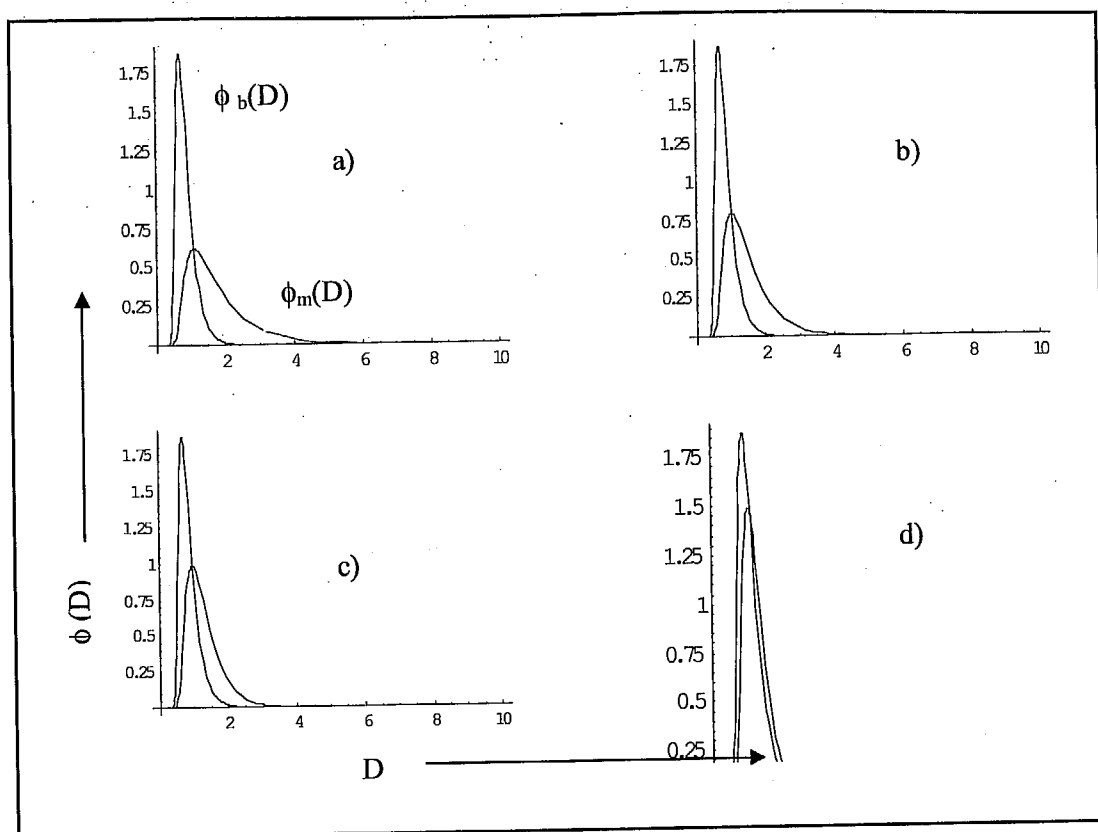


Figure 5.7 Graphs showing the burial dose distribution and the convoluted distribution with the truncated exponential (partial bleached) distribution. a) 90 % dose unbleached b) 70 % of dose c) 30 % of dose and d) 10 % of dose was unbleached.

As discussed below, the dose rate should be modified accordingly to suite the low end dose, i.e., we suggest that the age be calculated using the relation,

$$Age = \frac{D_{\min}}{\dot{D}_{\min}} \quad (5.5)$$

where, the numerator D_{\min} is,

$$D_{\min} = (\dot{D}_{\min, \text{Uniform}} + \dot{D}_{\min, K}) Age \quad (5.6)$$

In the above equation, dose rate is categorized into two namely, the uniform dose rate and the hotspot (K) dose rate. As the uniform dose rate is a constant value for entire dose distribution, i.e.,

$$\dot{D}_{\min, \text{Uniform}} = \dot{D}_{\text{Uniform}} \quad (5.7)$$

The minimum hotspot dose rate can be obtained using the 'p' factor (Section 4.2.4) by using relation,

$$\dot{D}_{\min, K} = p \dot{D}_K \quad (5.8)$$

So,

$$D_{\min} = (\dot{D}_{\text{Uniform}} + p \dot{D}_K) Age \quad (5.9)$$

If 'f' be the proportion of uniform dose rate then '1-f' will be the proportion of hotspot dose rate.

$$D_{\min} = (f \bar{\dot{D}} + p(1-f) \bar{\dot{D}}) Age \quad (5.10)$$

$$D_{\min} = ([f + p(1-f)] \bar{\dot{D}}) Age \quad (5.11)$$

$$Age = \frac{D_{\min}}{([f + p(1-f)] \bar{\dot{D}})} \quad (5.12)$$

This is the most general age equation that can be used for any sample that experiences both the heterogeneous bleaching and dose heterogeneity.

5.3.1 Dose

Based on discussions so far, in the new Age equation, the minimum dose is parameter of relevance. Results of convolution suggest that, the most robust estimate of burial dose is the minimum dose; this estimate is independent of the degree of partial bleaching and of dose rate distribution. From the beta dose rate modeling, the minimum dose is defined as the dose at which probability density function becomes zero. There are two main considerations for selecting the minimum dose from experimentally measured dose distribution data.

Minimum dose in the simulated single-grain dose distribution

During the development of the analytical model, we followed Laplace Transform to solve the integro-differential equation. While Laplace transform is stable under small changes in variables, the Laplace Inversion is not. Additionally Laplace Inversion was done numerically using approximated Legendre Polynomial. This problem, conventionally termed as an 'ill posed problem', and the above difficulties cause oscillations in the lower dose and higher dose side (Fig. 5.8.a).

The oscillations on higher dose side are not of much concern for our dose estimation problem. However desirable dose estimate lies in the lower side of the dose distribution, which can be seen in Fig. 5.8 a, b the oscillations are quite significant and centered at zero probability. Because of these oscillations, it is difficult to define exactly where this probability distribution function attains a zero value. Therefore, mathematically the minimum dose is an approximation based on a smoothened data.

Minimum dose in the measured single-grain dose distribution

The main issue here is the accuracy of minimum dose estimate from a measured dose distribution, since this is the key parameter for age calculation. During the measurement of D_e using the SAR procedure, the sensitivity of sample due to preheat, stimulation and irradiation is corrected by using the test dose OSL signal. It has been generally considered that sensitivity of the sample in natural environment (i.e., natural sensitivity) and that in laboratory environment is more or less same (Shlukov et al., 2001; Wallinga et al., 2000). If these sensitivities are different then the way the SAR procedure is used may not be totally right. During the first OSL measurement due to

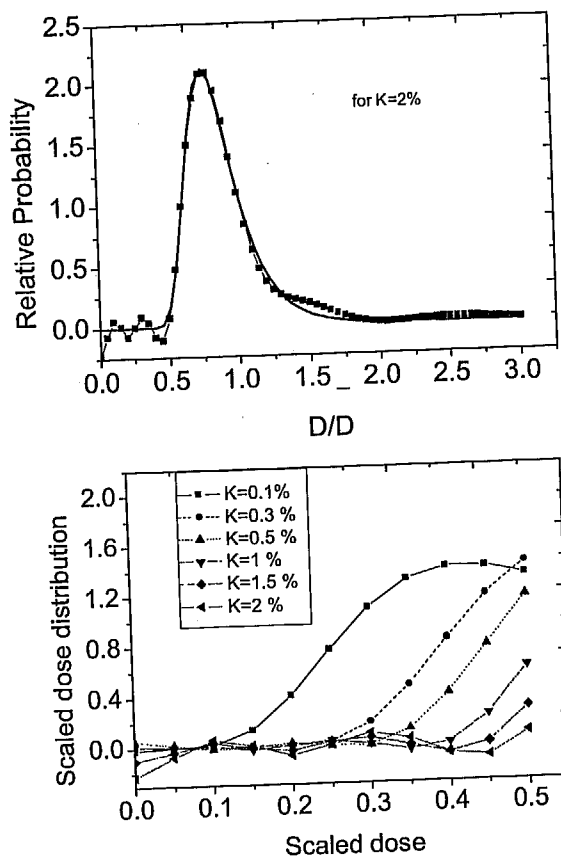


Figure 5.8

- a) The burial dose distribution arises from the 0.5 % of K concentration present in the sample. The oscillations in the lower dose side and in higher dose side are clearly seen and it is attributed to small variations in the values used in the numerical approach for the Laplace Inversion and
- b) the lower dose side is zoomed in so that the nature of oscillations could be noticed.

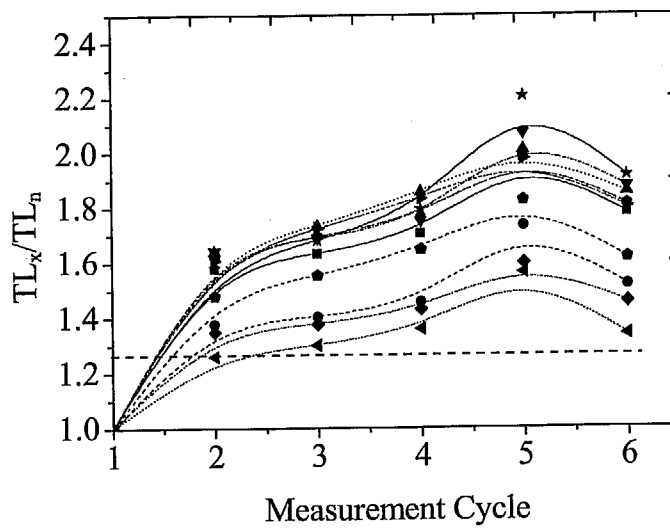


Figure 5.9 Sensitivity changes with many measurements. Dashed line show the 30 % increase in sensitivity after the first measurement.

the stimulation, preheat and irradiation, the sensitivity may be changed. The subsequent test dose signal T_n is measured entirely in laboratory environment. So T_n may not be a correct measure of the sensitivity of L_n . The rest of the points (R1, R2, R3, R4 and R5) in dose response curve are of no problem as they are all induced entirely in laboratory. The magnitude of sensitivity change during the L_n measurement can be up to 30 % (Fig 5.9). On an average it has been observed that in single aliquot measurement, the natural sensitivity change is $\sim 5\%$. Since NCF (Chapter 2, Singhvi and Stokes, Pers. Comm.) approach is based on the measurement of 110°C TL peak, it can not be applied to a single grain measurement protocol using a Risø system. This is because a grain placed in a sample holder of 100 grains cannot be heated individually. Therefore, an uncertainty of 5% arising from natural sensitivity change was used in all the dose estimates in this study. In addition to these problems, it has been shown that there is a random uncertainty of 10% in all the single grain measurements of quartz heated calibration quartz (Thomsen et al., 2005); the causes of this uncertainty are not known. This implies that the total uncertainty in a natural sample would be a sum (in quadrature) of above two uncertainties and equal to about 11.2%.

Because of these above two issues, namely the low dose oscillations and the accuracy of dose measurement, it is likely that the estimated p value and the minimum dose estimate will have some deviation from their true values. It is worth noting that p value is required for estimation of the dose rate applicable to the low dose part of the distribution. To tackle this issue it was preferred to use an average of the minimum dose population comprising 5% of the total grains instead of using the single estimate of least measured dose. It has been shown that 5% estimation is also a good approximation of the true dose in partially bleached samples (Olley et al., 1998; Jain et al., 2004; Bailey and Arnold, 2006).

As 5 % of the lowest dose points are considered for age estimation, statistically there should be enough number of data points in that region. An adequate number has been calculated as 117 grains (Vermeesch, 2004) in a work focused mainly on detrital provenance study using single-grain geochronometry. Vermeesch (2004) attempted estimation of the minimum number of grains in a sample that must be analyzed to achieve a required level of statistical adequacy. The author concluded that at least 117 grains should be dated if it is desired that number fraction of the population, comprising more than 0.05 of the total, is missed at the 95 % confidence level. This is

to say that the estimated ages are correct at a confidence level, It is recommended that if lesser number of grains were used then the confidence level reduced thereby leading to higher error in D_e . In the single grain luminescence analysis, typically only 5-10 % grains fill the criteria for SAR analysis, it implies that the total number of grains to be used is >1170 if 117 dose estimates are needed for analysis. Since it is usually impractical to measure such high number of grains, but if this is not done then the low dose side of the distribution will not be known very well.

5.3.2 Dose Rate

The total dose rate to a quartz grain comprises the uniform dose and a spatially variable (hotspot) dose rate. Uniform dose comprises gamma dose from U, Th and K, and the beta dose from U and Th and the cosmic ray dose. Heterogeneous dose rate is beta dose rate from the K. Empirically, the average radioactivity in sediment samples in this study (i.e., ^{238}U , ^{232}Th and ^{40}K values of about 3 ppm, 10 ppm and 2 % respectively) gives a uniform dose rate which is about 44 % of total dose rate. The heterogeneous dose rate arising from K is about 56 %. Recently, the actual radionuclide concentration was calculated by using 3758 samples (Ankjægård et al., 2006). This is the total number of samples processed in Risø National Laboratory, Denmark for 10 years. The result is given in table (Table 5.1) as well as in Fig 5. 10. By using the mode value of the U, Th and K from the above table, the uniform and heterogeneous components of dose-rates are calculated to be 37 % and 63 % respectively. The calculated values of fraction of uniform and hotspot dose rate from our samples are also consistent with this data within error limits. The value of the 'p' factor for particular K concentration can be obtained from Eq. 4.75 of Section 4.2.4 (Chapter 4).

To test the forgoing formulation, we examined the single grain dose distribution from Murray and Roberts, (1997) (Fig. 5.11). In this dose distribution, two dose peaks (modal values) are at 23.4 Gy and 35.6 Gy respectively. The dose rates were calculated from values given in Roberts, et al., (1996). Murray and Roberts (1997) used an average value for dose rate and obtained an age of 9.8 ka. Their bin-width was 2.05 Gy. The choice of this bin-width was arbitrary and as there is no a-priori

Table 5.1 Natural radioactive nuclide concentration of 3758 samples (from Ankjægård et al., 2006).

| | ^{238}U | ^{232}Th | ^{40}K |
|--------------------------------------|------------------|-------------------|-----------------|
| Mode, Bq.kg^{-1} | 8 | 4 | 355 |
| Median, Bq.kg^{-1} | 15.30 | 15.34 | 406 |
| 0.01 percentile, Bq.kg^{-1} | 0.20 | 2.84 | 40 |
| 0.99 percentile, Bq.kg^{-1} | 90.37 | 150.4 | 1182 |

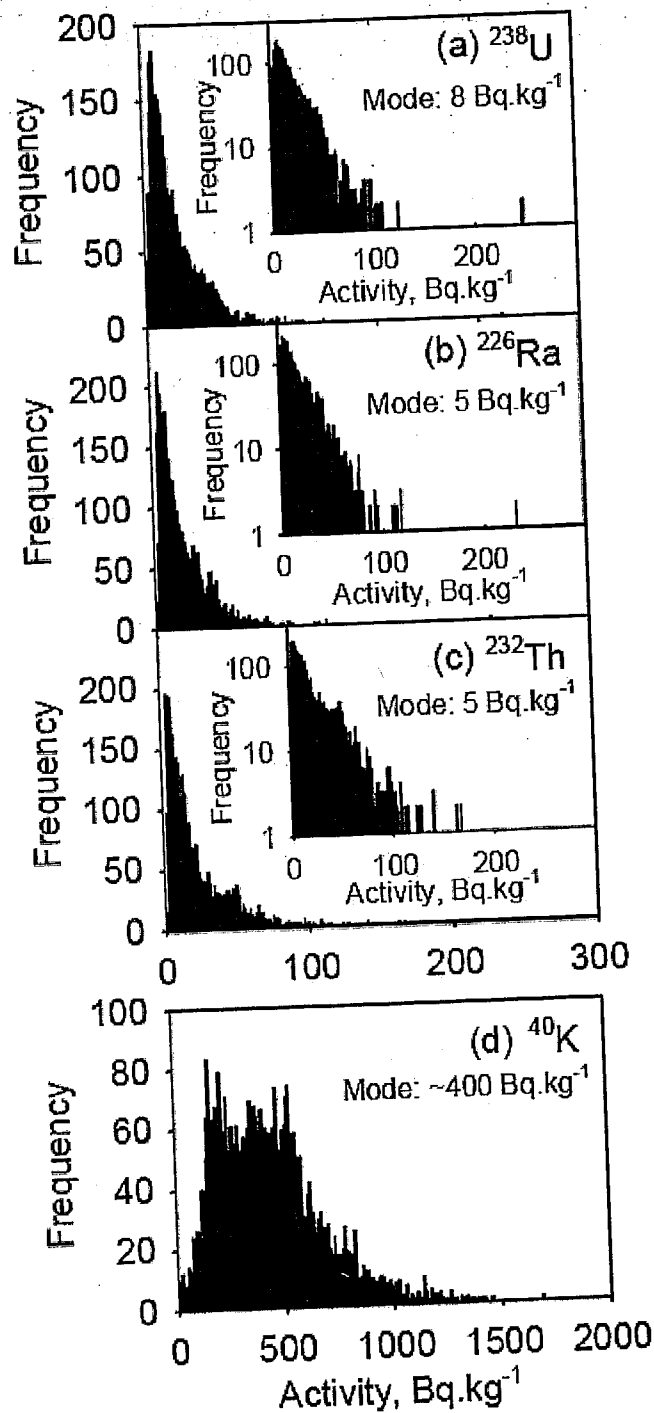


Figure 5.10 Natural radioactive nuclide measurements from the 3758 samples. [taken from Ankjægård, et al., 2006].

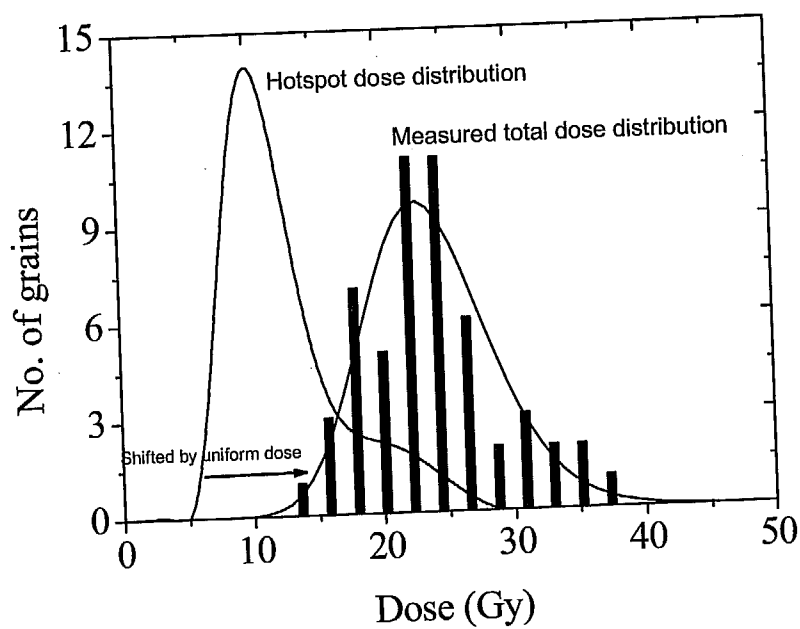


Figure 5.11 Murray and Roberts data with theoretically obtained dose distribution for the K concentration of the given sample.

basis for choosing bin-widths, we re-analyzed the frequency distribution using different bin-widths. As our model does not suggest explicitly the multimodal dose distribution, data were re-analyzed by marginally increasing the bin-width by 5 % i.e. 2.15 Gy compared to 2.05Gy. The recalculated dose distribution was fitted to a peak function and the RSD was calculated as 18.4 %. For comparing with theoretically predicted value of RSD for K concentration of 1.3%, the theoretical dose distribution was obtained (Fig. 5.11) for which RSD value is 30 %. This value is higher than experimental RSD because we did not include the uniform dose contributions from U and Th while computing the RSD from Murray and Robert's data. If we subtract the uniform dose contribution of 44 % of total dose, the resultant dose distribution derived from the Murray and Robert's data shows an RSD of about 34 %, which is marginally higher than model results of 30%. This is not surprising since experimental data would also include measurement errors.

For age estimation, the age based on the Eq. (5.12), i.e., minimum dose and the corresponding dose rate, yields an age 9.3 ± 1.4 ka (14.7 ± 2.2 Gy minimum palaeodose, dose rate of 1.58 Gy/ka, the 'p' factor of 0.43 for 1.3 % of K). The mean palaeodose and average dose rate yield an age of 9.8 ± 0.3 ka (22.7 ± 0.8 Gy, the mean value of the population and average dose rate of 2.32 Gy/ka). The consistency of ages 9.3 ± 1.4 ka (14.7 Gy) and 9.8 ± 0.3 ka (22.7 Gy) suggests that the sample was fully bleached and the distribution observed in data can be explained on the basis of beta heterogeneity. In such a case, the minimum dose and mean dose methods are expected to agree, as they indeed do. It may be added that the results based on this method and other methods such as TL/OSL and radiocarbon, are consistent within error limits.

Using the above procedures that successfully explain Murray and Roberts, 1997 results, ages for a large number of samples from Wahiba, Thar, Maxico were calculated. These are given in Table 5.2.

The tabulated values are plotted in Fig 5.12. Here the reported age is the single aliquot mean age. According to model, in case the sample was well bleached then the mean and model age should be same, provided appropriate dose rates are used for either cases; mean dose rate for the mean dose, and differential dose rate for the minimum dose. In the line of discussion, all the 22 samples with the exception of eight (9L3, 11L3, 17L6, 18L6, 19L7, GD03-03, GD03-13 and GD03-21) samples, accorded

Table 5.2. Detailed tabulation of results after applying modified age equation for Wahiba, Mexico and Thar desert samples.

| Code | Mean Dose ± (Gy) | | Min Dose ± (Gy) | | U ± (ppm) | | Th ± (ppm) | K ± (%) | F | 'p' factor | Mean Dose rate ± (Gy/ka) | | Dose rate ± (Gy/ka) | Mean Age ± (ka) | Differential | | | | | | |
|---------|------------------------|------|-----------------------|------|-----------------|------|------------------|---------------|------|---------------|-----------------------------------|------|---------------------------|-----------------------|--------------|------|------|------|------|------|-----|
| | 25.4 | 6.9 | 16.7 | 3.3 | 1.11 | 0.13 | | | | | 0.94 | 0.47 | | | 0.41 | 0.04 | 0.68 | 0.27 | 0.9 | 0.1 | 0.7 |
| 1L1 | | | | | | | | | | | | | | | | | | | | | |
| 2L1 | 40.6 | 4.8 | 27.3 | 4.8 | 1.12 | 0.12 | 1.02 | 0.44 | 0.91 | 0.09 | 0.54 | 0.40 | 1.4 | 0.1 | 1.0 | 0.1 | 29.2 | 4.5 | 27.2 | 5.5 | |
| 3L2 | 50.1 | 6.5 | 33.2 | 6.5 | 1.17 | 0.08 | 1.73 | 0.3 | 0.42 | 0.04 | 0.70 | 0.28 | 1.0 | 0.1 | 0.8 | 0.1 | 50.7 | 8.3 | 42.8 | 9.4 | |
| 4L2 | 38.2 | 4.3 | 26.9 | 4.3 | 1.04 | 0.1 | 0.98 | 0.38 | 0.88 | 0.09 | 0.54 | 0.39 | 1.3 | 0.1 | 1.0 | 0.1 | 28.5 | 4.3 | 27.9 | 5.3 | |
| 5L2 | 19.3 | 2.3 | 11.3 | 2.3 | 1.01 | 0.08 | 0.96 | 0.29 | 0.99 | 0.10 | 0.51 | 0.41 | 1.4 | 0.1 | 1.0 | 0.1 | 13.5 | 2.1 | 11.1 | 2.5 | |
| 6L3 | 57.5 | 12.5 | 37.6 | 12.5 | 1.12 | 0.11 | 0.8 | 0.6 | 1.41 | 0.14 | 0.46 | 0.44 | 1.8 | 0.2 | 1.3 | 0.1 | 31.1 | 7.5 | 29.1 | 10.1 | |
| 7L3 | 27.3 | 4.3 | 15.3 | 4.3 | 1.07 | 0.24 | 0.95 | 0.86 | 1.35 | 0.14 | 0.47 | 0.44 | 1.8 | 0.2 | 1.3 | 0.1 | 15.3 | 2.8 | 12.2 | 3.6 | |
| 8L3 | 22.8 | 4.9 | 19.6 | 4.2 | 0.85 | 0.01 | 1.8 | 0.54 | 0.35 | 0.04 | 0.71 | 0.25 | 0.8 | 0.1 | 0.7 | 0.1 | 26.8 | 6.4 | 29.5 | 7.0 | |
| 9L3 | 18.5 | 3.3 | 7.4 | 3.3 | 1.27 | 0.1 | 0.63 | 0.37 | 0.25 | 0.03 | 0.77 | 0.19 | 0.8 | 0.1 | 0.6 | 0.1 | 23.9 | 4.9 | 11.7 | 5.4 | |
| 11L3 | 24.9 | 4.1 | 14.6 | 4.1 | 1.21 | 0.07 | 0.95 | 0.27 | 0.55 | 0.06 | 0.64 | 0.32 | 1.1 | 0.1 | 0.8 | 0.1 | 23.4 | 4.5 | 18.2 | 5.4 | |
| 17L6 | 91.2 | 13.6 | 49.6 | 13.6 | 1.21 | 0.11 | 2.58 | 0.41 | 0.86 | 0.09 | 0.59 | 0.39 | 1.5 | 0.1 | 1.1 | 0.1 | 61.8 | 11.1 | 44.8 | 13.1 | |
| 18L6 | 92.7 | 14.3 | 25.8 | 14.3 | 0.86 | 0.08 | 1.55 | 0.28 | 1.02 | 0.10 | 0.51 | 0.41 | 1.5 | 0.1 | 1.0 | 0.1 | 63.1 | 11.6 | 24.7 | 13.9 | |
| 19L7 | 14.1 | 0.7 | 2.9 | 0.7 | 0.66 | 0.08 | 0.78 | 0.31 | 0.61 | 0.06 | 0.56 | 0.34 | 1.0 | 0.1 | 0.7 | 0.1 | 14.5 | 1.6 | 4.2 | 1.1 | |
| GD03-01 | 2.1 | 1.2 | 0 | 0.01 | 1.19 | 0.1 | 4.22 | 0.1 | 2.22 | 0.22 | 0.46 | 0.46 | 2.9 | 0.3 | 2.0 | 0.2 | 0.7 | 0.4 | 0.0 | 0.0 | |
| GD03-03 | 10.5 | 2.8 | 0.3 | 0.03 | 1.1 | 0.1 | 3.68 | 0.1 | 1.71 | 0.17 | 0.48 | 0.45 | 2.3 | 0.2 | 1.7 | 0.2 | 4.5 | 1.3 | 0.2 | 0.0 | |
| GD03-13 | 196.5 | 57.6 | 105.4 | 57.6 | 0.93 | 0.1 | 3.12 | 0.1 | 1.6 | 0.16 | 0.48 | 0.45 | 2.1 | 0.2 | 1.5 | 0.2 | 91.5 | 28.3 | 69.1 | 38.4 | |
| GD03-21 | 24.1 | 6.2 | 7.9 | 6.2 | 0.9 | 0.1 | 2.86 | 0.1 | 1.59 | 0.16 | 0.47 | 0.45 | 2.1 | 0.2 | 1.5 | 0.1 | 11.4 | 3.1 | 5.3 | 4.2 | |
| GPR-4 | 24 | 2.9 | 15.6 | 2.9 | 1.85 | 0.28 | 6.19 | 0.97 | 0.68 | 0.07 | 0.72 | 0.36 | 1.7 | 0.2 | 1.4 | 0.1 | 13.9 | 2.2 | 11.0 | 2.3 | |
| GPR-5 | 21.8 | 2.8 | 15.2 | 2.8 | 1.4 | 0.24 | 2.79 | 0.84 | 0.69 | 0.07 | 0.65 | 0.36 | 1.4 | 0.1 | 1.1 | 0.1 | 15.8 | 2.6 | 14.3 | 3.0 | |
| GPR-6 | 26 | 3.1 | 18.6 | 3.1 | 0.79 | 0.13 | 3.96 | 0.48 | 0.73 | 0.07 | 0.62 | 0.37 | 1.4 | 0.1 | 1.0 | 0.1 | 19.3 | 3.0 | 18.1 | 3.5 | |
| GPR-8 | 23.4 | 3.1 | 16.8 | 3.1 | 1.04 | 0.17 | 4.6 | 0.61 | 0.88 | 0.09 | 0.61 | 0.39 | 1.6 | 0.2 | 1.2 | 0.1 | 14.6 | 2.4 | 13.7 | 2.9 | |
| GPR-9 | 38.4 | 7.9 | 17.9 | 1.3 | 1.06 | 0.41 | 6.06 | 1.42 | 0.58 | 0.06 | 0.71 | 0.33 | 1.4 | 0.1 | 1.2 | 0.1 | 26.9 | 6.2 | 15.5 | 1.9 | |

* Cosmic ray dose rate is 0.18 Gy/ka

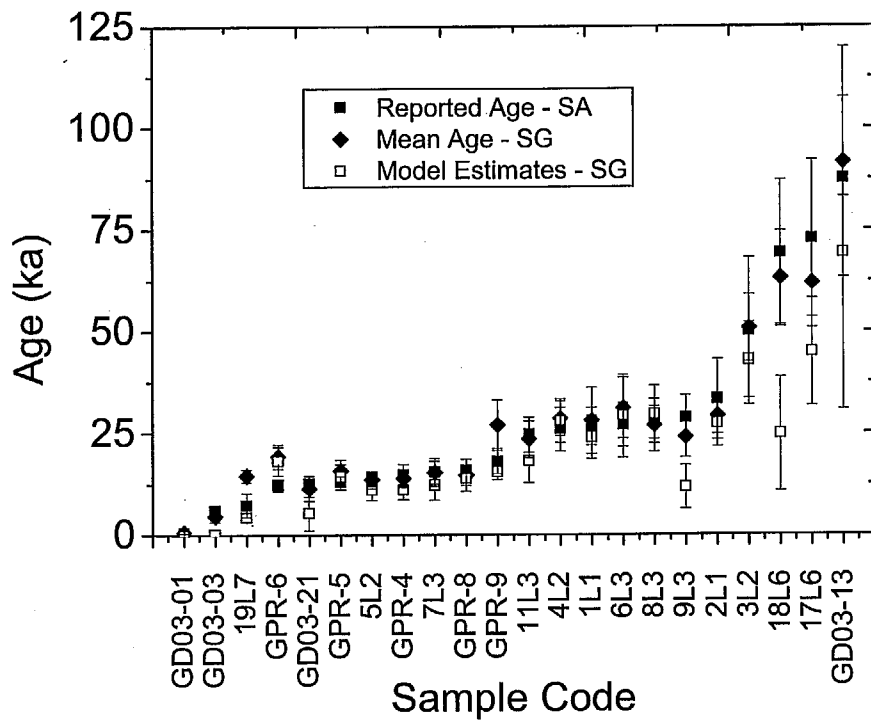


Figure 5.12. Comparison of model obtained age with the reported age and the mean age.

(within their error limits) with the model based calculations. Out of 22 samples of aeolian origin, 8 samples gave results different from the single aliquot and SG mean ages. Here the model ages were calculated using the Eq. (5.12). The reported age and mean ages should be same if the sample is well bleached. The model age estimates are lower than reported and mean single grain ages. Based on the model results, we suggest that these 8 samples are partially bleached even though they are inferred to be aeolian in origin and are not identified by any of the standard procedures to check their bleaching status at the time of deposition. The ages of these 8 samples were estimated from reasonable number of grains (9L3-29, 11L3-25, 17L6-67, 18L6-45, 19L7-20, GD03-03-80, GD03-13-41 and GD03-21-32) and hence these values are statistically rigorous. These need to be explained and perhaps grain size distribution will hold the clue. The success of this model in 14 cases out of 22 suggests that conceptually the approach is robust and only some fine tuning is needed. We thus feel that the present work implies a **paradigm shift** from a concept of "age analysis based on bleaching only" to age based on "bleaching and dose-rate heterogeneity".

5.4 Conclusion

In this chapter the effect of beta dose rate heterogeneity in partially bleached samples is explored and beta dose rate heterogeneity alone can cause ~ 40 % of RSD in the dose distribution. Higher K concentration would result in lower dispersion in equivalent dose. The true burial dose should be obtained by using a modified model age equation using the minimum dose and the minimum dose rate arising from beta heterogeneity, for all samples, well bleached or heterogeneous bleached.

Conventional procedures suggest that the use of the minimum dose and the average dose rate. In case of partially bleached sediments we show that this procedure can lead to an erroneous age estimate. In such a case a minimum dose rate should be used whose magnitude depends upon the K concentration in the sample.

In conclusion the differential dose rate approach presented above provides a more general and rigorous approach, can be used irrespective of bleaching status of sample. This approach will give a better approximation to true burial age even for poorly bleached samples

Chapter 6

Conclusion and Future outlook

This thesis reports on the measurement of dose distributions from single grains of quartz using the optically stimulated luminescence technique. The causes of the spread in the dose distribution are discussed and an analytical model is developed so as to treat the beta heterogeneity in the sediment matrix. This model is based on fluctuations (number and positional) in the K hotspots in a quartz dominated matrix. The results of the model are used to develop a dose selection protocol from a single-grain dose distribution from samples having different orders of partial bleaching.

The basis of the formulation arose from the measured paleodose distributions using multigrain and single grain OSL from three sets of aeolian samples from diverse provenances. It was observed that an unexpected large spread ($\sim 18\%$ for the multigrain and $\sim 35\%$ for the single grain measurements) in the dose distribution existed even after taking into account counting statistics and instrumental uncertainty. The possible sources for this large spread in the dose distribution were examined and based on a detailed analysis it was concluded that such large spread in the dose distribution arose from beta dose heterogeneity in the sediment matrix.

A mathematical approach was then developed to quantify the effect of spatial distribution of beta dose. An analytical solution was developed to quantify the spread in beta dose in the sediment. This solution is developed from the first principles using Laplace Transform technique by considering that the quartz grains and the beta emitting grains (K-feldspars) viz. hotspots are randomly distributed in the matrix. The capability of the algorithm for the numerical Laplace Inversion was tested with known standard peak shaped function ($y = xe^{-2x}$). The analytical model shows that about 20 to 45 % relative standard deviation (RSD %) in the single dose distribution can be caused solely by beta heterogeneity alone. The implications for choosing an appropriate dose rate for the different parts of the dose distributions are discussed. The implications of the model results on luminescence dating of single quartz grains were then examined. Since the most significant application of single grain dosimetry is for partially bleached sediments, the thesis demonstrates how a convolution of dose distributions arising due to combined effects of partial bleaching and heterogeneity of beta dose can be treated mathematically. It is shown that the minimum dose in the paleodose distribution is independent of both the partial bleaching and beta dose heterogeneity. A modified age equation is developed for the dose equivalent derived from the minimum dose estimate in the single grain dose distribution. This modified age equation includes only a fractional dose-rate from the potassium hotspots. This is to be contrasted with the conventional methods in which the mean dose rate from K is used irrespective of the manner in which the equivalent dose is calculated. The conventional method does not account for the distribution in doses arising from K hotspots and is therefore likely to overestimate the dose rate and hence give an erroneously younger age. An age calculation recipe was developed on the basis of the above results. This model is validated using a case study and results on samples from diverse geological settings. It is concluded that the analytical model developed in this thesis successfully explains the large spread in single grain dose distributions.

Future scope of this work

Several assumptions were made in order to derive an analytical solution to the beta heterogeneity problem. These assumptions need to be redefined in the future work. For example,

1. Minerals other than quartz and feldspar, and more realistic grain size distributions can be included in the sample matrix.
2. The model has considered uniform spherical grains of identical size. In nature a multimodal distribution is seen, which implies a closer packing. This would imply reduced beta range and hence higher heterogeneity of dose distribution. This needs to be properly evaluated.
3. The straggling effects of beta particles have not been considered in the present model. Consideration of such straggling effects would require a Monte-Carlo approach which can be incorporated in the future work,
4. The present model assumes that the hotspots have a uniform distribution in the matrix, and that there occurs no overlap between the spheres of influence of any two hotspots. The implication of this assumption is that the model approaches a uniform dose for sediments with greater than $\sim 2\%$ K concentration. Although majority of samples satisfy this criterion, it is not uncommon to find occasional samples with higher K content.
5. The minimum dose estimate is somewhat ambiguous (within 5%) because of the oscillations in the low dose part of the distribution. These oscillations arise because of the algorithm for numerical inversion of Laplace Transform used in this work. The accuracy and precision of the modified age equation can be improved by developing a more accurate inversion algorithm.
6. The model developed for K hotspots can be extended to include U and Th hotspots in the future work.

References

- Agersnap Larsen, N., Bulur, E., Bøtter-Jensen, L., McKeever, S. W. S., 2000. Use of the LM-OSL technique for the detection of partial bleaching in quartz. *Radiation Measurements*, 32, 2000, 419-425.
- Aitken, M. J., 1985. *Thermoluminescence Dating*, Academic Press, London.
- Aitken, M. J., 1998. *An introduction to Optical dating*, Oxford Science Publications.
- Ankjægaard, C. and Murray, A. S., 2006. Total beta and gamma dose rates based on beta counting on trapped charge dating. *Radiation Measurements*, *Submitted*.
- Bailey, R. M., Smith, B. W. and Rhodes, E. J., 1997. Partial bleaching and the decay form characteristics of quartz OSL. *Radiation Measurements* 27 (2), 123-136.
- Bailey, R. M., 2001. Towards a general kinetic model for optically and thermally stimulated luminescence quartz. *Radiation Measurements*, 33, 17-45.
- Bailey, R. M., 2003a. Paper I: The use of measurement-time dependent single-aliquot equivalent-dose estimates from quartz in the identification of incomplete signal resetting. *Radiation Measurements*, 37, 673-683.
- Bailey, R. M., 2003b. Paper II: The interpretation of measurement-time-dependent single-aliquot equivalent-dose estimates using predictions from a simple empirical model. *Radiation Measurements*, 37, 685-691.
- Bailey, R. M., Arnold, L. J., 2006. Statistical modeling of single grain quartz D_e distributions and an assessment of procedures for estimating burial dose. *Quaternary Science Reviews*, 25 (19-20), 2475-2502.
- Bateman, M. D., Frederick, C.D., Jaiswal, M.K., Singhvi, A.K., 2003. Investigations into the potential effects of pedoturbation on luminescence dating. *Quaternary Science Reviews*. 22, 1169-1176.
- Bellman, R.E., Kalaba, R.E., Lockett, J.A., 1966. *Numerical Inversion of the Laplace Transform: Applications to Biology, Economics, Engineering and Physics* (New York: Elsevier).

- Berger, G. W. & Luternauer, J. J., 1987. Preliminary field work for thermoluminescence dating studies at the Fraser River delta, British Columbia. Geological Survey of Canada Paper, 87/1A, 901-904.
- Berger, G. W., 1990. Effectiveness of natural zeroing of the thermoluminescence in sediments. *Journal of Geophysical Research* 95 (B8), 12375-12397.
- Beveridge, C., Kocurek, G., Ewing, G. R., Lancaster, N., Morthekai, P., Singhvi, A. K., Mahan, S. A., 2006. Development of spatially diverse and complex dune-field patterns: Gran Desierto Dune Field, Sonora, Mexico. *Sedimentology* 53 (6), 1391-1409.
- Bulur, E., 1996. An alternative technique for optically stimulated luminescence (OSL) experiment. *Radiation Measurements* 26, 701-709.
- Burbidge, C. I., Duller, G. A. T. and Roberts, H. M., 2006. D_e determination for young samples using the standardized OSL response of coarse grain quartz. *Radiation Measurements*, 4 (3), 278-288.
- Bush, D. A. and Feathers, J. K., 2003. Application of OSL single-aliquot and single-grain dating to quartz from anthropogenic soil profiles in the SE United States, *Quaternary Science Reviews*, 22 (19), 1153-1159.
- Bøtter-Jensen, L., 1997. Luminescence techniques: instrumentation and methods. *Radiation Measurements*, 27, 749-768.
- Bøtter-Jensen, L., Bulur, E., Duller, G. A. T., Murray, A. S., 2000. Advances in luminescence instrument systems. *Radiation Measurements* 32, 523-528.
- Bøtter-Jensen, L., Andersen, C. E., Duller, G. A. T., Murray, A. S., 2003a. Developments in radiation, stimulation and observation facilities in luminescence measurements. *Radiation Measurements* 37, 535-541.
- Bøtter-Jensen, McKeever and Wintle, 2003b. *Optically stimulated luminescence dosimetry*, Elsevier.
- Chandel, H. N., Patel, A. D., Vaghela, H. R. and Ubale, G. P. (2006) An effective reusable sampling pipe for luminescence dating. *Ancient TL* 24, 21-22.
- Chen & McKeever, 1997. *Thermoluminescence and its related phenomena*, World Scientific, Singapore.

- Clarke, M. L., 1996. IRSL dating of sands: bleaching characteristics at deposition inferred from the use of single aliquots. *Radiation Measurements*, 26, 611-620.
- Colls, A.E.L., 1999. Optical dating of fluvial sediment from the Loire Valley, France. MSc Thesis, University of Oxford, Oxford.
- Colls, A. E. L., Stokes, S., Blum, M. D. & Straffin, E., 2001. Age limits on the Late Quaternary evolution of the upper Loire River. *Quaternary Science Reviews*, 20, 743-750.
- Ditlefsen, C., 1992. Bleaching of K-feldspars in turbid water suspensions: a comparison of photo- and thermoluminescence signals. *Quaternary Science Reviews* 11, 33-38.
- Duller, G. A. T. and Bøtter-Jensen, L., 1993. Luminescence from potassium feldspars stimulated by infrared and green light. *Radiation Protection Dosimetry*, 47 (1/4), 683-688.
- Duller, G. A. T., 1996. Recent developments in luminescence dating of Quaternary sediments. *Progress in Physical Geography*, 20, 133-151.
- Felix, C. and Singhvi, A. K., 1997. Study of non-linear luminescence dose growth curves for estimation of paleodose in luminescence dating: results of Monte Carlo simulation. *Radiation Measurements* 27, 599-607.
- Fuchs, M. & Lang, A., 2001. OSL dating of coarse-grain fluvial quartz using single-aliquot protocols on sediments from NE Peloponnese, Greece. *Quaternary Science Reviews*, 20, 783-787.
- Galbraith, R. F. and Green, P. F., 1989. Estimating the component ages in a finite mixture. *Nuclear Tracks and Radiation Measurements* 17, 197-206.
- Galbraith, R.F., Roberts, R.G., Laslett, G.M., Yoshida, H., Olley, J.M., 1999. Optical dating of single and multiple grains of quartz from Jinmium rock shelter, northern Australia: Part I, experimental design and statistical models. *Archaeometry*. 41 (2), 339-364.
- Galbraith, R. F., 2002. A note on the variance of a background corrected OSL count. *Ancient TL* 20, 49-51.

- Gemmell, A. M. D., 1997. Fluctuations in the thermoluminescence signal of suspended sediment in an alpine glacial meltwater stream. *Quaternary Science Reviews* 16, 281-290.
- Glennie, K. W. and Singhvi, A. K., 2002. Event stratigraphy, paleoenvironment and chronology of SE Arabian deserts. *Quaternary Science Reviews*, 21 (7), 853-869.
- Glennie, K. W., Morthekai, P., Fryberger, S. G., Hern, C. Y., Singhvi, A. K., 2007. Dating the Sharqiyah (Wahiba) aeolian sands, Oman. *In preparation*.
- Gorton, N. T., Walker, G, Burley, S. D., 1996. Experimental analysis of the composite blue CL emission in quartz – is this related to aluminium content? In *International Conference on Cathodoluminescence and Related Techniques in Geosciences and Geomaterials*, Nancy, France, Abstracts, 59-60.
- Götze, J., Plötze, M. and Habermann, D., 2001. Origin, spectral characteristics and practical applications of the cathodoluminescence (CL) of quartz – a review. *Mineralogy and Petrology*, 71, 225-250.
- Herman Cember, 1996. *Introduction to Health Physics*, 3rd Edition, McGraw-Hill.
- Hildebrand, F. B., 1987. *Introduction to Numerical inversion*, 2nd Edition, Dover Publications, USA.
- Huntley, D. J., Godfrey-Smith, D. I., Haskell, E. H., 1991. Light-induced emission spectra from some quartz and feldspars. *Nuclear Tracks and Radiation Measurements*, 18, 127-131.
- Hütt, G., Jaek, I., Tchonka, J., 1988. Optical dating: K-feldspars optical response stimulation spectra. *Quaternary Science Reviews*, 7, 381-386.
- Istratov, A. A. and Vyvenko, O. F., 1999. Exponential analysis in physical phenomena, *Review of Scientific Instruments*, 70 (2), 1233-1257.
- Jacobs, Z., Duller, G. A. T. and Wintle, A. G., 2006. Interpretation of single grain De distributions and calculation of De. *Radiation Measurements*, 41, 264-277.
- Jain, M., Bøtter-Jensen, L. and Singhvi, A. K., 2003a. Dose evaluation using multiple-aliquot quartz OSL: test of methods and a new protocol for improved accuracy and precision. *Radiation Measurements*, 37, 67-80.

- Jain, M., Murray, A. S., Bøtter-Jensen, L., 2003b. Characterisation of blue-light stimulated luminescence components in different quartz samples: implications for dose measurement. *Radiation Measurements* 37, 441-449.
- Jain, M., Murray, A. S. and Bøtter-Jensen, L., 2004a. Optically stimulated luminescence dating: how significant is incomplete light exposure in fluvial environments?, *Quaternaire*, 15 (1-2), 143-157.
- Jain, M., Thomsen, K.J., Botter-Jensen, L., Murray, A.S., 2004b. Thermal transfer and apparent dose distributions in poorly bleached mortar samples: results from single grains and small aliquots of quartz. *Radiation Measurements* 38 (1), 101-109.
- Jain, M., 2007. Insufficient bleaching in the single quartz grains from various geological settings, *In preparation*.
- Jaiswal, M., 2005. Optically stimulated luminescence dating of fluvial sediments: applications and implications to paleoseismology and paleoclimatology, M. S. University of Baroda, Vadodara, India.
- Jaiswal, M. K., Jain, V., Nagar, Y. C., Morthekai, P., Singhvi, A. K. Limits of applicability of standard growth curve in single aliquot regeneration procedure in luminescence dating. *Radiation Measurements, In preparation*.
- Kelly, W. H., Bear, G.B., Peters, R.A., 1959. The beta decay of K40. *Nuclear Physics*, 11, 492-498.
- Kittel, C., 2002. *Introduction to Solid State Physics*, 7th Edition, John Wiley & Sons Ltd., Singapore.
- Krbetschek, M. R. Götze, J. D. S. and Trautmann, T., 1997. Spectral information from minerals relevant for luminescence dating. *Radiation Measurements*, 27, 695-748.
- Lepper, K., Agersnap Larsen, N., McKeever, S.W.S., 2000. Equivalent dose distribution analysis of Holocene eolian and fluvial quartz sands from Central Oklahoma. *Radiation Measurements* 32, 603-608.
- Li, S.-H., Wintle, A. G., 1992. Luminescence sensitivity changes due to bleaching of sediments. *Nuclear Tracks and Radiation Measurements*, 20, 567-573.

- Murari M.K. and Singhvi A.K., 2006. Component Specific palaeodose estimation in optically stimulated luminescence dating : Methodology, Applications and Implications, APLD, Honkong.
- Murray, A. S., Olley, J. M. & Caitcheon, G. G., 1995. Measurement of equivalent doses in quartz from contemporary water-lain sediments using optically stimulated luminescence. *Quaternary Science Reviews*, 14, 365-371.
- Murray, A.S., Roberts, R.G. 1997. Determining the burial time of single grains of quartz using optically stimulated luminescence. *Earth and Planetary Science Letters* 152, 163-180.
- Murray, A. S., Wintle, A. G., 2000. Luminescence dating of quartz using an improved single-aliquot regenerative-dose protocol. *Radiation Measurements* 32, 57-73.
- Murray, A. S., Olley, J. M., 2002. Precision and accuracy in the optically stimulated luminescence dating of sedimentary quartz: a status review. *Geochronometria* 21, 1-16.
- Narayanan, K.S.S., Ramadurai, K.S., 1992. The numerical solution of inverse problems using Gaussian quadrature. *European Journal of Physics* 13, 111-116.
- Nathan, R. P., Thomas, P.J., Jain, M., Murray, A.S., Rhodes, E.J., 2003. Environmental dose rate heterogeneity of beta radiation and its implications for luminescence dating: Monte Carlo modeling and experimental validation. *Radiation Measurements* 37, 305-313.
- Nuttal, R. H. D. and Weil, J. A., 1980. Two hydrogenic trapped-hole species in α -quartz. *Solid State Communications*, 33, 99-102.
- Olley, J. M., Roberts, R. G., Murray, A. S., 1997. Disequilibria in the Uranium decay series in sedimentary deposits at Allen's cave, Nullarbor Plain, Australia: implications for dose rate determinations. *Radiation Measurements* 27, 433-443.
- Olley, J. M., Caitcheon, G.G., Murray, A.S., 1998. The distribution of apparent dose as determined by optically stimulated luminescence in small aliquots of fluvial quartz: Implications for dating young sediments. *Quaternary Geochronology* 17, 1033-1040.

- Olley, J. M., Caitcheon, G.G., Roberts, R.G., 1999. The origin of dose distributions in fluvial sediments, and the prospect of dating single grains from fluvial deposits using optically stimulated luminescence. *Radiation Measurements* 30, 207-217.
- Olley, J. M., Tim Pietsch, Roberts, R.G., 2004. Optical dating of Holocene sediments from a variety of geomorphic settings using single grains of quartz. *Geomorphology* 60 (3-4), 337-358.
- Olley, J. M., Roberts, R. G., Yoshida, H., Bowler, J. M., 2006. Single-grain optical dating of grave-infill associated with human burials at Lake Mungo, Australia. *Quaternary Science Reviews*, 25, 2469-2474.
- Piessens, R., 1969. Numerical inversion of the Laplace Transform, *IEEE Transactions of Automatic Control*, AC-14, 299-301.
- Prescott, J. R., and Stephan, L. G., 1982. Contribution of cosmic radiation to environmental dose, *PACT* 6, 17-25.
- Randall, J. T. and Wilkins, M. H. F., 1945. Phosphorescence and electron traps. *Proceedings of the Royal Society of London A* 184, 366-407.
- Rendell, H. M., Webster, S. E. & Sheffer, N. L., 1994. Underwater bleaching of signals from sediment grains: new experimental data. *Quaternary Science Reviews* 13, 433-455.
- Rhodes, E. J. & Pownall, L., 1994. Zeroing of the OSL signal in quartz from young glaciofluvial sediments. *Radiation Measurements* 23, 581-585.
- Rink, W. J., Rendell, H., Marseglis, E. A., Luff, B. J., Townsend, P. D., 1993. Thermoluminescence spectra of igneous quartz and hydrothermal vein quartz. *Physical and Chemistry of Minerals*, 20, 353-361.
- Roberts, H. M. and Duller, G. A. T., 2004. Standardised growth curves for optical dating of sediments using multiple-grain aliquots. *Radiation Measurements*, 38 (2), 241-252.
- Roberts, R.G., Spooner, N.A., Jones, R., Cane, S., Olley, J.M., Murray, A.S., Head, M.J., 1996. Preliminary luminescence dates for archaeological sediments on the Nullarbor Plain, South Australia. *Australian Archaeology* 42, 7-16.
- Schwartz, G., 1978. Estimating the dimension of a model. *The annals of Statistics* 5 (2), 461-458.

- Shlukov, A. I., Usova, M. G., Voskovskaya, L. T., Shakovats, S. A., 2001. New dating techniques for quaternary sediments and their application on the Russian Plain. *Quaternary Science Reviews*, 20 (5-9), 875-878.
- Singarayer, J. S., Bailey, R. M., 2003. further investigations of the quartz optically stimulated luminescence components using linear modulation. *Radiation Measurements* 32, 451-458.
- Singhvi, A. K., Sharma, Y. P., Agrawal, D. P., 1982. Thermoluminescence dating of sand dunes in Rajasthan, India. *Nature* 295, 313-315.
- Singhvi, A. K. & Wagner, G. A., 1986. Thermoluminescence and its applications to young sedimentary deposits. In *Dating young sediments*, eds. A. J. Hurford, E. Jäger and J. A. M. Ten Cate, CCOP Technical Publication 16, pp. 159-197. CCOP Technical Secretariat, Bangkok.
- Singhvi, A. K., & Lang, A., 1998. Improvements in infra-red simulation dating of partially bleached sediments: the differential partial bleach technique. *Ancient TL*, 16, 1-8.
- Singhvi, A. K. & Wintle, A. G., 1999. Luminescence dating of Aeolian and coastal sand and silt deposits: applications and implications. In A. S. Goudie, I. Livingstone, S. Stokes (Eds.) *Aeolian environments, Sediments and Landforms*. Wiley Chichester, 293-317.
- Smith, B. W. and Rhodes, E. J., 1994. Charge movements in quartz and their relevance to optical dating. *Radiation Measurements* 23, 329-333.
- Spooner, N. A., 1994. On the optical dating signal from quartz. *Radiation Measurements*, 23, 593-600.5656
- Stokes, S., Bray, H. E. & Blum, M. D., 2001. Optical resetting in large drainage basins: tests of zeroing assumptions using single-aliquot procedures. *Quaternary Science Reviews* 20, 879-885.
- Thomsen, K. J., Jain, M., Bøtter-Jensen, L., Murray, A. S., Junger, H., 2003. Variation with depth of dose distributions in single grains of quartz extracted from an irradiated concrete block. *Radiation Measurements*, 37, 315-321.

- Thomsen, K. J., Murray, A.S., Bøtter-Jensen, L., 2005. Sources of variability in OSL dose measurements using single grains of quartz. *Radiation Measurements* 39 (1), 47-61.
- Thomsen, K. J., Murray, A. S., Bøtter-Jensen, L., Kinahan, J., 2006. Determination of burial dose in incompletely bleached fluvial samples using single grains of quartz. *Radiation Measurements*, submitted.
- Vander Touw, J. W., Galbraith, R. F., Laslett, G. M., 1997. A logistic truncated normal mixture model for overdispersed binomial data. *Journal of Statistical Computation and Simulation* 59, 349-373.
- Vandenbergh, D., Hossain, S.M., De Corte, F., Van den haute, P., 2003. Investigations on the origin of the equivalent dose distribution in a Dutch coversand. *Radiation Measurements* 37, 433-439.
- Vermeesch, P., 2004. How many grains are needed for a provenance study?, *Earth and Planetary Science Letters*, 224 (3-4), 441-451.
- Wallinga, J., Murray, A. S. and Duller, G. A. T., 2000. Underestimation of equivalent dose in single-aliquot optical dating of feldspars caused by preheating. *Radiation Measurements*, 32 (5-6), 691-695.
- Wang, R. and Li, X. A., 2001. Monte Carlo dose calculations of beta-emitting sources for intravascular brachytherapy: A comparison between EGS4, EGSnrc and MCNP. *Medical Physics*, 28 (2), 134-141.
- Yoshida, H., Roberts, R. G., Olley, J. M., 2003. Progress towards single-grain optical dating of fossil mud-wasp nests and associated rock art in northern Australia. *Quaternary Science Reviews*, 22, 1273-1278.
- Zhang, J. F., Zhou, L. P., Yue, S. Y., 2003. Dating fluvial sediments by optically stimulated luminescence: selection of equivalent doses for age calculation. *Quaternary Science Reviews*, 22, 1123-1129.
- Zimmerman, D. W., 1971. The radiation-induced increase of the 100°C thermoluminescence sensitivity of fired quartz. *Journal of Physics C* 4, 3265-3276.

List of publications

Papers in refereed Journals

1. P. Srivastava, G.A. Brook, E. Marais, **P. Morthekai**, A. K. Singhvi, 2006. Depositional environment and single aliquot and single grain OSL chronology of the Homeb silt deposits, Kuiseb River, Namibia. *Quaternary Science Reviews* 65,478-491.
2. Y.S. Mayya, **P. Morthekai**, Madhav, A. K. Singhvi, 2006. Towards quantifying beta microdosimetric effects in single-grain quartz dose distribution, *Radiation Measurements* 41, 1032-1039.
3. C. A. Beveridge, G. Kocurek, N. Lancaster, R. Ewing, **P. Morthekai**, S. Mahan, A. K. Singhvi, 2006. Development of spatially diverse and complex dune-field patterns: Gran Desierto dune field, Sonora, Mexico, *Sedimentology* 53 (6), 1391-1409.

Abstracts in Conferences

1. **P. Morthekai**, A. K. Singhvi., 2005. The absorbed dose distribution of natural quartz grains using single aliquot and single grain analysis, NCLA-2005, Bangalore, Luminescence Society of India.
2. **P. Morthekai**, Y. S. Mayya, A. K. Singhvi., 2005. Further studies on microdosimetry in single grain luminescence dating, LED-2005, University of Cologne, Germany.
3. Beveridge, C. A., Kocurek, G., Lancaster, N., Ewing, R., **Morthekai, P.**, Mahan, S., Singhvi, A. K., 2004. Origin and evolution of the Gran Desierto sand sea, 2004 Denver Annual Meeting.

Papers under preparation

1. **P. Morthekai**, Y. S. Mayya, A. K. Singhvi, Beta dose distribution among the single quartz grains due to the heterogeneous distribution of dose emitters.
2. **P. Morthekai**, Y. S. Mayya, A. K. Singhvi, M. Jain, A solution for true depositional age using partially bleached quartz single grains, Radiation Measurements.
3. **P. Morthekai**, Madhav K Murari, A. K. Singhvi. Effects of natural sensitivity change in the dose estimation – Understanding using the components of Quartz OSL, Radiation Measurements.
4. **P. Morthekai**, A. K. Singhvi. Comparison of ages from the multiple and single aliquot methods with single grains of quartz : Wahiba sands, Radiation Measurements.
5. Glennie, K., **P. Morthekai**, A. K. Singhvi. Dating the Sharqiyah (Wahiba) Aeolian sands, Oman.
6. B. S. Paliwal, **P. Morthekai**, A. K. Singhvi. Age of the Elephant fossils from Bhadawasi, District Nagaur, Rajasthan and their signatures on the past climate of the Thar Desert.

